Numerical Modeling of Flow in Parshall Flume Using Various Turbulence Models

Mehdi Heyrani

Thesis submitted to the University of Ottawa
in partial fulfillment of the requirements for the

Doctorate in Philosophy Civil Engineering

Department of Civil Engineering
Faculty of Engineering
University of Ottawa

Abstract

Studying the behavior of hydraulic structures under various extreme conditions is far beyond the reach of traditional build-test experimental methods. Following the typical method, it is necessary to provide the downscaled model to be used in the laboratory and determine various structural parameters against unforeseen scenarios, which should be mimicked in the laboratory. Usually, human and instrument errors as well as scale effects are some of the causes of inaccurate results; therefore, substitute methods have always been sought to determine the stability and efficiency of various hydraulic devices. The implementation of computer models, also referred to as numerical simulation, is one of the most efficient ways to reduce time and cost, and at the same time, add to the degree of confidence in the design process. Improvements in computational power of supercomputers in recent decades have led researchers and engineers to become familiar with these numerical models and implement them in various studies. One of the basic hydraulic structures that is widely used to measure the flow for open channels is the Parshall flume. Although the Parshall flume is simple to use, the application of various rating equations for different sizes highly affects the output value, which is the flowrate. To avoid this, appropriate rating equation must be developed for various sizes that are not listed in the standard Parshall flume size chart. With the help of the Computational Fluid Dynamic (CFD) techniques, numerous turbulence models i.e., standard $k-\varepsilon$, RNG $k-\varepsilon$, realizable $k-\varepsilon$, $k-\omega$, $k-\omega$ SST, $k-\omega$ SST DES, Smagorinsky and Dynamic *k* equation, have been used to simulate different geometric setups for different sizes of Parshall flumes. The result from various families of turbulence models, i.e., Reynold Average Navier-Stokes (RANS), Large Eddy Simulation (LES) and Detached Eddy Simulation (DES), used in this study, provide promising values with acceptable margins of error, which were found to be less than 3% in all cases except one. The application of numerical modeling to simulate the flow in Parshall flumes is used to verify the reliability of applying OpenFOAM as the open-source CFD used for all the simulations in this study. The data obtained from the numerical simulations are considered a reliable source to adjust the rating equation for any future non-standard Parshall flume. Overall, it should be pointed out that the quality of non-linear turbulence models, i.e., Shih-Q, LC and v^2-f, were considerably higher than those obtained using linear turbulence models.

Acknowledgments

I would like to express my sincere gratitude to my advisors Prof. Abdolmajid Mohammadian and Prof. Ioan Nistor for the continues support of my Ph.D. study, for their patience, motivation, and immense knowledge. Without their precious support it would not be possible to conduct this research.

Last but not least, I wish to thank my loving and supportive wife, Faranak, who provide unending inspiration. Without her tremendous understanding and encouragement in the past three years, it would be impossible for me to complete my study.

Table of Contents

List of Figures

List of Tables

List of acronyms

ADVM	Acoustic Doppler Velocity Meter
ANFIS	Adaptive Neuro-Fuzzy Inference System
ANN	Artificial Neural Network
ANSYS	Analysis System
ASTM	American Society for Testing and Materials
CFD	Computational Fluid Dynamic
CRMSE	Central Root Mean Square Error
CVRMSE	Coefficient of Variation of the Root Mean Squared Error
DES	Detached Eddie Simulation
DNS	Direct Numerical Simulation
DO	Dissolved Oxygen
FAVOR	Fractional Area/Volume Obstacle Representation
FL	Fuzzy Logic
FVM	Finite Volume Method
ISO	International Organization for Standardization
JIS	Japanese Industrial Standard
LC	Lien Cubic
LES	Large Eddy Simulation
LRR	Launder, Reece and Rodi
MCM	Monte Carlo Method
MCM	Monte Carlo Method
MF	Membership Function-Based
MPF	Modified Parshall Flumes
NS	Navier-Stokes
OpenFOAM	Open-Source Field Operation and Manipulation
PF	Parshall Flume
R	correlation coefficient
RANS	Reynolds Average Navier-Stokes
RMSE	Root Mean Square Error
RNG	Re-normalization Group
RSM	Reynolds Stress Model
RVF	Rapidly Varied Flow
SEE	Standard Error of Estimate
SGS	Subgrid-Scale
SQ	Shih Quadratic
SSG	Speziale, Sarkar and Gatski
SST	Menter's Shear Stress Transport turbulence model
VoF	Volume of Fluid

List of Symbols

Re ……..	Reynolds number
ρ ……..	Density (kg/m^3)
Q ……..	Discharge volume (m^3/s)
g ……	Gravitational acceleration (m/s^2)
K ……..	A constant, can be obtained experimentally
t …….	Time (s)
r……..	Radial distance (rad)
P ……	Fluid pressure (N/m^2)
v ……	kinematic viscosity (m^2/s)
k ……..	turbulent kinetic energy(m^2/s^2)
ε……..	turbulent dissipation rate (m^2/s^3)
W……	Width of the channel (m)
H……..	Water level in the channel (m)
v……..	Vertical component of velocity (m/s)
u……..	Horizontal component of velocity (m/s)
w…….	Velocity component in z direction (m/s)
α……..	Percentage of presence of water ($VoF\ method$)
∇ …….	Vector differential operator
H_a, H_b, H_c …….	Water Level in stilling wells of Parshall flume
δ_m ……..	Wall distance
μ_t ……	Modeling turbulent viscosity
ν …….	Turbulence viscosity
ω ……	Specific dissipation rate
σ_ε ……..	Model constant
S ……..	Modulus of mean rate of strain tensor
β, γ……..	Model constant
L……	Turbulence length scale
T……	Turbulence time scale

$C_1, C_2, C'_{\varepsilon 1}, C_{\varepsilon 2}$ ……	$v^2 - f$ coefficients
$S_k, S_\varepsilon, S_{\overline{V^2}}, S_f$ ……	Constant coefficient defines by user for $v^2 - f$
f ……	Solution to the last equation in $v^2 - f$
$\Omega^*, \Omega_{ij}, S^*_{ij}, S^*, U^*, \eta, W^*$ ……	Constants of Shih quadratic turbulence model
$C_\mu, C_1, C_2, C_3, A_3, A_5, \sigma_k, \sigma_\varepsilon$ ……	Constants of Shih quadratic turbulence model
Π_1, Π_2, Π_3 ……	Constants of Shih quadratic turbulence model
C_s ……	Smagorinsky Constant
G_b, G_k ……	Model constant

Chapter 1

Introduction

1.1 Introduction

Early civilizations formed along rivers, not only to provide the basic necessity of human needs, i.e., water, but also to harvest the great power lying within the river. One of the early sources of energy harnessed by mankind was the water flow power that was extracted by water wheels for the purpose of turning flour milling stones. The idea of transmuting the water's kinetic energy into mechanical motion in order to perform extensive daily tasks was developed over the time. Through the course of history, the understanding of humans regarding the importance of natural energy resources has evolved significantly.

As a key parameter to harvest the energy of the river flow efficiently, it is important to accurately determine the discharge rate of the flow in the river or open-channel. Numerous devices, electrically or mechanically powered, were introduced over time by various inventors. However, by focusing on the renewable nature of the device's main power source, it should be free from any external source of energy; hence, it must heavily rely on the harvested power of the flow.

1.1.1 Research Needs

The accuracy assessment of the Parshall flume, a basic flowrate measurement hydraulic structure which is used mostly in open channels, has been neglected due to lack of adequate high precision laboratory experiments. Various parameters, i.e., flow entrance condition, proper placement of stilling wells, channel slope and the shape of the entrance wing-walls, and others contribute to the overall performance of Parshall flumes. Considering the relative alteration of the parameters mentioned above is an expensive and time-consuming task if conducted in laboratory conditions and this may result in obtaining inconsistent results due to various experimental errors.

Applications of numerical modeling on various types of flumes have been carried out by different scholars using several Computational Fluid Dynamic (CFD) software i.e., SOLA-FLUMP, Ansys Fluent and FLOW-3D, to improve the results' accuracy [1–12]. Although Parshall flume had been in the focus of multiple numerical studies, lack of investigation on small throat size Parshall flume i.e., 7.62 cm, has been observed, as the majority sizes of the Parshall flumes that had been numerically analyzed, were the large throat size flumes. The application of such sizes is common in a typical width open channel and in industrial location i.e., Wastewater Treatment Plant, as flow

measuring device. Therefore, study on small throat size Parshall flume that has more application in controlled condition environment i.e., laboratory, has been deemed necessary.

Nowadays, it is possible for the majority of researchers and engineers to have access to supercomputers to simulate their proposed hydraulic design in order to improve the weak points in the future. In general, CFDs are available to use with or without a commercial license where OpenFOAM can be named as a powerful open-source and free CFD, while the most popular commercially licensed CFD, FLOW-3D, has been implemented by many scholars in various important fluid dynamics projects.

Although the importance of laboratory experiment presence cannot be understated when validating the numerical simulation findings, the focus of this study was to investigate the implementation of CFD model to enhance the design of Parshall flumes, and provide an overview of the effectiveness of various turbulence models that have been used. The reliability of using the simulation results compared to the experimental data was investigated in depth in two technical papers in chapters 3 and 4.

1.1.2 Background on flow measurement

Baron Kelvin once highlighted that what can’t be measured, can't be managed, and this is particularly true in flow measurement. The historical interest goes back thousands of years ago when the flow of water was measured by the Romans from their aqueducts to the consumers, which were the households in that time over 4 millennia ago. In China, in order to measure the salt produced from salt water in brine pots, the flow of salty water was measured in early times [13]. However, the purpose of the measurement was only to control the process. A weir with a basic form was one of the first water meters used by the Egyptians around three thousand years ago. The Egyptians were the first to invent a clock that was operated by the flow of water, called a clepsydra. The clock was formed in a bowl-shaped container filled with water. The water escaped through a tiny opening and the water level decrease indicated the time. It dates back to at least fourteen hundred B.C. Figure 1 shows the reconstructed Clepsydra from Egypt.

Figure 1: Reconstruction of an Egyptian Clepsydra from the Temple of Karnak[14]

Since the relation between the area, head and the velocity were obviously not appreciated, there was no significant progress at all before A.D. 1500. Over the last six centuries, a handful of scientists have made breakthroughs in the understanding of flow phenomena. The first principles of flow measurement started to be understood only around four hundred years ago when the need to charge consumers for water became essential. By the end of the 19th century, it had become more important to measure the flowrate for utility and industrial purposes. The pressure differential methods predominated up to about 1950 when other methods were introduced. The number of different measuring techniques have grown to around sixty nowadays [15]. Eight main techniques for flow measurement are currently available: ultrasonic, variable area, positive displacement, differential pressure, measuring technique used in turbines which is called inferential, fluid-dynamic, electromagnetic and mass flowmeters. The mass flow meters have been developed recently for industrial purposes where the fluidal products are valuable by weight, not by volume [16].

1.1.3 Venturi Tube

One of the early measuring devices was built in the 19th century by Clement Herschel (1842-1930). He wished to implement Bernoulli's principle into water flow. Unlike Venturi, who only used two cones joined together, Herschel decided to integrate a contoured throat and thus came up with the classical venturi tube. The pressure at two points along the device (upstream of the throat and at the throat itself) was measured and the pressure difference was translated with the Bernoulli equation into flowrate. An original form of differential pressure meter is the venturi tube. The

typical design is shown in the figure below. [17] Figure 2 shows the schematics of the classic Venturi Tube.

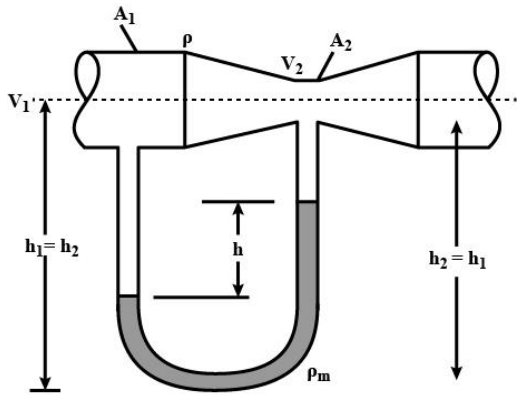

Figure 2: Venturi Tube

In general, any changes in the cross-sectional area of a fluid in motion will result in changes in its pressure and velocity. Since the losses of energy are minimal and the conditions of flow are close to ideal, the discharge coefficients of venturi meters are commonly very close to unity, where 0.98 is a typical value. The Coefficient of Discharge is still a function of the Reynolds number, particularly when the flow is laminar flow. The relation is shown in the figure below.

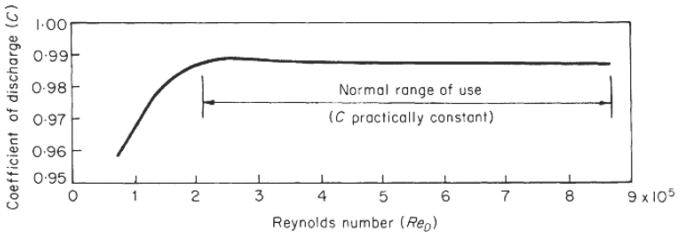

Figure 3: Reynolds number vs. coefficient of discharge [18]

1.1.4 Electromagnetic Flowmeters

The same principle of the electrical generator has been applied in the electromagnetic flowmeter. When, within a magnetic field, the movement of a conductor has been felt, a voltage is generated in the conductor. The speed of the movement is in direct proportion with the level of generated voltage. The flowrate of water is determined based on the movement of the fluid (as the conductor) through the pipe or channel so that both the fluid and the path are in a magnetic field. To detect

the generated voltage, the electrodes are attached to the walls of the passage, i.e., the open channel or pipe, as shown in the figure. The flowrate is proportional to the voltage.

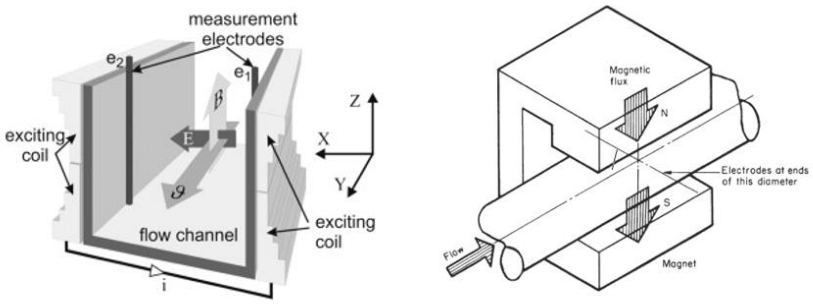

Figure 4: The concept of the electromagnetic flow measurement method in an open flow channel (left) and in a pipe (right). [Elsevier][19]

In reality, the uniformity of the magnetic field is far from attainable as there is no symmetricity in the flow. To solve this issue and achieve highly accurate results from the meter, as with other flowmeters, calibration is required.

1.1.5 Parshall flume

The most popular and reliable flow measuring device, that has been widely used all over the world, is a specifically designed flume, called the Parshall flume. It provides the discharge of the flow passing through a channel with a width as narrow as 1 in (2.54-cm), up to a wide river having a width of 144 in (365.8-cm) Parshall flumes have been used for almost a century, and many variations of the flume have been introduced by numerous researchers over time, i.e., Cutthroat flume, Montana flume, etc. The topic of climate change and its harmful side effects on our environment makes the use of sustainable energy powered devices more in demand as no external energy source is required for their operation. The Parshall flume is a measuring device with no moving parts; therefore, no significant amount of energy is required to run one.

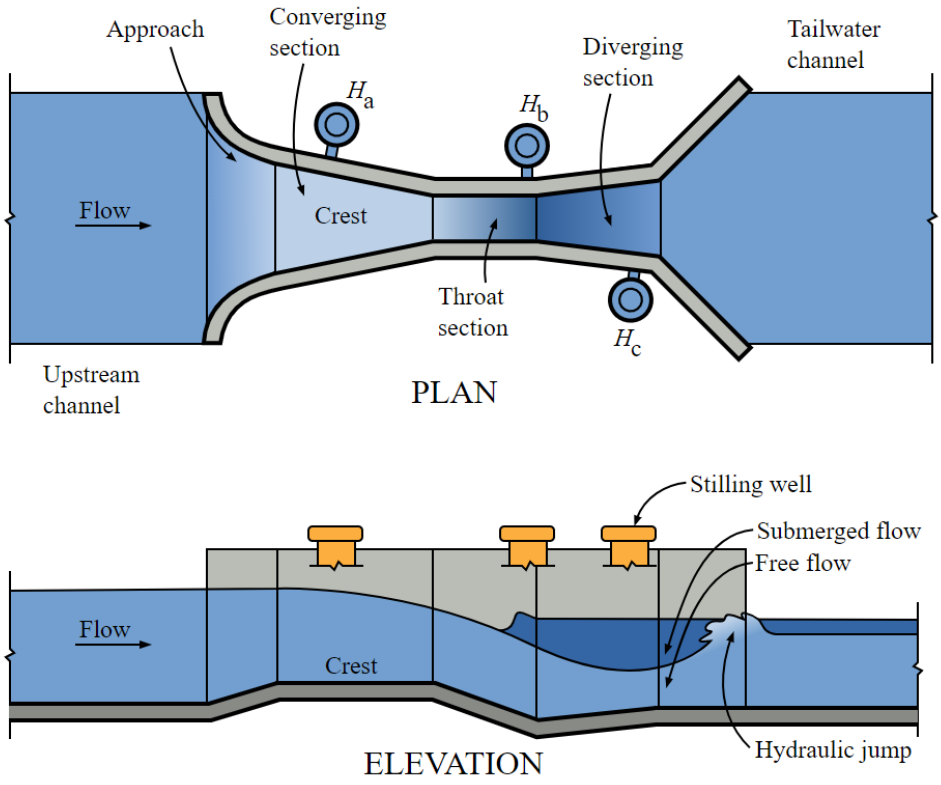

Figure 5: Parshall Flume top and side view [20]

The Froude number of the flow entering the Parshall flume should not exceed 0.5 (which corresponds to a sub-critical flow)[21]. Due to the introduction of the narrow parallel walls at throat section and the steep bed slop, the type of the flow changes from sub-critical to super critical. If the approaching water flow is determined to be of a super-critical flow type, then, due to the occurrence of a hydraulic jump, flow energy is dissipated before entering the Parshall flume. The point where the critical depth occurs is the location where the sub-critical flow converts into super-critical flow.

The main factor that contributes to its popularity is the simplicity of its operation, as it can be used by various types of people, from farmers to engineers, where a basic knowledge in math is adequate to perform the translation of the water head into discharge, i.e., employment of the rating equation. One of the challenges with the application of the Parshall flume over time is the implementation of altered or modified Parshall flumes. Either the design was not followed precisely or the installation guideline was significantly neglected. As a result, the accuracy of the flume can drop to as low as 30%. For example, on numerous locations it was observed by Heiner [22] that the

original guidelines and designs have been altered with or without proper modifications to its rating equation. It is very common that if the project specification requires a Parshall flume that is not listed in the standard size chart, a non-standard Parshall flume should be proposed along with an appropriate rating equation. It requires extensive laboratory experiments to provide the proper constant values to the rating equation.

Due to the significant cost of laboratory experiments the design of new Parshall flumes becomes prohibitive. Hence, the rating equations for non-standard Parshall flumes are usually obtained using a combination of rating equations for similar sized flumes.

The standard design and the characteristic of the discharge of Parshall flume have been addressed in the following standard codes;

- ASTM D1941 – 91 (2013) Standard Test Method for Open Channel Flow Measurement of Water with the Parshall Flume [23]
- ISO 9826 (1992) Measurement of Liquid Flow in Open Channels – Parshall and SANIIRI Flumes [24]
- JIS B7553 (2017) Parshall Flume Type Flowmeters [25]

Between years 1953 to 1991, the USBR [26] was the only source to set exact dimensions of Parshall flumes. The need of standardization for the Parshall flume by the world's technical standards organizations was recognized and in 1991 the first standard manual containing Parshall flume exact dimensions had been produced by ASTM. So far, there have been several revisions published by ASTM standard, notably in 1996, 2001, 2007, and 2013. The ISO published its standard for Parshall flume in 1992 and no updates have been published since. The Japanese Industrial Standard (JIS) has published its 93rd latest edition in 2017. The requirement set by ASTM D1941 for the dimensions of Parshall flume allows +/- 2% tolerance while JIS B7553 set the tolerance of +/- 1% to 1.5% based on the flume size.

An alternative solution to laboratory experiments has been introduced in recent decades by using Computational Fluid Dynamic (CFD) software, which allows the engineers and researchers to test their new designs using only computational power and resources. It prevents the necessity of providing the actual or scaled model of the proposed design to be tested. Advancement in the computing power of supercomputers provides a unique opportunity to scholars to test their designs and to be able to generate a realistic simulation of actual possible scenarios. It provides the ability

to amend, adjust and enhance the geometry of the proposed design, and at the same time, make the necessary adjustments to the possible flow scenarios, besides any modifications to geometry.

1.2 Numerical Simulation of Flow

Time dependency and multi dimensionality are characteristics of the turbulence phenomenon. Therefore, large amounts of data and information are necessary just to develop an introduction to turbulent flow. The ability of the available computer processors to simulate all practical flows are still unfeasible. Thus, a variety of statistical methods and approximations, which is called a turbulence model, is required [27]. To numerically simulate the flow of fluid in a hydraulic structure, i.e., an open channel, three approaches are introduced. A brief description of each is provided in the following sections. Figure 6 illustrate the hierarchy of the turbulence model.

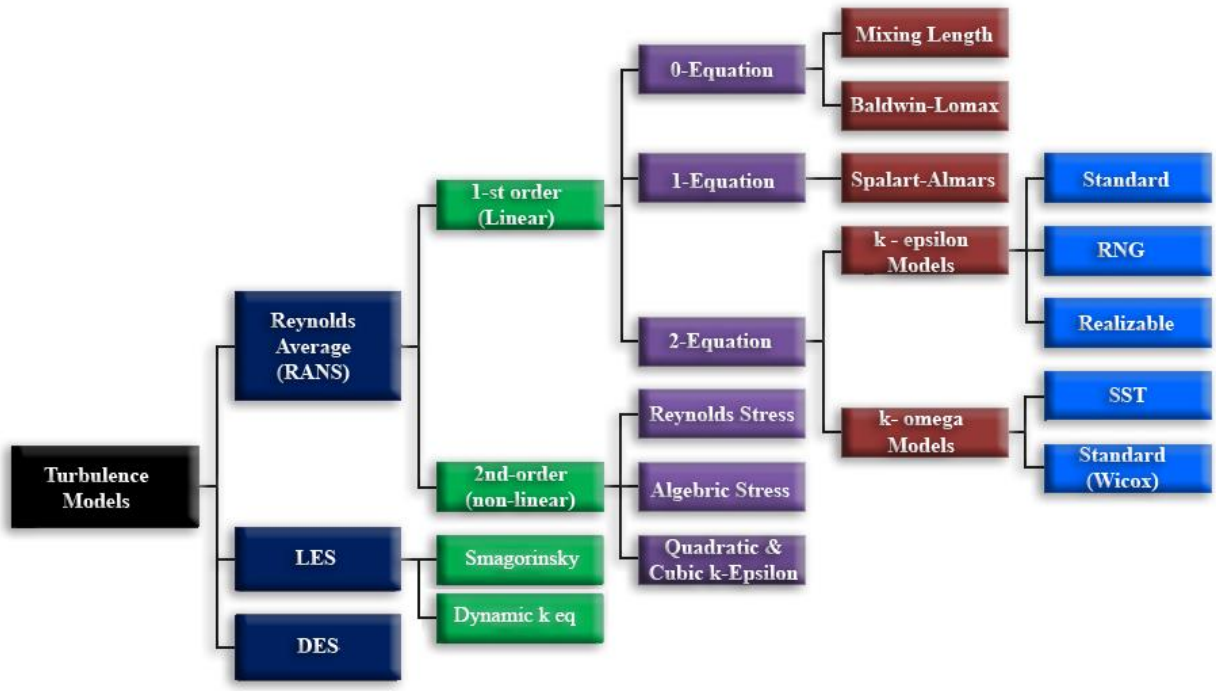

Figure 6: Turbulence model hierarchy

1.2.1 Direct Numerical Simulation (DNS):

In this method, with no extra modeling, only the Navier-Stokes equations are solved. Since the separation scale in turbulent flows is great, large numbers of grid points are necessary for practical

application. Since, for modelling purposes, the comparison or usage is only made between the average quantities, by the end of the simulation, it is necessary to apply statistical refinement for the 3-dimensional unsteady solutions.

1.2.2 Reynolds-Averaged Navier-Stokes equations (RANS):

It is a statistical action to solve the Navier-Stokes equations to obtain average quantities directly. The implemented methods in RANS are not considered numerical methods for small scales. The same behavior is also applied to the mesh requirement. RANS is widely used to reduce the testing number in modern design chains. In RANS, it is only required to model the correlations that appear when the non-linear terms of the basic relations are averaged. This is found to be extremely difficult, so nowadays, the non-existence of such an all-purpose turbulence model is accepted. This limits the potential of prediction of the RANS approach.

1.2.3 Large Eddy Simulation (LES)

This technique was introduced in the 1960s and the concept involves implementing the DNS approach for the large eddies in the main free stream of the flow while use the Navier Stokes approach for the boundary layer close to the rigid sections. This approach is believed to be an intermediate between the DNS and RANS approaches. It put more demand on the numerics compared to what is required in RANS, but less effort for the modelling is needed for the small scales due to their universality in nature. To address the important problems in simple configurations, it has been used generally as a DNS substitute [28]; LES has a high potential to be used in industrial simulations since it has reduced the cost of computation significantly [29]. A visual comparison between grid size used in DNS and LES is illustrated in Figure 7.

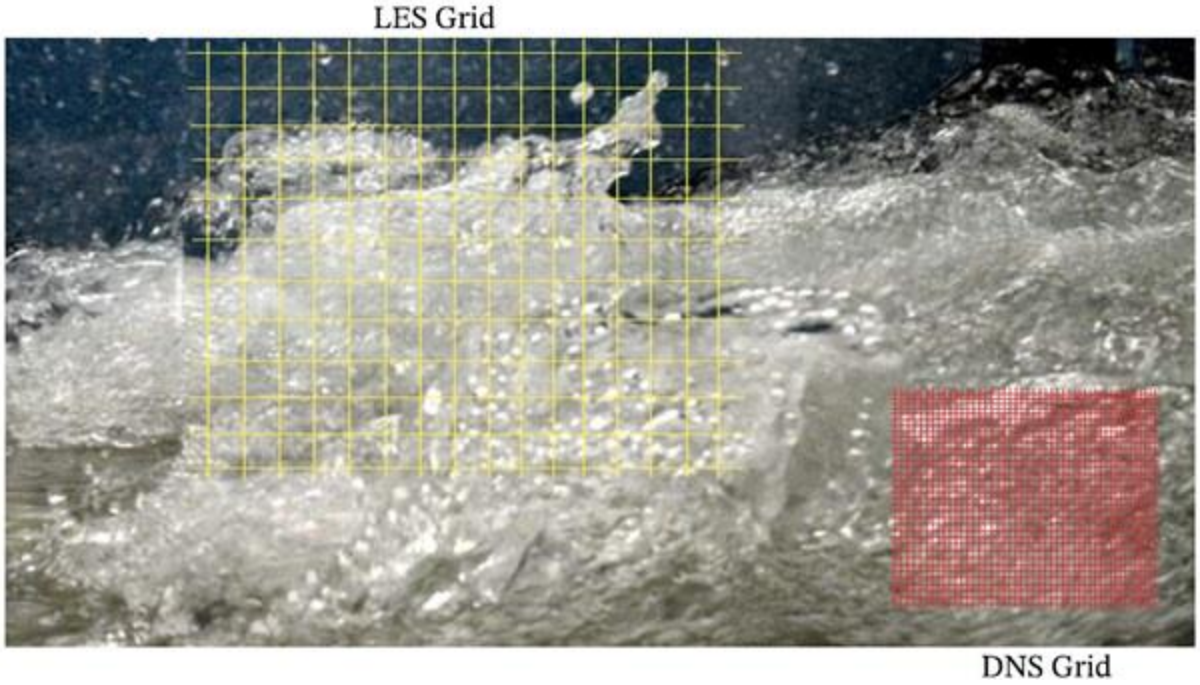

Figure 7: Visual comparison between DNS grid size and LES grid size [30]

1.2.4 Detached-Eddy Simulation (DES)

Due to the fact that close to the wall region the large-scale turbulence is physically small, especially where the flow has a high Reynold's number, grids with an appropriately fine mesh are essential. As a result, the cost of computation is excessively high and makes LES unapplicable to be used for engineering problems. The affordable solution is to develop different hybrid methods or the Detached Eddy Simulation (DES) approach. DES has a combination of all the advantages of RANS and LES.

The reason that this methodology is proposed, is to address the imminent necessity of solving the turbulent flows, particularly for those types of flow that are bounded with walls, and the very necessary fine mesh near the walls stops a full simulation of LES. For the turbulent structures in the near-wall within the viscous and buffer inner layers that consist of high-speed inflows and low-speed discharges (sometimes named the streak process) it is important for the structures to be resolved in the near-wall region. The major part of the turbulent production is generated by this streak process when the Reynolds number is low to medium. In LES, all of these turbulent structures must be completely taken into account to achieve a precise re-creation of the phenomenon. The computational resources required for an accurate LES simulation for a flow

within the walls with a large Reynolds number can be extremely large. To develop a RANS turbulence model, a tremendous amount of work needs to be undertaken to model the near-wall regions; therefore, it is logical to implement RANS models to capture the near wall turbulent structures instead of using high resolution LES. In addition, the RANS model is known for the spectrum of unsteadiness that comes along with the turbulent fluctuations distanced from the wall [31].

It should be noted that all the results in this thesis are time averaged.

1.3 Thesis Objectives

The numerical simulation of the flow in a Parshall flume is considered to be the main objective of this study. Meanwhile, the implementation of various turbulence models, i.e., 10 turbulence models consisting of linear and non-linear models, was carried out using OpenFOAM, the chosen open-sourced CFD, to find the most reliable water level data in the Parshall flume. The exhibition of a realistic flow simulation in the flume, constructed numerically and compared to the experimental results, supports further reliance on the application of CFDs for hydraulic structures. The motivation of this study is to provide the engineering community with a validated approach to simulate Parshall flumes for efficient and accurate design applications. Finally, it should be mentioned that submerged flow condition can happen due to downstream condition which is beyond the scope of this study.

1.4 Novelty and Contribution

This is the first study where computational fluid dynamic software has been used to model the flow in a small throat size Parshall flume i.e., 7.62-cm, using various turbulence models. The main novelty of this study is the use of both linear and nonlinear turbulence models.

In this study, the results from an experimental study have been reproduced using 4 linear turbulence models from RANS approach i.e., Standard $k-\varepsilon$, RNG $k-\varepsilon$, Realizable $k-\varepsilon$, $k-\omega$ and $k-\omega$ SST, 2 turbulence models from LES numerical approach i.e., Smagorinsky and Dynamic K equation, and a turbulence model from DES i.e., $k-\omega$ SST DES. In addition, as a main novel aspect of this study 3 nonlinear turbulence models have been used for the first time which include Shih Quadratic $k-\varepsilon$, Lien Cubic and v^2-f from RANS family. 99 preliminary simulations leading to 39 final simulations have been performed to evaluate the performance of the above-mentioned models mainly to extract the water level data. A comprehensive literature

review on the application of numerical models on Parshall flume has also been conducted and published. Implementation of the appropriate turbulence model has been investigated in order to obtain the most efficient and accurate design of the Parshall flume.

1.5 Thesis Organization

The thesis consists of 3 technical papers followed by a Conclusions section. The chapters are organized as follows.

Chapter 2 is a review paper with the title of "Application of Numerical and Experimental Modeling to Improve the Efficiency of Parshall Flumes; A Review of the State-of-the-Art", which provides an extensive literature review on similar studies related to this topic.

Chapters 3 and 4 deliver two article papers with the titles: "Numerical Modeling of Venturi Flume" and "Numerical Simulation of Flow in Parshall Flume Using Selected Nonlinear Turbulence Models". Both chapters provide enough evidence to support the objectives stated in the two papers. Various turbulent models were implemented to provide in-depth insight into the application of numerical simulation on hydraulic structures, i.e., the Parshall flume in this case.

Chapter 5 includes an overall conclusion on the "implementation of numerical modeling in flow simulation in hydraulic structures."

Chapter 2

Application of Numerical and Experimental Modeling to Improve the Efficiency of Parshall Flumes; A Review of the State-of-the-Art

2.1 Abstract:

One of the primary steps in managing the flow in an open channel is determining its properties. Empirical equations are developed to provide further information regarding the flow in open channels. Obtaining such experimental equations is expensive and time consuming; therefore, alternative solutions have been sought. Over the last century, the Parshall flume, a static measuring device with no moving parts, has played a significant role in measuring the flow in open channels. Many researchers have focused their interest on studying the application of Parshall flumes in various fields like irrigation and wastewater management. Although various scholars used experimental results to enhance the rating equation of the Parshall flume, others used an alternative source of data to recalibrate the height–discharge relation equation using numerical simulation. Computational Fluid Dynamic (CFD) software is becoming popular nowadays as computing hardware has advanced significantly within the last few decades, making it possible to go beyond the limited resolution that was experienced in the past. Multiple CFD models, depending on their availability, either open-source or commercially licensed, have been used to perform numerical simulations on different configurations of flumes, especially Parshall flumes, to produce water level results. Regarding various CFD tools that have been used, i.e., FLOW-3D, Ansys Fluent, or OpenFOAM, after precise calibration with experimental data, it has been determined that the output is reliable and can be implemented to the actual scenarios. The benefit of using this technique to produce results is the ability of the CFD approach to adjust the initial conditions, like flow velocity or structural geometry, where necessary. With respect to channel size and the condition of the site where the flume is located, the choices are narrowed to the specific Parshall flume suitable to the situation. It is not always possible to select the standard Parshall flume; therefore, engineers provide some modification to the closest flume size and provide a new rating curve to produce accurate flowrates. This review has been performed on the works of a number of scholars who targeted the application of numerical simulation and physical experimental data in Parshall flumes to either enhance the existing rating equation or propose further modification to the structure’s geometry.

2.2 Introduction

From ancient times, the allocation of appropriate amounts of water among the various sectors of society was a crucial task to be managed by local authorities. Different methods and devices were implemented to perform this task. As time passed, more accuracy was demanded as complaints arose about the performance of basic early measuring devices for water under field conditions such as open channels. Several parameters are considered when designing and building the ideal flow measuring device. According to Ref. [32], seven major criteria should be taken into account. Accuracy is the most important element, while the budget required to build such a device should be adequate. In addition, the device should also be easy to operate. The measuring device must operate for long periods with minimum maintenance costs and be free of any moving parts. Due to the low maintenance cost requirement, sediments and debris must be able to pass freely through without clogging the measuring device. Figures 8 and 9 show two different sizes of a measuring device called the Parshall flume.

Figure 8: Parshall flume measuring structure, installed[33].

Figure 9: Parshall flume measuring structure, uninstalled [34].

The Parshall flume is one of the measuring flumes that has been widely used over the last century. It is a modified Venturi flume that was first proposed by Parshall in 1936 when a negative slope was added to the flat bed of the Venturi flume at the throat section [35]. The flume worked on the principle of critical depth. The water enters at the convergence section of the Parshall flume and is guided through the wing walls at the entrance toward the throat section, the congestion part of the flume designed to accelerate the flow to achieve supercritical flow. The bottleneck was accompanied by the sudden steep drop in the flume bed followed by a negative slope that worked as a decelerator, starting at the beginning of the divergence section. Various modifications of the Venturi flume were studied over the years, but the Parshall flume gained popularity due to being well organized and accurate. Other flumes like the Cutthroated flume, a Venturi flume with no throat section, has a sudden transition between convergence piece and divergence part. The Montana flume, another modification of the Parshall flume, which only contains the convergence and throat section, is another example of a modified Venturi flume. In this modification, the divergence part is omitted as it was deemed unnecessary.

Regardless of which type of flume was chosen to measure the flow, the flowrate was derived from a mathematical relationship between the water level and discharge. The relationship was provided for each type of flume with different variable values due to variation in size. The quality of the physical experiment to derive the mathematical relationship for each flume directly affects the accuracy of the obtained flowrate. Therefore, with respect to various sources of error during physical experiments, it is difficult to neglect their results on the outcome. Human error and

uncalibrated device error were among the most common errors that have been improved over the last few decades by introducing more digital sensors instead of human observations. High precision manufacturing processes have now been implemented and are responsible for producing more accurate devices, i.e., measuring devices that result in fewer device errors.

Alternatives to the complicated procedures mentioned above have always been desired by engineers and researchers. More flexibility was needed in the design of such devices that worked under different circumstances. As one of the best economic solutions, moneywise and timewise, implementing numerical models to be run on super-computers to simulate the behavior of flow by solving the flow equations has drawn significant attention.

One reliable and fast approach introduced to substitute for physical experiments on hydraulic devices, i.e., Parshall flumes, is the Computational Fluid Dynamic (CFD) software. CFD models have been advanced within recent decades as computer processors have become more powerful. Different approaches to solve the Navier–Stokes equations of flow were proposed by various scholars over this period. Approaches like the Reynolds Average Navier–Stokes (RANS), Large Eddy Simulation (LES), and Detached Eddy Simulation (DES) were used by numerous researchers, and various secondary methods were proposed under each approach.

Using computational fluid dynamic software provides such accurate results that it eliminates the need of acquiring experimental observation. The purpose of replicating a downscaled physical model is to study the actual behavior of the specific structure under other flow conditions such that a proper safety factor is ensured in the design stage of a structure in order to withstand against any extreme conditions. For example, when designing dams, considering the possibility of having a large amount of rainfall that can occur with 100 or 1000 years return period is often required. Using numerical modeling made it almost unnecessary to use any type of physical material to build the downscaled model, while providing the freedom to take into account any unforeseen condition that might threaten the integrity of the structure in the short or long term of its life span. Additionally, it provides significant freedom to change the initial conditions, the boundary conditions, or make necessary changes to the computational mesh of the numerical model. Hence, CFD plays a significant role against under- or over-designed hydraulic structures that can affect the environment (aquatic ecosystem) or generate major dangers posed by their failure.

Based on several applications of different CFD models, the quality of the results in comparison to the actual laboratory tests were well accepted. Hence, the use of numerical simulation was approved by many scholars.

The objective of this paper is to (i) provide the reader with an introduction to the principles and applications of Parshall flumes, as well as to the most common types of modified flumes such as the Venturi and cutthroat flumes, (ii) present a typical algorithm to calculate the discharge using head discharge equation, (iii) specifically examine the work of previous researchers using numerical models to enhance the design and efficiency of the Parshall flume, (iv) examine selected previous studies on physical experiments to demonstrate the performance of their modifications to this type of flume; (v) present a comprehensive explanation of the various components of the numerical models used, including mesh generation, boundary conditions, initial conditions, postprocessing and error analysis, numerical methods, etc. Figure 10 illustrates the schematic design of a Parshall flume.

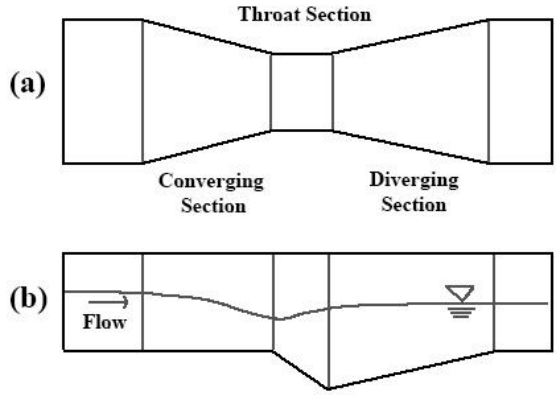

Figure 10: Sketch of Parshall Flume basic design (a) is top view and (b) is cross sectional side view.

2.3 Parshall Measuring Flume

In order to determine the discharge in open channel flow, various hydraulic structures are used, such as different types of weirs, orifices, spillways, as well as the Parshall measuring flume. Among different measuring devices, the Parshall flume provides more accurate discharge value by taking advantage of the principle of critical flow. The design of the geometry of the Parshall flume allows flow entering the throat section, a narrow section with parallel walls, due to the

gradual contraction of the entrance and the steep slope of the throat's bed, to be forced to change to critical flow, with a Froude number equal to one. Using the principle of critical flow leads to find more accurate discharge measurement in open channel flow.

One of the main advantages of the Parshall flume over other types of measuring devices is that the relative head loss is much smaller in the case of the Parshall flume when compared to the classical weirs. Additionally, the ability to pass the debris through is another important advantage.

The accuracy of some of the flume results are able to compete with those obtained from weirs i.e., ± 2–5%. Among different flumes, the Parshall and Montana flumes have exhibited ± 3–5% more accuracy than weirs, alongside cutthroat flume with a value of ± 3% [36].

2.3.1 Types of Parshall Flume

Various types of flumes were developed over the past century as measuring tools in open channel flow. One of the early measurement flumes are the Venturi flumes, which have three main sections: the converging, contraction, and diverging sections. As previously mentioned, the idea of using a specially-designed flume is to alter the flow into the critical regime. The contraction section of the flume is responsible to deliver this change to the flow.

The Parshall flume, a modified version of the Venturi flume, was the result of extensive modifications to the original design. The introduction of the bed elevation within the throat section accelerates the flow more efficiently compared to its predecessor (Venturi). Other researchers made various modifications to the Parshall flume by removing its diverging section (this was termed the Montana flume), and removed the throat section and named it the Cutthroat flume. The rating equations vary depending on the type of modified Parshall flume and flow conditions, i.e., free flow or submerged flow.

Free flow refers to the condition when the water level downstream of the flume has no effect on slowing down the overall flow speed. By contrast, the submerged condition is when the water level at downstream section increases and subsequently directly reduces the flow speed at the upstream section, hence creating a backwater effect.

2.3.2 Rating Equations for Parshall Flume

This section tries to provide some insight on the different mathematical relationships that were proposed to calculate the flowrate with respect to the widths of flume's throat and the type of flow, whether it is a free flow or a submerged flow. The key parameters in the equations are the head

value at a specific location along the flume (within the contraction section for free flow) or in submerged flow, the ratios of two head values at different locations i.e., a point within the contraction section (H_a) and another point within the converging section (H_b).

Parshall flumes with free flow condition from 1 to 8 ft. are designed following Equation (1) [37]

$$Q = 4WH_a^{1.522W^{0.026}} \quad (1)$$

where the discharge is denoted by Q (cfs), the width of contraction section is W, and H_a is the water level in the throat section. The equation works with imperial units.

Equation (2) is used for the same range flows, but for submerged flow conditions [37].

$$Q = 4WH_a^{1.522W^{0.026}} - \left\{\left\{\frac{H_a}{\left\{\frac{1.8}{K}\right\}^{1.8} - 2.45}\right\}^{4.57-3.14K} + 0.093K\right\} W^{0.815} \quad (2)$$

where K is the ratio of H_b/H_a (referred to as degree of submergence); H_a is the primary staff gauge reading while H_b is the secondary readings in feet. The equation works with imperial units.

Parshall [37] proposed Equation (3) for the flumes larger than 10 ft. in throat size up to 40 ft. with free flow condition;

$$Q = (3.6875W + 2.5)H_a^{1.6} \quad (3)$$

where Q is the rate of discharge (cfs), W is the width of flume throat, and H_a is the head measurement.

2.4 Numerical Modeling in CFD

In order to setup a computational fluid dynamic model, a few steps must be taken: Pre-Processing, Processing, and Post-Processing.

The Pre-Processing stage includes the mesh generation and defining the initial and boundary conditions.

Mesh generation is performed either by block-mesh (in OpenFOAM) or using other applications in order to provide a solid watertight mesh that has no flaws in terms of overlapping, gaps, or sharp angles.

As one of the key parameters to obtain an accurate numerical simulation model, the focus was on the appropriate selection of the cell sizes. This process is referred to as mesh sensitivity analysis. Figure 11 demonstrates the mesh sensitivity analysis performed by Ref. [38].

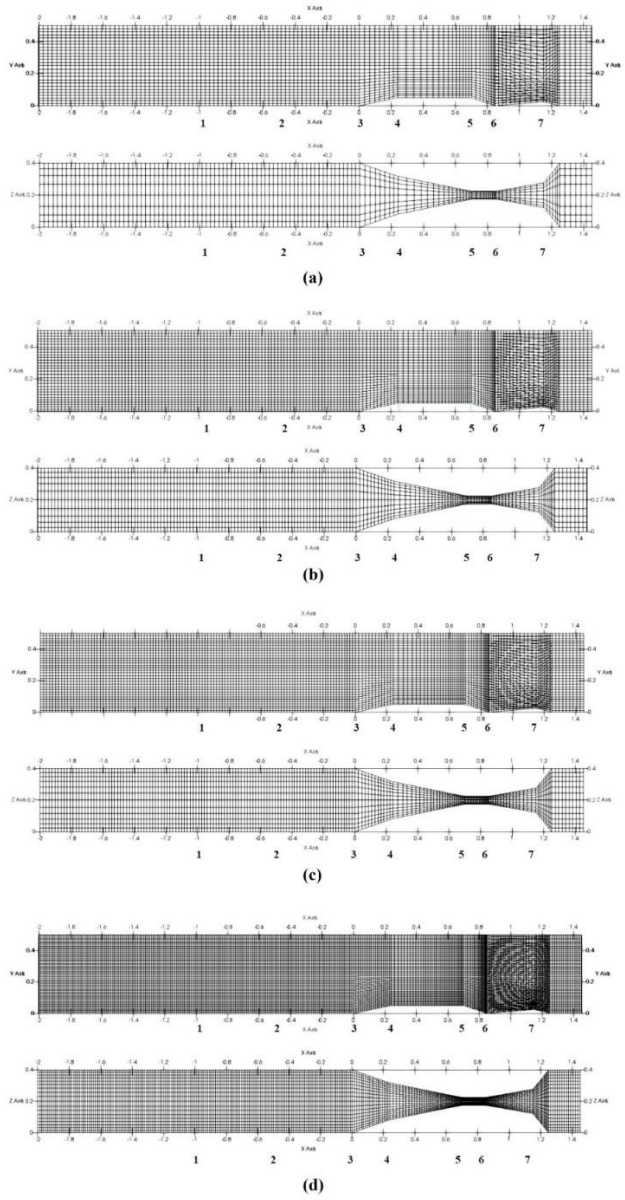

Figure 11: Mesh sensitivity analysis: top view and side view of the Parshall flume: (a) contains 27,000 cells; (b) 52,000 cells; (c) 75,000 cells; (d) 270,000 cells. The C setup was used in their simulation [38].

Boundary conditions are responsible for defining the properties of the computation domain edges in terms of permeability and specifying the point of entry and exit of the fluid in block-mesh. The atmosphere edge in the model is defined by boundary conditions as well. On the other hand, the properties of the flow at the entrance and exit (i.e., speed, direction, and acceleration) are set by initial conditions.

The processing stage uses various solvers to recruit different schemes (i.e., discretization of the interpolation terms), discretize the temporal term, the gradient terms, etc.

Post-processing involves the use of other software to interpret the results from the previous stage. Paraview, for example, [38,39] is used to plot the numerical results. As an example, it uses the streamline and contour type of plots beside the slice and threshold functions.

Finally, results from the numerical models are examined against available experimental result using various error analysis methods such as the absolute error method, the standard error of estimate (SEE), the root mean square error (RMSE), the central root mean square error (CRMSE), etc.

2.4.1 Governing Equations

The Navier–Stokes equations, a system of equations to solve the incompressible fluid motion in three-dimensional coordinates, is implemented in the numerical simulations by various CFD models. The system consists of equations for continuity and momentum. The Navier–Stokes equations are described as follows [40,41]:

$$\frac{\partial u}{\partial x}+\frac{\partial v}{\partial y}+\frac{\partial w}{\partial z}=0 \tag{4}$$

$$\frac{\partial u}{\partial t}+u\frac{\partial u}{\partial x}+v\frac{\partial u}{\partial y}+w\frac{\partial u}{\partial z}=-\frac{1}{\rho}\frac{\partial p}{\partial x}+\nu\nabla^2 u \tag{5}$$

$$\frac{\partial v}{\partial t}+u\frac{\partial v}{\partial x}+v\frac{\partial v}{\partial y}+w\frac{\partial v}{\partial z}=-\frac{1}{\rho}\frac{\partial p}{\partial y}+\nu\nabla^2 v \tag{6}$$

$$\frac{\partial w}{\partial t}+u\frac{\partial w}{\partial x}+v\frac{\partial w}{\partial y}+w\frac{\partial w}{\partial z}=-\frac{1}{\rho}\frac{\partial p}{\partial z}+\nu\nabla^2 w-g \tag{7}$$

where p denotes total pressure and ρ represents density, the velocity in three-dimensional directions is represented by u, v, and w, t denotes time, and g is the gravitational acceleration. The following equation is used to obtain the ρ value.

$$\rho=\alpha\rho_1+(1-\alpha)\rho_2 \tag{8}$$

The two involved phases, i.e., air and water, in fluid motion are represented by ρ_1 and ρ_2, respectively. Depending on where the point is selected, the α value varies from 1 to 0. The

presence of water requires $\alpha = 1$ while 0 represents the presence of air. The best value to represent the surface would be the average value.

And, finally, ∇^2 is obtained from Equation (9),

$$\nabla^2 = \frac{\partial^2}{\partial x^2} + \frac{\partial^2}{\partial y^2} + \frac{\partial^2}{\partial z^2} \qquad (9)$$

2.4.2 Equation of the free Surface

As the dominant method for analyzing the free surface, Volume of Fluid (VoF) is implemented in the majority of CFD models. Figure 12 shows the basic illustration of how VoF works within the mesh grid. As mentioned above, the assigned value for the full presence of air is 0, while in contrast, 1 is used when there is no air, i.e., the presence of water. Hence, the average value in between represents the zero-pressure boundary, i.e., fluid surface. The following equation is used by VoF:

$$\frac{\partial \alpha}{\partial t} + \frac{\partial(\alpha u)}{x} + \frac{\partial(\alpha v)}{y} + \frac{\partial(\alpha w)}{z} = 0 \qquad (10)$$

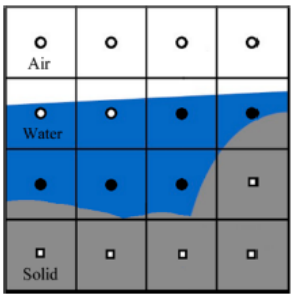

Figure 12: Illustration of VoF method (Reprinted with permission from Ref. [42]. 2020 ELSEVIER).

2.5 Literature Review

2.5.1 Numerical Studies

Ref. [39] studied the results of models using 7 different turbulence models to investigate which one performed the best when simulating a Parshall flume. The simulations were constructed based on experimental setup by Ref. [43] where the water level was recorded. OpenFOAM, an open-

source Computational Fluid Dynamic (CFD) software package was utilized to solve the flow equations. The turbulence models were chosen from three different main methods, i.e., Reynolds Average Navier–Stokes (RANS), Large Eddy Simulation (LES), and Detached Eddy Simulation (DES). The VOF method was implemented to reveal the boundary between fluid and air. Considering all different approaches to solve the flow equations, the performance of each turbulence model was evaluated by calculating the standard average error. This was done for 7 well-distributed cross-sections along the flume by comparing simulation results with experimental data. Results of the comparison revealed that the best performance was achieved with the standard $k-\varepsilon$ model from the RANS family, followed by the Dynamic one-equation approach from the LES approach.

Due to the variety of the turbulence models used in the study by Heyrani et al., the latter was considered to be one of the most comprehensive resources to study the application of numerical modeling in Venturi flumes, specifically the Parshall flume. Overall, the results from all turbulence models were considered acceptable due to the low error percentage values, i.e., less than 2.53%, where the highest was recorded for $k-\omega$ SST and $k-\omega$ SST-DES from RANS and DES families, respectively. The authors showed that due to the fluctuations recorded at the first cross-section, the average error percentage recorded was higher. Figure 13 shows the comparison between the numerical data versus the experimental results.

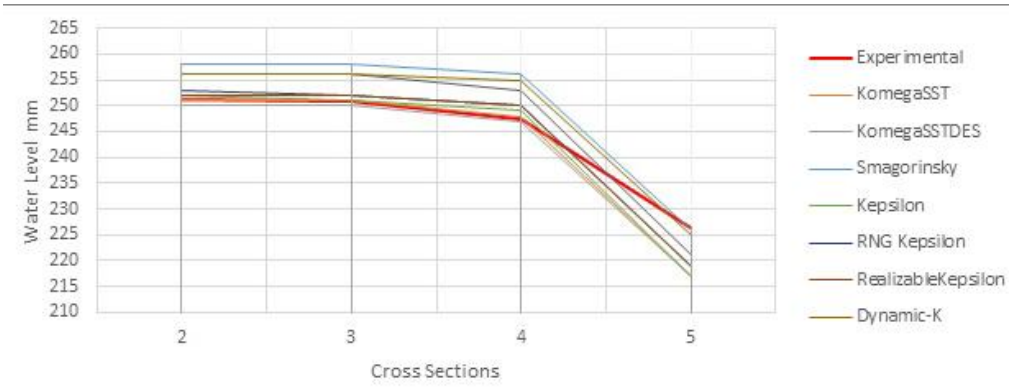

Figure 13: Comparison between numerical data and experimental results [39]

In conclusion, the application of numerical modeling as a tool to enhance the hydraulic design of hydraulic structures was highly recommended by Heyrani et al. [39]. This was mainly due to the

time and cost saving nature of the CFD approach. Additionally, the reasonably low computational resource allocation for numerical modeling of the Parshall flume made it a good candidate to be applied in order to rectify complicated engineering challenges.

The implementation of nonlinear turbulence models in OpenFOAM was pursued by Ref. [38] in conjunction with their previous comprehensive study on 7 linear turbulence models. Three different turbulence models, i.e., Shih et al. (1998) [44] Quadratic $k-\varepsilon$ Model (SQ), Lien, 1996 [45] Cubic Turbulence Model (LC) and v^2-f, from the RANS family were selected to simulate the flow in a modified 3-in Parshall flume. The modification was focused on the throat section parameters, i.e., the width, the length, and the overall bed drop of the throat. Various flowrates were used in the simulation model, as the experimental data were available in the other study, Ref. [39], mentioned above. A comparison was made between numerical and experimental data. The maximum average error was obtained by SQ model, i.e., 8.69%, while the v^2-f model provided an average error value of 1.79%, the lowest among not only the three nonlinear models used in this study, but also the seven linear models that were used previously by Heyrani et al. [39] in another study, with the same experimental setup.

The authors concluded that the use of CFD software with a non-linear turbulence model to simulate the flow in Parshall flumes was feasible due to the quality of the results and the amount of time spent to achieve them. The level of accuracy within not only the three nonlinear models, but also the other linear turbulence models used previously were considered acceptable, as all of the average error values were below 3% except the SQ model. Hence, it was recommended that the CFD results be implemented for any further modifications in the design of Parshall flumes, as the numerical simulations closely mimic the actual scenarios. Figure 14 is an example of what was discussed above regarding the numerical simulation reliability.

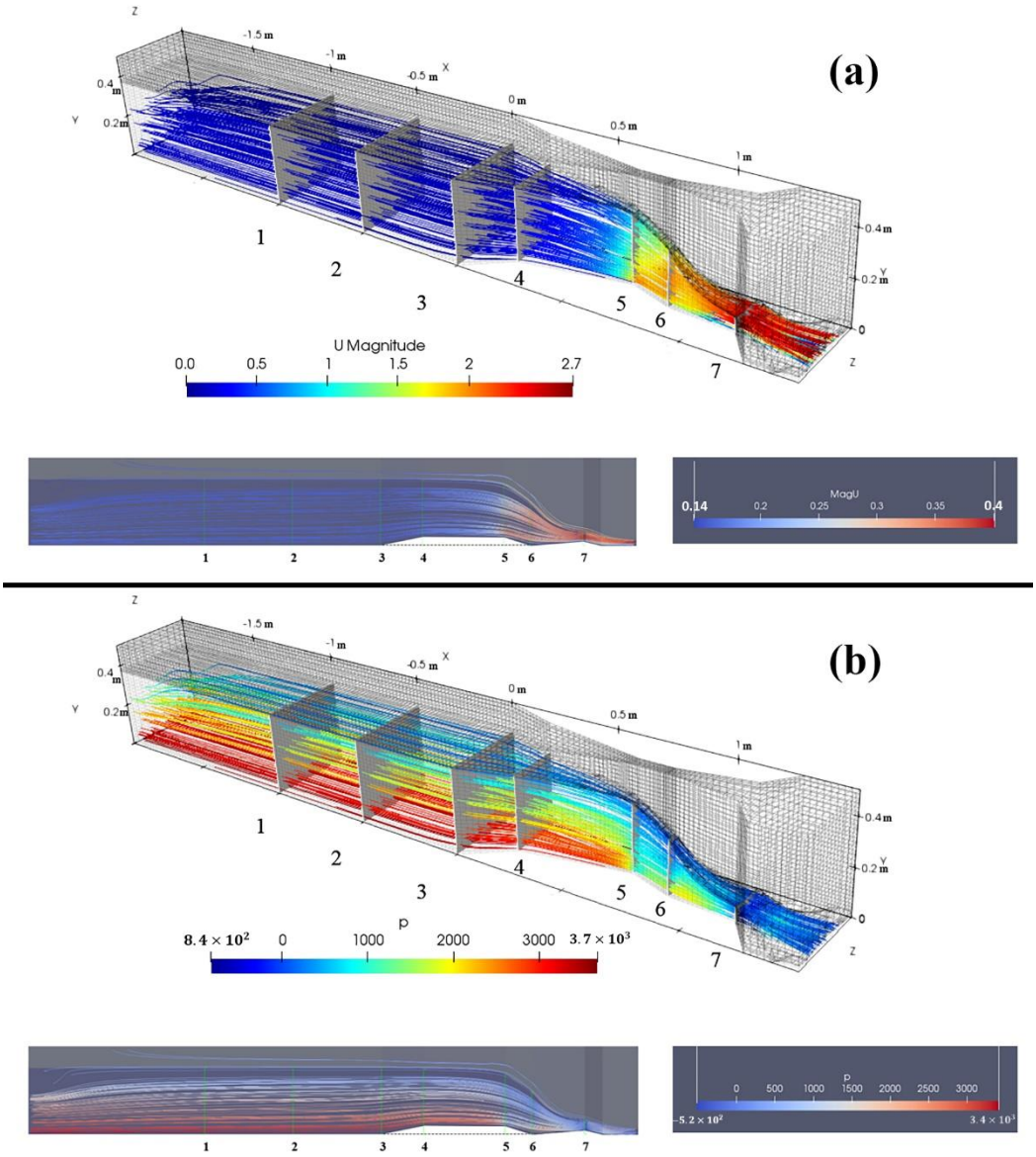

Figure 14: Simulated velocity (a) and simulated pressure pattern (b) across the Parshall flume. The patterns match the physical behavior of actual Parshall flumes [38] .

Ref. [1] conducted a study on the effects of nonstandard conditions with respect to Parshall flumes. The most common criteria that are neglected by scholars are the presence of longitudinal bed slope at the placement location and the existence of distortion in the velocity profile upstream of the flume's entrance. The Parshall flume used in Ref. [1] experiments was a 6-in flume. As a simulation tool, SOLA-FLUMP, a three-dimensional, free-surface finite-difference code was utilized to rectify the errors that arose due to such non-structural issues. The use of SOLA-FLUMP

is strictly limited to the cases where non-submerged flows are passing through Parshall flumes. The comparison of the simulation results and experimental data were reported to be good even though the viscosity parameter in the model was neglected.

Implementing a V-Notch Weir in the system provides a flowrate reading with an accuracy of up to 1.25% when calibration was done in place. There was a modification on the entrance wing-walls that made the flume geometry different from the standard one. One of the reasons for this modification was to improve the simplicity of the model's performance, while it was claimed that shifting the wingwall's location to 2.44 m upstream of the inlet entry point did not make any changes to the flume's overall performance. It was also highlighted that due to lack of computational resources, the numerical simulations were all performed on symmetric geometry around the centerline of the flume. Asymmetric simulations were possible to achieve with improvements of the computational hardware. The authors concluded that the SOLA-FLUMP code was accurate enough to be used as a resource to provide guidelines for the use of Parshall flumes in nonstandard situations.

Ref. [42] compiled numerous numerical simulations and physical experiments to investigate the accuracy of two field-scaled Parshall flumes placed in a parallel setup. The application of two flumes (0.91 and 1.22 m) was used as a tool to measure the flow rate in a wastewater system in Minnesota. VFS-Geophysics code, an open-source simulation model that was available in-house to the researchers, was used to develop the numerical simulations. Volume of Fluid (VOF), Large Eddy Simulation (LES), and level-set methods were also used as numerical tools to determine the water surface level and turbulent flow, as two-phase flow conditions were assumed. A combination of LES and level-set methods provided instantaneous water level values at any point in the flume. Overall, the study was conducted over four different flowrates, i.e., 500, 700, 1000, and 1500 L/s, where the total number of nodes in the grid system was reported as 6.5 million nodes. The experimental study was carried out using dye dilution method along with different flowrate measurement devices to determine the discharge passing through Parshall flumes. The authors reported that the best discharge results were obtained using an interval of one hour for time-averaged flow rate data. The main objective in the comparison of numerical results and experimental data in this study was to demonstrate that the numerical model is a reliable method of finding the margin of error of the full-scale flume under working condition; also, it is an applicable tool to determine the range of water surface level fluctuations over the Parshall flume.

The comparison between simulation results and experimental data showed up to 8% variation in one Parshall flume's rating curve, while the other one demonstrated a 3% error at high flow rates. The error increased up to 10% when low discharge was introduced to the second flume. Figure 15 illustrates the grid system on the Side A (right) Parshall flume in the parallel system.

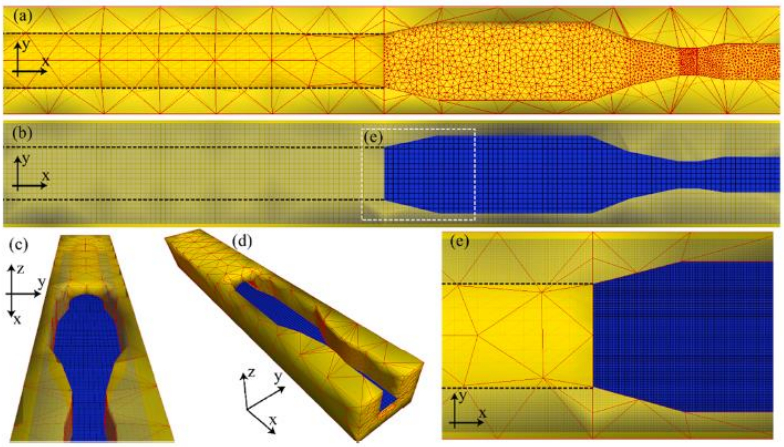

Figure 15: Computational grid system in the Side A flume. (a) contains a triangular grid system (b) demonstrates the rectangular grid system. (c) and (d) are three-dimensional schematics showing the superimposed grid system. (e) magnifies the dashed section in (b). (Reprinted with permission from Ref. [42]. 2020 ELSEVIER).

In a study by Ref. [3], the advantages of using a flume, specifically a short-throat flume, was explored. It was highlighted that the application of a flume or flume set with smaller size to provide more accurate discharge control at the inlet of the field was neglected by different researchers. The TruVOF technique together with the principles of critical flow were implemented in a 76 mm wide flume in FLOW-3D. The Re-Normalization group (RNG) $k-\varepsilon$ turbulence model was used in the numerical simulation to evaluate the hydraulic performance of the flume under 16 different conditions. The maximum discharge of up to 40 L/s was assumed during the experiments. Simulation results were then compared to the time-averaged flow field, flow pattern, Froude number, and velocity distribution. The results of the application of a portable short-throat flume revealed lower head loss compared to the long-throat flume. Moreover, free flow condition confirmed less head loss versus having submerged condition.

A short throat flume with a flat bottom was used in their study. There were, in total, 11 cross-sections considered as the data collection points, starting with 259 mm width at cross-section 1 to

178 mm width at the last cross-section. The throat size of 76 mm was recorded for cross-sections 5 to 9. The comparison of results indicated that a ± 10% error is unavoidable. In addition, the constructed regression model used to illustrate the relation between the upstream depth and discharge in various tested conditions showed an error of 9.16%, a value that is acceptable when it comes to the flow measurement in irrigation areas. With respect to the long-throat flume, the head loss of a portable short-throat flume in the field was determined to be considerably low. Further, head loss under the free flow condition was less than the one under the submerged flow condition of portable short-throat flume with a flat base in the field.

In another study by Ref. [46] , by developing a numerical model, the importance of consideration of the fluid viscosity was explored. The focus of the study was on flow with low discharge in a Parshall flume. As mentioned in the paper, the original rating equation by Parshall paid no attention to the fluid viscosity for low discharge flows. Therefore, a numerical model was introduced for four different sizes of Parshall flume to predict the fluid viscosity's effect on the depth–discharge relation. The use of the original rating equation along with several experimental data shows an overprediction of discharge. This happened for a discharge of around less than 15% of the maximum rated discharge for the flume. Moreover, inconsistency was up to 25% when the flume operated within its recommended flowrate. Therefore, the coefficients of the initial rating equation were reconstructed for low discharges using the numerical results. It was highlighted that the simulation results were in perfect accordance with experimental data.

The numerical model was constructed based on two concepts of energy conservation and the formation of the boundary layer on the sides and bed of the Parshall flume. The physical Parshall flume model used for experimental investigation could accommodate two different setups: 3- and 6-in, which acted as ¼ scale model of 1- and 2-ft setups. The flowrate was measured for each experiment with a calibrated Venturi meter, a separate procedure in addition to the main experiments. Alternative rating equation coefficients were proposed for various Parshall flumes when the flow is in submerged condition at low discharge, but it was recommended that the original Parshall's equation constants be used for higher flowrates.

Ref. [10] investigated the importance of maintaining the main design parameters as originally proposed for the Parshall flume. The proper design criteria from Parshall himself can lead to discharge accuracy of ± 3–5%. Meanwhile, the negligence of common parameters, such as specifying the correct location for head measurement upstream and the selection of the proper

wingwalls design at the entrance, caused the rating curve to be produced with inaccurate discharge results. As an example, a possible error of up to 60% was unavoidable when the submergence condition was not fully considered with no free-flow condition involved. In addition, measuring the flow head upstream anywhere but the specific location proposed by Parshall can also introduce an error of up to 60%. Therefore, to rectify the issue of applying nonstandard Parshall flumes in flow measurements over free-flow conditions, numerical simulation was utilized as a cost saving tool to provide numerus flow parameters over various sizes of Parshall flumes. The CFD results were investigated to provide a procedure to correct the flowrate for different sizes of flumes ranging from 2- to 8-ft. The application of CFD in this study was considered as an alternative to the traditional build–test method, which was considered inefficient with respect to over-allocation of some resources such as time and cost.

The results and procedures provided by Heiner and Barfuss followed the approach of collecting the head measurement at different points on the wingwalls and centerline anywhere within the convergence section except the standard location. For each flume size studied by Heiner and Barfuss, three different wingwall arrangements were considered, i.e., standard radius wingwall, 45-degree wingwall, and no wingwall. The CFD model used was FLOW-3D, while the VOF method was used to determine the boundary condition of the free surface. The FAVOR method was implemented to distinguish the boundary line between solid surfaces and the flow.

Ref. [4] validated the application of the numerical modeling by providing the correction coefficient for different sizes of Parshall flumes. Common problems in nonstandard Parshall flumes include dislocation of staff gauge and the presence of undefined entrance conditions such as different wingwall arrangements in the flumes, which can increase the calculated flowrate error up to 60%. Introducing a suitable correction factor, in the majority of cases, was able to produce results of (±) 3–5% in error and improve the biased data of the rating curve. The correction value was obtained by using data from a physical model of a 61 cm Parshall flume. Geometrical dissimilarity across the various sizes of Parshall flumes made it impossible to implement a single calibrated equation to remove the biases from the calculated flow rates of all nonstandard flumes. Therefore, numerical modeling was employed to rectify this problem.

Up to 18 cross sections within the converging area of a Parshall flume were defined to evaluate water level, while various wingwall configurations were introduced to the flume, i.e., radius of curvature of entrance wingwalls, 45-degree angled, and no wingwall. Multiple locations within the

cross sections were chosen to record the water surface data: at centerline, close to side walls, and at the sides attached to the stilling well. In total, 54 points were designated to be studied. The locations of the cross sections were selected based on the data collected during a field visit to the nonstandard flumes.

FLOW-3D was used as the CFD tool while the VOF method was implemented to provide the free surface of the flow. As wall function, the Fractional Area/Volume Obstacle Representation (FAVOR) method was chosen. In order to minimize the simulation time, the channel was only defined up to the beginning of the downstream section. Running the simulation only for the left side of the longitudinal centerline allowed further reduction in computational time since the geometry of the flume was symmetric. Due to the ability of RNG $k-\varepsilon$ model to simulate hydraulic jumps, this turbulence model was used in FLOW-3D. Based on 10 s time averaged data of water surface, pressure, and velocity, a small deviation was observed against the instantaneous data. Based on the study on wingwall configuration, a ± 5% deviation was expected to occur in the measured flow. The use of a numerical model was recommended by Ref. [4] , based on the good performance of the numerical results, i.e., deviation of 5% for 90 to 95% of the data, against bias corrected physical findings.

Ref. [47] investigated the sources of flow problems in short-throated flumes. The empirical models that were derived from physical experiments were pointed out to be a fundamental tool in constructing the rating curve of the flume. The quality and efficiency of the derived equation is in direct proportion to the size of the samples collected under different conditions, i.e., flume sizes and flow discharges. The conventional approaches, such as hydrostatic pressure method, were incapable of modeling the hydraulic characteristics of flows passing through Venturi flumes. Instead, a one-dimensional model was used to simulate the flow and clarify various characteristics of the flow, such as water level and pressure gradient over various sections. Finally, measured data were compared against the simulated data. The comparison between numerical and experimental data confirmed good model performance.

The study was divided into two main categories. For an open channel flow, a high-order model was developed with no consideration of pressure or vertical velocity assumptions for the flow. It was claimed that the one-dimensional model had higher computational efficiency than the 2D non-hydrostatic and quasi-3D numerical models. With respect to simplicity in application, it was considered as computationally efficient. The capability in providing the rating curve via a

convenient method for free flow condition in flumes like Venturi and Parshall made the proposed model even more competent.

The other pertinence of this study was the provision of numerical simulation for short-throated flumes with or without bottom hump. Total losses of energy considered in the study were due to the flow turbulence and roughness of the walls and floor, where it was believed that surface friction caused the majority of the losses. Overall, the results from the proposed one-dimensional model satisfied the free flow data in a Parshall flume as well as in the other short-throated flumes when compared with the 2D model results. Figure 16 illustrates the comparison of simulation results and experimental data.

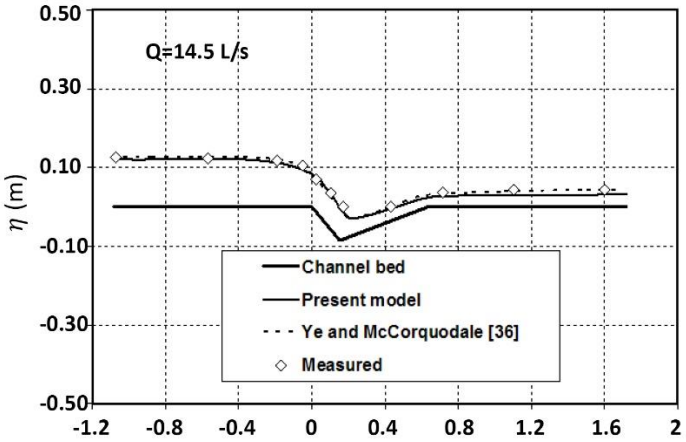

Figure 16: Consistency in the simulated data and physical results [47]

Ref. [2] studied available approaches to reduce the head loss in flumes by introducing three curve-designed flumes. The new flumes were formed as the result of alteration in the contraction ratio of the flume using the concept of critical flow to minimize the head losses. According to Ref. [2] , contraction ratio was defined as the ratio of the throat's cross-sectional area to the area of the channel's cross-section. A comparison was carried out for various hydraulic parameters such as water level, Froude number, velocity distribution, and head loss over the physical model and numerical simulation for curved flumes. The analysis revealed an overall error of 4.7% in the water level, which was considered acceptable. The results also showed a sudden decrease in discharge due to the submerged condition at the beginning of the divergence section. This happened shortly after the flow gained speed along the contraction section. A gradual increase in the contraction ratio resulted in a decrease in the depth of water and an increase in the Froude number upstream.

The best result of maximum head loss was 38.4% while 26.41 L/s flowrate was passing through the curved flume's throat with a contraction ratio of 0.4. It was emphasized by the authors that compared to other flumes, the results from curved flumes were superior. In addition, a new formula to provide the rating curve of the proposed flumes was constructed based on dimensional analysis method, and this led to accurate results.

Fluent software was used as CFD with implementation of VOF method to illustrate the free surface of the flow. Due to the presence of the curved surface within the flume, an unstructured mesh was chosen to define its geometry within CFD. The standard $k-\varepsilon$ turbulence model was selected to solve the flow equations for 12 different flow rates, i.e., 5 L/s to 27.19 L/s over three different curved flumes having various contraction ratios, i.e., 0.4, 0.5, and 0.6. The authors concluded that due to smaller head loss in curved flumes, higher flow capacity was expected to pass compared to the airfoil-shaped flume under the same conditions.

Ref. [9] used numerical modeling to simulate the three-dimensional (3-D) flow field in a Parshall flume and two other flumes using the VOF method. The data from physical experiments were used to evaluate the accuracy of simulated results in order to determine the efficiency of the CFD approach. FLOW-3D software was chosen as the CFD tool, while the standard $k-\varepsilon$ turbulence model was selected to simulate the flow. The implementation of FLOW-3D was due to its reliability, as verified by various researchers. A U-shaped channel with a radius of 0.2 and 0.45 m in depth was used to accommodate the Parshall flume with a throat size of 0.152 m and a contraction ratio of 0.763. The velocity of the flow and the turbulent kinetic energy were assessed at 4 different cross sections, with the flowrate set to 40 L/s. The largest error in the comparison was found to be 2.3 mm or 1.07%. The overall head loss of the Parshall flume was observed in the throat section and especially in the divergence section where the hydraulic jump was formed.

It was concluded that the head loss of the Parshall flume in a U-shaped channel was far greater than the other two flumes, i.e., 3.3 times bigger than the parabolic flume and 1.16 times greater than the long-throated flume. Therefore, the parabolic flume was found to be the most accurate measuring tool in the study. The rating curve relationship for different channel gradients was also proposed.

In a study by Ref. [5] , several parameters in four different flumes were numerically and experimentally investigated. ANSYS Fluent software such as the CFD tool and standard $k-\varepsilon$ turbulence model, along with the VOF method, were used to provide the results for 144 simulations

across various flume configurations with different contraction ratios. The correlation between the contraction ratio, i.e., 0.4, 0.5, and 0.6, the discharge, i.e., 4.83 to 27.15 L/s, and depth upstream, were analyzed. Figure 17 illustrates different setups on different types of flumes. The formula to evaluate the discharge was obtained through this correlation. To avoid the effect of flow fluctuations on the water level readings, the flumes were placed 3 m downstream in the 12 m long rectangular channel in the laboratory. The comparison was carried out across the flume's centerline for the discharge, and a few different constrains were used, such as: Froude number and water depth upstream, critical submergence degree, and velocity gradient, along with the head loss. In the critical state, the ratio of the water depth from downstream to upstream was considered as the critical submergence degree. The authors stated that in sewer monitoring systems and irrigation systems in agriculture, the lowest head loss and backwater were expected, while an acceptable large value of critical submergence degree is required.

Satisfactory results of the comparison of all four flume designs were reported. Figure 18 illustrates the basic schematic of the flumes used in this study. The head loss in the cutthroat flume was found to be the smallest while an error of 3.17% was recorded in the flume's discharge comparison. Overall, the variance in the simulation and experimental discharge values in all four flumes did not exceed 5%, which satisfied the discharge measurement requirements. It was concluded that with the simulation setup mentioned earlier, the comparison of experimental results and the numerical data showed that a 10% error was unavoidable. It was mentioned that more numerical studies can lead to the achievement of better flume shape designs.

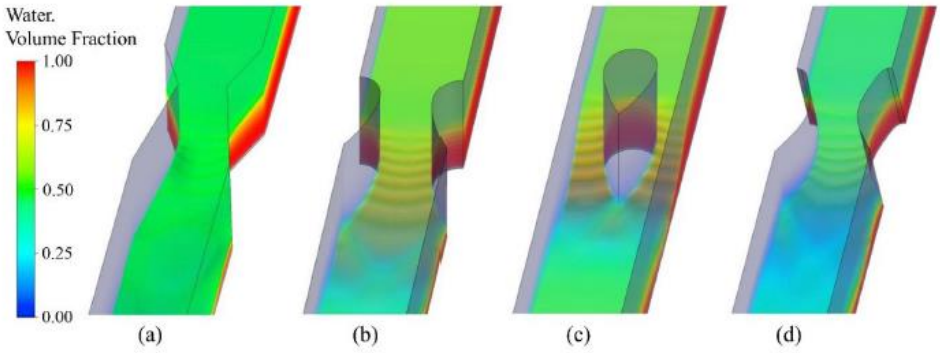

Figure 17: The results of flow patterns in different flumes; (a) Cutthroat flume, (b) airfoil-shaped flume, (c) airfoil pillar-shaped flume, (d) optimized airfoil-shaped flume [5].

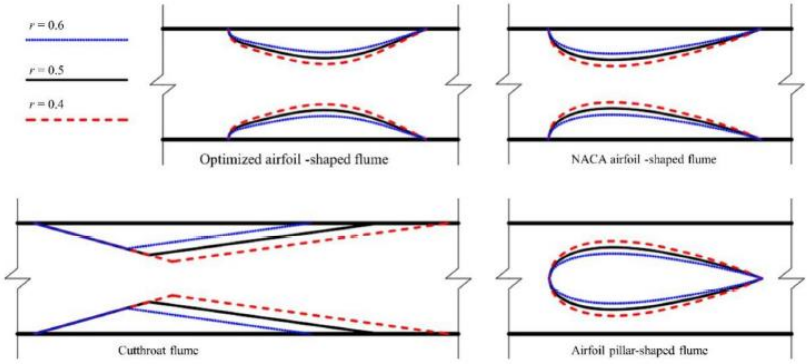

Figure 18: Experimental setup: contraction ratio used on each flume [5]

A study on the numerical modeling of a Montana flume, a Parshall flume with no divergent section, under submerged flow condition, was undertaken by Ref. [7] to calibrate and evaluate the accuracy of the flume. The motivation behind this research was the fact that numerous Montana flumes during several field visits were observed to have submerged flow condition while no adjustment is available for them. Based on the experiments carried out, the Montana flume under free flow condition provided very similar results to the Parshall flume in the same size class. However, when submerged condition is introduced, a discharge underestimation of up to 15% in the submerged-flow equation of Parshall flume was observed. Moreover, a discharge overestimation of 56% occurred when the free-flow equation of the Parshall flume was implemented. Therefore, an independent process to adjust the biased flow rate during submerged flow condition was illustrated by comparison between physical and numerical data on a 6-in Montana flume. Next, the method of calibration of the numerical model based on the physical data was extended to nine other Montana flumes with sizes of up to 8 ft under the same submerged flow condition.

The CFD model used in this study was FLOW-3D, while the turbulence model used was RNG $k-\varepsilon$ due to its reputation for for accuracy when defining the flows that have strong shear regions and low-intensity turbulent flow. For submerged flow condition of the Montana flume, the model reached steady state after 27 s, while it was mentioned that most simulations required only 15 s. To indicate different areas, i.e., water, air, or solid in the model, the VOF (Volume of Fluid) and Fractional Area Volume Obstacle Representation (FAVOR) methods were used. Additionally, a no-slip condition was used for the wall shear boundaries.

Since Parshall flumes cause a drop in water head, Ref. [6] proposed a new flume design. The flume, with no throat section, was to be installed in trapezoidal channels that were widely used in China for irrigation channels for agricultural purposes. Figure 19 provides the schematic of the proposed flume. To determine the efficiency of the new cutthroat flume, FLOW-3D software was implemented as the CFD simulation tool using the RNG $k - \varepsilon$ turbulence model. The method used to distinguish water from air at the surface of the flow was the TruVOF technique, while the mesh was generated using the Fractional Area Volume Obstacle Representation (FAVOR) method to define the rigid boundaries. Different flowrates of up to 75 L/s were applied in the simulation model in order to evaluate the hydraulic performance of the newly designed flume. To compare the simulated CFD result, physical experiments were carried out on the same size and condition of the cutthroat flumes defined in CFD. Acceptable errors of less than 10% were reported when the observed time-averaged flow rate and simulated flow velocity gradient were compared. It was also noted that the velocity near the walls was lower than the flow velocity at the center of the flume.

Increase and decrease were indicated in the results of averaged longitudinal flow velocity and Froude number, respectively, over convergence and divergence sections. As an example, a Froude number of less than 0.5 was calculated just before the throat congestion section. The objective of the study was achieved when the results indicated that only 9% of the total head was recorded as being lost. The cutthroat flume worked significantly better when the cross-section of the channel was trapezoidal compared to rectangular. In accordance with the relationship between discharge and upstream depth, a regression model was developed. Under various working situations, the regression model showed satisfactory results with up to 2.06% error, which was considered to be an acceptable relative value.

In conclusion, the authors strongly recommended the use of a trapezoidal cutthroat flume in order to improve the accuracy of the discharge measurement, while no significant flow head loss was expected to occur.

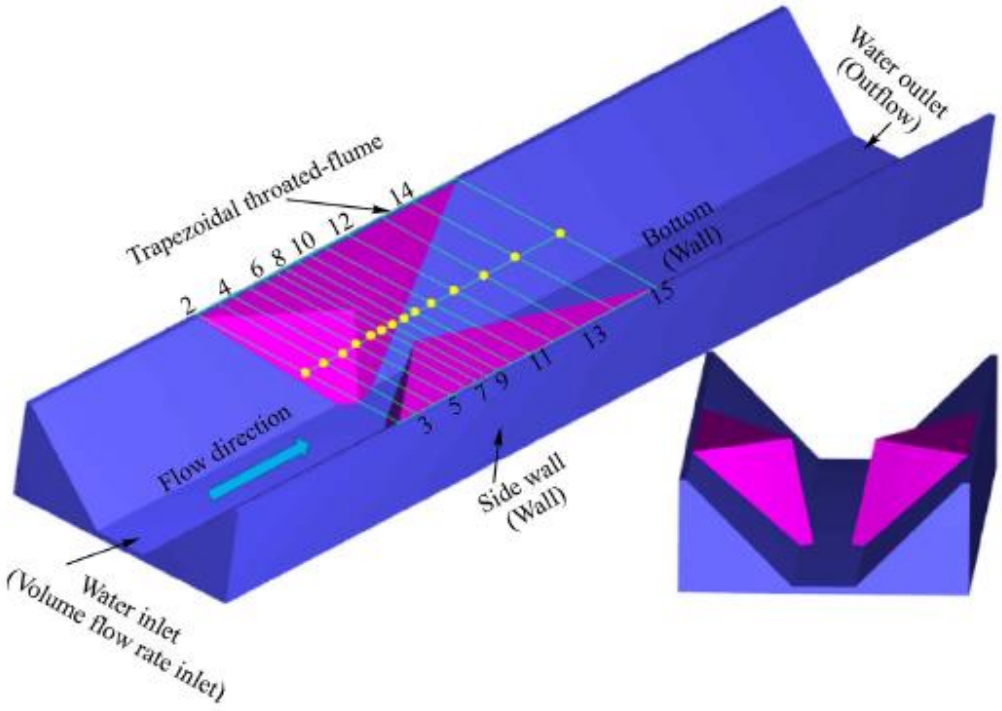

Figure 19: Entire flume geometry [6]

A study by Ref. [48] explored the application of numerical modeling in a Parshall flume to determine the appropriate size of the flume for different applications. The aim of this study was to use numerical simulation (FLOW-3D) to determine the efficiency of the empirical equation provided by the International Standard Organization (ISO) (ISO9826) for the Parshall flumes with low standard grades. The water level at the upstream and downstream ends were measured during the experimental phase.

The width of the water channel used for the experiment was 0.8 m while Parshall flumes with the throat section sizes of 0.3 and 0.152 m were placed into it. The entrance values of the convergence section were reported as 0.64 and 0.4 m, respectively, while 0.5 and 0.39 m were the widths of the downstream side of the divergence section, respectively. Unique boundary conditions at upstream and downstream ends of the flume with respect to the experimental setup were defined as well for the numerical simulation. The measurement of the flowrate was carried out using a triangular weir that was installed upstream.

The comparison between experimental and numerical simulation results revealed that the error was less than 4%. A new empirical model for flow was proposed using numerical simulation

results. The calibration of the new model using the measured flowrate exhibited an error of up to 2.3%. It was concluded that the low error value proved that the proposed model can be used to determine the proper size of a Parshall flume.

Ref. [49] investigated the use of a cutthroat flume to measure the discharge of the supercritical flow. In order to construct a suitable relationship, various physical experiments were done on the cutthroat flume to provide adequate amounts of data for regression analysis. Compared to the Venturi flume and Parshall flume, the application of a cutthroat flume was mentioned as being more popular in measuring the flow in open channels. This is due to the simplicity of its geometry; hence it is cost effective to construct this specific type of flume for supercritical flow. The proposed relationship between water head (H_a) and flow (Q) was developed based on regression analysis and it was demonstrated to perform well. It could be implemented in any cutthroat flume with the same specifications and still provide high quality results. In the experimental laboratory, a flume with square cross-section having dimensions of 0.6 m depth, 0.6 m width, and 21 m length was used to house a cutthroat flume with throat size of 0.34 m. The width of the converging and diverging sections was 0.58 and 0.36 m, respectively. To achieve supercritical flow and avoid any effect of the water turbulence on the cutthroat flume, the flume was placed 13.65 m downstream of the 21 m channel with the same slope of 1.05% for all the experiments.

It was concluded by the authors that if the supercritical flow formed at the throat section, the application of the cutthroat flume as a tool to measure the supercritical flow discharge was satisfactory. Therefore, it was deemed unnecessary to convert the flow type from supercritical to subcritical while measuring the discharge. With respect to the location where the supercritical flow formed within the flume, i.e., at the throat section or downstream of that section, two different relationships were proposed.

Ref. [11] performed extensive research on long-throated flume designs to increase flow measurement efficiency by implementing a software program. The application of a long-throated flume, due to its significant reduction of head-loss and low cost of fabrication, was proposed as an alternative solution for implementing various kinds of flumes with contraction sections. This revealed potential capabilities in measuring different flow types more economically and flexibly.

The calibration was done using computer software in order to eliminate the need for laboratory experiments. The possibility of creating non-modular flow in the flume where the ratio of the width to length of crest is relatively great introduced discrepancies between the numerical and

experimental data. Additionally, the generated suction effect at the end of the throat section that was observed during experiments affected the reading of that section, and this could easily influence the accuracy of the results provided by the rating equation for numerical and experimental results.

The proposed designs were calibrated to achieve the maximum accuracy. To achieve full potential of the flume, two essential parameters in each design were required, i.e., (1) providing enough freeboard, and (2) maintaining the Froude number in the approach channel as low as possible to guarantee a turbulent flow in the throat section.

In order to produce a successful long-throated design with width-contraction, FLOW3D was used by the US Bureau of Reclamation to simulate 4- and 2-ft modified Parshall flumes. Various flowrates were used in simulations to provide the rating curve that well described the relation between head and discharge in the long-throated flume. The comparison of the results from CFD and WinFlume software on an 8-ft Parshall flume revealed an acceptable error variation of less than 2%.

The authors also eliminated two common issues in the implementation of long-throated flumes. They recommended that adding a ramp at the control section could rectify the suction effect challenges, and that keeping the length to width ratio of the crest to 2:1 or higher can minimize the other obstacles to using the long-throated flume as an accurate measuring device.

Ref. [12] used the CFD approach to find a suitable contraction design on the flume to accurately calibrate the Acoustic Doppler velocity meters (ADVMs). The purpose of this research was to find the linear relationship between average velocity of the contraction's cross section and the sample velocity measured by the upward-facing ADVM. Accuracy improvement of the ADVM with elimination of the in-situ calibration was part of the objective as well. While the contraction section was removed from the flume, the flow was measured to calibrate the CFD software. The contraction section was responsible for creating the Rapidly Varied Flow (RVF), known as a non-uniform type of flow in the open channel that forces a rapid depth change over a small section of the flume.

The flume was 1.215 m in width and depth while having 86 m length with a 0.2% bed slope. The section occupied for this experiment as the testing region was 54 m in total length. It was capable of handling a maximum flowrate of 0.86 m^3/s. FLOW-3D was implemented as CFD software to

provide the appropriate design for channel contraction. Three different contraction setups were proposed and tested, using CFD to find the most appropriate design.

The surface roughness of the whole length of the channel was calibrated by comparing the velocity from the experimental test on 36 cross-sections against the numerical results corresponding to the same locations of the cross-sections. The roughness value ($k_s = 0.0002$ m) was iteratively set to achieve the minimum error in the comparison. This value was the exact value for the roughness of the steel's painted surface of the current flume used in this experiment. The results revealed that the Coefficient of Variation of the Root Mean Squared Error (CVRMSE) values for similar scenarios varied from 4 to 8%. It was concluded that the lack of CFD's ability due to the limitations of computer resources was one of the reasons for inadequate performance. The other reason was the existence of measurement errors known as the measuring device error.

Ref. [50] conducted a study to estimate the applicability of Parshall flumes (PF) and modified Parshall flumes (MPF) in determining the oxygenation rate of surface water. In this study, the usefulness of three different modeling techniques—artificial neural network (ANN), fuzzy logic (FL), and adaptive neurofuzzy inference system (ANFIS)—were examined.

The researchers used a dataset of 50 experiments. According to the results they obtained, the ANN model was found as suitable to predict the oxygen transfer efficiency E20 in PF and MPF. The ANN model also provided better predictive performance than the FL and ANFIS models. They also reported that the Gaussian membership function-based (MF) models had better results than the gbell MF-based models. According to the results of the sensitivity analysis, they suggested that q and K play important roles in estimating the oxygenation rate. Table 1 provides a summary of the papers using numerical method.

Table 1: Summary of the articles that contributed in the numerical category.

Categories	Article #	CFD	Turbulence Model	Flume Type	Standard/ Nonstandard	Free Surface	Wall Function	Submergence	Flowrate
Numerical	[38]	OpenFOAM	SQ/LC/ V2-f	Parshall	Nonstandard	VOF method	Standard	Unsubmerged	20 L/s
	[39]	OpenFOAM	7 Turbulence Models	Parshall	Nonstandard	VOF method	Standard	Unsubmerged	20–30 L/s
	[1]	SOLA-FLUMP	UNSPECIFIED	Parshall	Nonstandard	UNSPECIFIED	UNSPECIFIED	Unsubmerged	UNSPECIFIED
	[47]	1D-flow Simulation model	UNSPECIFIED	Short-throat	Standard	UNSPECIFIED	UNSPECIFIED	UNSPECIFIED	UNSPECIFIED
	[42]	VFS-Geophysics code	UNSPECIFIED	Parshall	Standard	VOF method	UNSPECIFIED	UNSPECIFIED	UNSPECIFIED
	[2]	Ansys Fluent	Standard K-Epsilon	Curved	Nonstandard	UNSPECIFIED	UNSPECIFIED	Submerged	5–27.19 L/s
	[3]	FLOW-3D	RNG Kepsilon	Short-throat	UNSPECIFIED	UNSPECIFIED	UNSPECIFIED	UNSPECIFIED	UNSPECIFIED
	[4]	FLOW-3D	RNG Kepsilon	Parshall	Nonstandard	VOF method	FAVOR method	UNSPECIFIED	UNSPECIFIED
	[46]	UNSPECIFIED	UNSPECIFIED	Parshall	Standard	UNSPECIFIED	UNSPECIFIED	Submerged	UNSPECIFIED
	[5]	Ansys Fluent	Standard KEpsilon	Cutthroat	Nonstandard	VOF method	UNSPECIFIED	UNSPECIFIED	4.8–27.15 L/s
	[6]	FLOW-3D	RNG Kepsilon	New design	Nonstandard	TruVOF method	FAVOR method	UNSPECIFIED	up to 75 L/s
	[7]	FLOW-3D	RNG Kepsilon	Montana	Standard	VOF method	FAVOR method	Submerged	UNSPECIFIED
	[48]	FLOW-3D	UNSPECIFIED	Parshall	Nonstandard	UNSPECIFIED	UNSPECIFIED	UNSPECIFIED	UNSPECIFIED

[9]	FLOW-3D	Standard KEpsilon	Parshall	Standard	VOF method	No-Slip	UNSPECIFIED	40 L/s
[10]	FLOW-3D	UNSPECIFIED	Parshall	Nonstandard	Yes	Yes	UNSPECIFIED	UNSPECIFIED
[12]	FLOW-3D	UNSPECIFIED	Contraction flume	Nonstandard	UNSPECIFIED	UNSPECIFIED	UNSPECIFIED	UNSPECIFIED
[11]	FLOW-3D	UNSPECIFIED	Modified Parshall	Nonstandard	UNSPECIFIED	UNSPECIFIED	UNSPECIFIED	UNSPECIFIED
[50]	Regression Analysis	UNSPECIFIED	Contraction flume	Nonstandard	UNSPECIFIED	UNSPECIFIED	UNSPECIFIED	UNSPECIFIED

2.5.2 Experimental Studies

The application of a small Parshall flume to measure supercritical flow was investigated by Ref. [51]. Experiments with multiple configurations, i.e., 15 different setups, were performed for 82 test conditions to study the accuracy of the results of two different sizes of Parshall flumes, i.e., (15.24-cm) 6-in and (22.86-cm) 9-in. In order to modify the flume's relationship, alterations in various parameters such as approach channel slope, roughness, and flume convergence were considered. To provide conditions for 82 experiments, various slopes ranging from 4 to 7% were incorporated, with different flowrates from 0.028 to 0.112 m^3/s for two different flume sizes along with changes in other parameters of the flow.

While the flow was maintained in unsubmerged condition, the accuracy of the flumes to measure the supercritical and subcritical flows was determined to be ± 5%. The relationship used to measure the flow in the flume was enhanced to incorporate various parameters such as channel slope, roughness, and the condition of the convergence section. To determine supercritical flow, an equation was proposed. Additionally, in order to distinguish properly between different regimes of flow, a Froude ratio indicator was established.

The developed relationship was applicable only to Parshall flumes with throat width sizes of 12-in or smaller while flume slopes of up to 7% were considered in the process of collecting experimental data; hence, it is not recommended to use the equation for larger gradients. The Parshall flume was located 12.2 m downstream in a 0.61 m wide, 18.3 m long channel with adjustable bed slope. The condition of the approach flow was determined by various parameters

within the upstream section of the flume such as roughness. Overall, 13 cross-sections were chosen to record the water surface elevation.

The authors concluded that it was not possible at that time to come up with one single relationship for both flow regimes, i.e., supercritical and subcritical; instead, for each flow type, different equations were developed. In addition, it was important to carefully observe the condition of the hydraulic flow at the beginning and/or the end of the converging section. As an example, based on the observations during the experiments, the hydraulic flow condition could affect the creation of the hydraulic jump further downstream of the Parshall flume while the same configuration was followed.

In a study by Ref. [43], the performance of a modified 3-inch Parshall flume was investigated in relation to the process of flow aeration. The lack of highly turbulent flow in rivers and man-made channels causes a reduction in Dissolved Oxygen (DO) ratios. The introduction of hydraulic structures such as throated flumes, cascades, and weirs has been proposed as a solution to this problem in channels and rivers. In the experimental setup used by Ref. [43], deoxygenation took place chemically in a storage tank at the beginning of the system. The DO was measured upon entrance and exit of the flume in order to record the increase in DO after the flow passed through the flume.

Flumes were installed in a rectangular channel with dimensions of 0.4 m in width and 0.6 m in height with the length of 5 m. Fluid with various flow rates, i.e., 10, 20, 30, and 40 L/s, were set to pass through 27 modified Parshall flumes. With respect to flow in critical regions of the flume, eight locations were selected to collect the water level data using a mobile digital point gauge. The shape variation of the Venturi flumes was specified based on the size of their throat width, throat length and the sill height. The results of water surface level and DO were recorded in the study for a total number of 108 physical experiments.

It was concluded that in channels having low or zero gradient, the implementation of Parshall flumes or any type of throated flume capable of introducing turbulence to the flow was recommended by the author. The presence of hydraulic jump that was caused by the flume geometry design was one of the key elements in the DO increment process.

Ref. [52] used a 5-ft full-scale Parshall flume to determine an accurate relationship to estimate discharge of supercritical flow. The objective of the study was to evaluate if Parshall flumes with various sizes greater than 12-in could be sufficiently calibrated to determine the flowrate of

supercritical flows. Across 11 different experiments, i.e., 3 subcritical and 8 supercritical, the discharge range was set between 3.07 and 30.15 cfs, and the variation in Froude number was recorded as between 0.67 and 1.31. A comparison of the experimental data with the results of the current equation used for subcritical and supercritical flows led to the development of a new rating relationship that was applied for only supercritical flows in large Parshall flumes.

In the experimental setup, the Parshall flume was placed downstream of a 17.1 m length channel with the width of 4.88 m and a slope of 4.38%. The water level and velocity were measured at three points on the center line of the flume, in addition to 16 different cross-sections that were located in the upstream channel.

The rating equation provided acceptable results when used for Parshall flumes with sizes similar to the one chosen in this study. It was mentioned that unsubmerged free-flow condition was considered during all experiments. It was concluded that accurate flow measurement with various sizes of Parshall flumes, i.e., up to 5-ft, for different types of flow, especially supercritical flow, was possible with only 4.52% error. It was also recommended to perform physical tests on different sizes of Parshall flumes, i.e., 9-in and greater up to 5-ft, to validate the derived relationship for supercritical flow.

Ref. [53] worked on the determination of uncertainty in flow rate measurement with Parshall channels. They used the Monte Carlo Method (MCM). The researchers presented the main uncertainties and explained the mathematical models and parameters. They reported the measurement uncertainty components with the help of MCM simulations.

In their study, the input sizes and the uncertainties of the measured flow rate were evaluated separately. Regarding the measurement uncertainty, they considered the following parameters: reference equipment calibration; repeatability; resolution of both the reference equipment and the equipment installed in the calibrated system; zero setting; linearity of scale; aging deviations and bias; vertical angular deviations (longitudinal and transverse); air temperature compensation (correction applied to the speed of sound); pressure and vapor pressure in the air; echo interference (noise interference); surface irregularity (due to unstable flow conditions); fluid properties (viscosity, density, non-Newtonian behavior; etc.); sub-surface thin layers of sediment; and stability of the installation (influence of wind and other sources of vibration).

The researchers showed that the common use of fixed model parameters underestimates the uncertainty of measurement, ranging from 8 to 12%, depending on the correlation effect.

Ref. [54] produced different sizes of Parshall flumes with different throat widths and tested them in the laboratory under free flow conditions. They determined the discharge coefficient and exponent and developed a single equation for different channel sizes.

The researchers tested four different sizes of Parshall flumes with throat widths of 0.052, 0.076, 0.152, and 0.229 cm in an open channel measuring 9.45 × 0.60 × 0.55 m. They measured upstream heads and velocities in the experiments.

According to the results of their experiments for flow rates ranging from 0.004 to 0.138 m3/s, they proposed a new empirical formula that provides the depth–discharge relationship. They reported that this equation is suitable for simple and small Parshall Flumes under free flow conditions. In their paper, four different sizes of Parshall flumes, having different throat widths were fabricated and tested in the laboratory under free-flow condition. The coefficient of discharge and exponent were determined and a single equation for the different flume sizes was developed. The relationship is simple and suitable to use for small Parshall Flumes.

Ref. [8] performed a study to accurately estimate the flow rate of a low flow season in Korea. They used a Parshall Flume and reviewed its applicability. In their study, they installed a Parshall Flume in an actual river and measured the flow rate obtained from the flow rate formula and velocity measurements, which were stated to be very accurate when compared to the flow rate computation results. They estimated the flow rate and compared it with the actual flow rate of the Parshall Flume.

They mentioned that in comparison with the directly measured flow rate as measured by flow velocity, the flow rate measured by the Parshall Flume possessed higher accuracy. The researchers reported that the flow rate formula based on the state discharge rating curve equation results showed an error of approximately 14%. They also stated that the usage of calculation by the state discharge rating curve equation at low flow rates leads to a greater error than the Parshall Flume, and in order to calculate the accurate low flow rate, the flow rate measured by the Parshall Flume should be preferred.

As a result, the authors concluded that the flow rate measured by the Parshall Flume had a very high accuracy and reliability.

Ref. [55] studied the Parshall flume and the Montana flume, which have the same calibration procedures under normal free-flow conditions, and tested their calibrations under submerged flows.

They conducted the tests at the Utah Water Research Laboratory in an acrylic 15.2 cm (6-in) flume. The researchers stated that the standard Parshall flume rating curve overpredicted flow rates in the submerged Montana flume by up to 48%. They also stated that Parshall submergence corrections were applied to the submerged Montana flume, and flow rates were under predicted by up to 19%. The study developed submerged flow rate correction factors specifically for a Montana flume, and the paper also demonstrated how to apply the corrections.

Ref. [56] aimed to determine the limits of application of traditional critical flow theory in the study of Venturi flumes. The researchers conducted this study to account for the influence of the slope and curvature of streamlines on the head–discharge relationship in Venturi weirs with short throats, and to evaluate the discharge coefficient as a function of the radius of curvature of the upstream energy, throat length, throat width, and inlet arc constriction. They proposed an empirical equation. As a result of the study, they reported that this empirical equation is valid up to a deviation of 8% compared to the traditional approach and can be used in engineering applications. Table 2 provides a basic summary of the experimental studies.

Table 2: Summary of the articles that contributed to the experimental section.

Categories	Article #	Flume Type	Standard / Nonstandard	High/Low Discharge
Experimental	[43]	Parshall	Nonstandard	Low to High
	[51]	Parshall	Standard	UNSPECIFIED
	[52]	Parshall	Standard	Supercritical flow
	[49]	Cutthroat	Standard	Supercritical flow
	[53]	Parshall	Nonstandard	UNSPECIFIED

2.6 Discussion

Based on the thorough analysis of various studies concerning the measurement of flow in open channels using Parshall flumes and other similar types of flumes, it should be emphasized that the majority of the numerical modeling studies were carried out on nonstandard Parshall flumes rather than on the standard ones.

Various turbulence models have been used by different scholars. Among the researchers, Refs. [2,3,5,9,38,57], the $K-\varepsilon$ turbulent model, both the standard and RNG versions, are implemented the most. It has been applied to the standard Parshall flume, cutthroat and short-throat flumes. Heyrani et al. 2021 [39] extended the use of $K-\varepsilon$ model by implementing another version of the $K-\varepsilon$ turbulent model, i.e., realizable $K-\varepsilon$ beside the earlier versions. In one specific case, the $K-\varepsilon$ model was used by Sun et al. 2020 [2], for a modified flume with curved contraction walls. The results demonstrate good correlation between numerical and experimental findings. Considering the various articles reviewed in this paper, it is found that the $K-\varepsilon$ model is deemed to be the most reliable turbulence model among different turbulence models like $K-\omega$, Smagorinsky, etc.

In an overview of the numerical articles that implemented computational fluid dynamic software, using the three-dimensional modeling was outlined in few articles [5,6,38,39,42]. The possibility of generating a 3-D mesh and solving the flow equation in three-dimensional modeling is due to the advancement of the computer processors within the past decades. The volume of calculations is in direct proportion to the desired resolution for the models. Using higher resolution will result in more explicit findings. The Large Eddy Simulation (LES) and Detached Eddy Simulations are addressed in Ref. [39] and provide quality results, since in these methods the presence of small eddies is considered in the calculation. Therefore, it is recommended to choose fine mesh size in LES and DES modeling to be able to get more accurate findings on the mechanics of the flow.

Application of non-linear models by Ref. [38] shows promising results with the least error possible in comparison to the linear methods that are used by other scholars in different studies. Additionally, the VOF method to determine the water surface level is implemented by the majority of the researchers [5–7,9,38,39,42,57].

Most of the articles in the numerical section are focused on numerical simulation of either Parshall flume or its modified versions, such as cutthroat and short-throated flumes. On the other hand, Montana measuring flume was only used by Ref. [7] to be simulated numerically while the submerged flow condition was experienced. This is due to the lack of studies of the behavior of Montana flume using numerical models in different articles. Therefore, in future studies, it is recommended to focus more on Montana measuring flume as well.

According to Ref. [46] and Ref. [52], the Parshall flume's rating equation does not work accurately when there is supercritical flow, and it is unreliable when low discharges pass through the flume

since the presence of fluid viscosity is neglected in the equation that was first proposed by Parshall himself. Therefore, improvement of the height–discharge relationship, known as the rating curve, in the standard Parshall flume will increase the efficiency of the system in the design stage when precise information is demanded for further adjustments for its various applications, i.e., wastewater treatment plant design or design of a specific hydraulic structure.

According to the investigation of the articles mentioned, there is limited use of various turbulence models in numerical simulation in the literature. More studies should be conducted on the application of not only RANS models, but also of the LES and DES models in order to provide in-depth information regarding turbulent models from all major methods. Apart from the articles by Heyrani et al., 2021 [38,39], the rest of the researchers used either the standard $k-\varepsilon$ or RNG $k-\varepsilon$, or otherwise did not specify the turbulence model they implemented in their study. Providing a comprehensive study, covering all the appropriate turbulence models will be crucial for the future use of CFD.

In addition, it was found that due to limitations in numerical simulation resources, i.e., insufficient computational hardware, some researchers preferred to perform only partial simulations. Therefore, the reliability of the results has more room to be improved. The use of different CFD models was also observed in various cases as some used commercial software while open-source software was implemented by others. The accessibility of CFD to a wide range of researchers is quite important. Therefore, more flume related applications of open-source CFD models like OpenFOAM are recommended due to their availability to a vast number of people.

Some of the researchers relied on the results from numerical simulations with no further verification against the experimental data. Therefore, with respect to the available resources, the use of experimental data is recommended in addition to the simulation results.

One of the highlights of using numerical simulation to study the behavior of flow in open channels is the freedom to choose the appropriate size of a Parshall flume depending on different conditions. Simulating flow in a Parshall flume can help engineers to efficiently select the proper size of a Parshall flume suitable for specific situations.

One of the parameters used to assess the quality of the experimental or numerical studies is analyzing the effect of various input values on the model. Among the articles that were reviewed in this paper, a number of scholars [2,5,6,9,38,39] specified more details of the inputs that were

assumed, such as the flowrate value, while there is a large gap identified in other researchers' work with respect to detailed parameters specifications.

As a first step in setting up a numerical model, it is important to define a sealed mesh with no gaps and overlaps. In order to build up the mesh, two options are available: either choose a structured mesh, where the dominant shape of the mesh cells is organized, or use an unstructured mesh, e.g., with triangular/tetrahedral geometry of the mesh cells. Depending on the geometry, it is recommended to choose an unstructured mesh such as in the work of Khosronejad et al. [42] and Sun et al. [5] where, due to the shape of the block-mesh, the researchers used unstructured meshes. In a previous study by Heyrani et al. [38,39] and Ran et al. [6], due to the straight edges and surfaces of their modeled hydraulic structure, the structured mesh was chosen.

While the mesh of the geometry is constructed by block-mesh or other types of software, one should carefully deal with the boundary between the structure and the water in contact with various surfaces; this is termed as wall tracking algorithm. The VOF method presented earlier in this paper demonstrates this technique to differentiate the interface between the water and atmosphere. Another type of joint surface in numerical model is when the flow flows through the hydraulic structure, i.e., passing the water flow from Parshall flume. The Fractional Area Volume Obstacle Representation (FAVOR) method was used by various scholars [6,7,57], while Boundary Fitted Mesh method implemented by Refs. [2,5,38,39] delineates the boundary between the flow and any rigid object in the path of the flow.

Various CFD software were used by scholars and engineers to solve flow equations for various flow measuring devices. As mentioned earlier, the resolution of mesh is essential to provide as accurate as possible results. Using a powerful computer processor can determine whether, with a given resolution of the mesh, it is possible to capture the smallest eddies or not. The accessibility of the current CFD software in the market is also directly determined by the availability of the software to the target audience. One of the parameters to choose the CFD model is to consider the price paid for its license, whether it is an open-source software like OpenFOAM or if it is a licensed registered software like FLOW-3D. Although there has not been any study to compare their capability in numerical modeling in the context of Parshall flumes, considering the same block-mesh, initial conditions, boundary conditions, numerical method, etc., depending on the computational resources available to the researcher [38,39] it is preferable to use open-source software such as OpenFOAM, while the FLOW-3D is the chosen CFD by some other scholars.

2.7 Conclusions

This review has covered numerous articles focusing on implementing numerical modeling to enhance the efficiency of Parshall flumes or Cutthroat flumes, and others based on the physical experimental results they all tried to validate the numerical relationship, or the modifications introduced to the Parshall flume. Based on what was discussed in this review article, the following points are highlighted below.

The application of numerical modeling is considered to be a reliable technique to provide fast and accurate results with minimum cost in terms of time and money.

The efficiencies of various Computational Fluid Dynamic (CFD) software programs have been well described by different scholars who demonstrated the accuracy of results of their numerical models. The reliability of these models made their application popular among researchers and engineers who have access to suitable computer processors. The freedom to alter, as needed, the geometry of the modeled hydraulic structure adds to the popularity of numerical modeling.

Laboratory tests are useful in conjunction with the results of the numerical models, as the accuracy of the CFD models' output can be determined via the data obtained physically on the same setup.

It is important to calibrate the mathematical relationship that was used for the Parshall flume to provide the flowrate since the entrance condition and upstream flow type directly affect the precision of the height–discharge relationship. Nevertheless, choosing inappropriate equations and constants with respect to the type of flow and hydraulic jump, whether it is submerged or not, can trigger inaccurate flowrate results.

Due to the accessibility of testing facilities to the majority of engineers and researchers, most of the time, building and testing methods for small scale models are not as expensive as for large projects. However, for larger projects, numerical models are typically less expensive than physical models. Additionally, the application of hydraulic structures, i.e., large scale Parshall flumes, requires the consideration of different scenarios to assess the tolerance of the structure under unforeseen harsh conditions. For example, choosing a Parshall flume as a measuring device for a wide-open channel requires extensive study on the hydrology of the region to understand the extreme weather conditions over the life span of the structure. The return period should be selected based on the codes and regulations that are available in various versions from different municipalities.

Since having access to high performance processors is essential to run numerical models, in some articles, it was highlighted that to tackle the deficit of limited access to proper computer hardware, the proposed structures were usually designed with a symmetrical shape. Therefore, only one side of the symmetrical structure was modeled to deal with the limited computational resources. Although this method provides reasonable results, the reliability of this technique requires greater validation, particularly for LES and DES simulations, since the behavior of the fluid in motion is highly turbulent.

Based on the review of numerous articles, for further study, the use of CFD models is recommended to perform numerical modeling on various sizes of Parshall flumes since there is a gap in the current state of application of the existing numerical modeling for this type of flume. A large number of turbulence models exist that have not yet been used to simulate the flow in Parshall flumes.

Parshall flume is a flow measuring device that does not require energy to operate. The only vital energy to operate is taken from the water flow. As was explained earlier in this paper, the primary water level at throat section is used to calculate the discharge when there is free flow. The water level in the converging section determines the degree of submergence when submerged flow is experienced. These water level values are directly used to determine the flowrate using the rating equation explained in Section 2.3.2. Using the flow energy to convert the water level into discharge is highly useful in Parshall flumes. Therefore, the authors advocate that such systems are used to retrofit the open channels in agricultural section, wastewater treatment plants, and also encourage different industrial sectors to substitute the current electrical flowmeters with Parshall flumes whenever feasible and applicable.

Chapter 3

Numerical Modeling of Venturi Flume

3.1 Abstract:

In order to measure flow rate in open channels, including irrigation channels, hydraulic structures are used with a relatively high degree of reliance. Venturi flumes are among the most common and efficient type, and they can measure discharge using only the water level at a specific point within the converging section and an empirical discharge relationship. There have been a limited number of attempts to simulate a venturi flume using computational fluid dynamics (CFD) tools to improve the accuracy of the readings and empirical formula. In this study, simulations on different flumes were carried out using a total of seven different models, including the standard $k-\varepsilon$, RNG $k-\varepsilon$, realizable $k-\varepsilon$, $k-\omega$, and $k-\omega\, SST$ models. Furthermore, large-eddy simulation (LES) and detached eddy simulation (DES) were performed. Comparison of the simulated results with physical test data shows that among the turbulence models, the $k-\varepsilon$ model provides the most accurate results, followed by the dynamic k LES model when compared to the physical experimental data. The overall margin of error was around 2-3 %, meaning that the simulation model can be reliably used to estimate the discharge in the channel. In different cross-sections within the flume, the $k-\varepsilon$ model provides the lowest percentage of error, i.e., 1.93 %. This shows that the water surface data are well calculated by the model, as the water surface profiles also follow the same vertical curvilinear path as the experimental data.

3.2 Introduction

The Parshall flume is a simple static measuring device with no moving parts that is used to determine the flow rate in an open channel where a constant recording of discharge is required. The initial idea by Ralph Parshall in designing the Parshall flume was to make it easier for water users, like farmers, who do not have access to sophisticated types of equipment, to be able to determine how much water is delivered to them with an acceptable level of accuracy [58]. Currently, Parshall flumes are mainly used in irrigation and sewer systems to measure the flowrate [43]. In general, they are designed to generate a critical flow within the throat section, which affects the water level along the converging section upstream, implementing an empirical relationship

between water surface elevation and discharge results in finding the discharge value at a specific time from the water surface elevation.

Variations of Parshall flumes are typically restricted to the dimensions of the geometries proposed by Ralph Parshall in 1936 for limited size numbers, i.e., 16 sizes, which vary in the opening from 1” to 144”. The arbitrary dimensions of the flumes used in various open channels in recent years have not been comprehensively studied. Since then, technology has advanced significantly, especially in the development of computational tools. Numerical simulations have introduced a new revolutionary chapter to the design of hydraulic structures, allowing engineers to extend their full potential by designing a variety of different hydraulic structures with new arrangements in their dimensions and shapes. They allow designers to optimize the specifications of their design to suit the need of the project’s objective. Computers and modeling software offer possibilities to perform extensive calculations, and they allow new designs to be tested with relatively low cost. For instance, a proposed hydraulic structure can be simulated to study its behavior under working conditions. This provides engineers with extensive variations in geometries and dimensions when designing a structure. Using computer models makes it possible to implement Parshall flumes with complex shapes and dimensional limitations where needed.

The authors of [46] used a numerical model to develop an alternative rating equation to be implemented at low discharge for different flume sizes. In a study on a submerged Montana flume, to prove the reliability of the CFD programs’ accuracy, the flow rate was calculated with FLOW-3D. It is shown that the numerical results closely matched the experimental results. Furthermore, it is revealed that a free-flow equation for a Parshall flume would also be a good fit for a Montana flume [7]. To determine the accuracy of a field-scaled Parshall flume at a wastewater system in Minneapolis, Minnesota, [42] implemented the large-eddy simulation (LES) and level-set method to compute the turbulent flow under two-phase flow conditions. A three-dimensional finite difference code, SOLA-FLUMP, is presented by [1] to assess the various effects due to the sloped channel, the upstream velocity profile distortion, and the geometry of the flume.

A parametric study was performed in terms of stability and accuracy on Reynolds-average Navier–Stokes (RANS) and hybrid RANS/LES turbulence models and numerical schemes offered in openFOAM, an open-source software, by [59]. From the results, the second-order upwind scheme and limiters were found to be the most stable with the lowest computational cost, thereby providing the highest level of accuracy for RANS models.

It is important to determine the degree of reliability of the model that is going to be used for a specific simulation. One of the most dependable approaches is to evaluate the simulated results with actual experimental data. In this paper, different simulated datasets generated from seven dissimilar methods, i.e., standard $k-\varepsilon$, RNG $k-\varepsilon$, realizable $k-\varepsilon$, and $k-\omega$ SST; Large Eddy Simulation (LES); and Detached Eddy Simulation (DES) are examined versus four physical datasets obtained from physical experiments on different flumes with different discharges.

A high-order partial differential equation, like the momentum transport equation, that includes nonlinear terms cannot be solved analytically to obtain a general solution. Numerical solutions require discretization techniques to reshape the continuous partial differential equation into a discrete equation. Computational fluid dynamics (CFD) using the finite volume method (FVM) [60] can be very useful for this purpose. With the rapid increase in the computational capability of computers, large-eddy simulation (LES) is increasingly embedded in the CFD models used by researchers and engineers to solve turbulent flows [61]. LES is a compromise between the efficiency of Reynolds-average Navier–Stokes (RANS) and the prohibitive computational cost of direct numerical simulation (DNS). Approaches of LES or the variant hybrid family like RANS/LES (DES) are progressively taking over the computationally expensive DNS approach to solve problems with compound geometries and flow properties [62].

The authors of [4] tried to introduce a correction coefficient to a 24” Parshall flume where the positions of the staff gauges were mislocated and the condition of the flume entrance was set up differently from the one introduced by [58]. They used numerical modeling to implement the correction factor for other sizes of Parshall flumes. Based on this study, a part of the small deviations, the physical model, and numerical simulation were aligned with one another.

In order to decrease the head loss in a curved flume, three flumes were studied on the basis of critical flow by [2]. The study was conducted on laboratory experimental results versus numerical simulation data. The hydraulic parameters such as velocity of the free surface and the depth of water were analyzed and compared. A maximum error of 4.7% in the water depth was obtained. It was shown that a good consistency was achieved between numerical simulation and experimental data.

The objective of this paper is to solve the Navier–Stokes equations using OpenFOAM to study the behavior of various numerical models in simulating Parshall flumes similar in size and flowrate to the flumes used in physical experiments by Dursun (2016).

Based on the literature review at the beginning, there is no comprehensive numerical solution that has been conducted on the models simulating the hydraulic structures, i.e., Parshall flume. The reliability of RANS LES and DES turbulence models in simulations has been studied in this research by evaluating the performance of seven turbulence models against the experimental data of different Parshall flume structures. Subsequently, the consistency of the simulations was determined in various scenarios in relation to the experimental data. Based on what was discussed in the literature review, seven turbulence models, i.e., RANS models (including Standard $k-\varepsilon$, RNG $k-\varepsilon$, Realizable $k-\varepsilon$, and $k-\omega\, SST$) and hybrid RANS/LES models such as $k-\omega\, SST-DES$, and an LES models, namely, the Smagorinsky method and dynamic K LES method, respectively, were selected due to their wide usage and advantages compared to other turbulence models.

This paper is organized as follows: the methodology is explained in the next section, including governing equations, turbulence models (including RANS, LES, and DES models), numerical setup (including initial and boundary conditions), mesh analysis, and data; the results and discussion are then presented, in which the performance of numerical models is discussed. Some concluding remarks complete the study.

3.3 Methodology

By the increasing power of processors, computational fluid dynamics (CFD) has become the most convenient tool to simulate fluid motion. In CFD, the fluid's flow establishment follows physical parameters, including pressure, viscosity, velocity, and temperature. In order to simulate a physical case related to the fluid flow, the physical properties should be taken into account accurately.

CFD approaches are used in solving the fluid flow equations as well as fluid interaction with solid bodies. The Euler equation for inviscid fluid and the Navier–Stokes equation for viscous fluid can be derived in their integral arrangement with respect to the conservation of energy, mass, and momentum [63].

OpenFOAM is one of the open-source solvers for CFD that is widely used for simulations. It is a platform including numerous C++ libraries and applications that are able to solve numerically the continuum mechanics problems [64]. It uses a tensorial method that implements an object-oriented programing approach and employs the finite volume Method (FVM).

3.3.1 Governing Equations

A viscous incompressible fluid flow is governed by a general three-dimensional system of equations, called the Navier–Stokes system, that consists of momentum and continuity equations. The system is described as follows [41,40]:

$$\frac{\partial u}{\partial x}+\frac{\partial v}{\partial y}+\frac{\partial w}{\partial z}=0 \tag{11}$$

$$\frac{\partial u}{\partial t}+u\frac{\partial u}{\partial x}+v\frac{\partial u}{\partial y}+w\frac{\partial u}{\partial z}=-\frac{1}{\rho}\frac{\partial p}{\partial x}+\nu\nabla^2 u \tag{12}$$

$$\frac{\partial v}{\partial t}+u\frac{\partial v}{\partial x}+v\frac{\partial v}{\partial y}+w\frac{\partial v}{\partial z}=-\frac{1}{\rho}\frac{\partial p}{\partial y}+\nu\nabla^2 v \tag{13}$$

$$\frac{\partial w}{\partial t}+u\frac{\partial w}{\partial x}+v\frac{\partial w}{\partial y}+w\frac{\partial w}{\partial z}=-\frac{1}{\rho}\frac{\partial p}{\partial z}+\nu\nabla^2 w-g \tag{14}$$

where ρ denotes density; p represents total pressure; u, v, and w represent the velocity in three different directions, i.e., x, y, and z; t is used for time; and gravitational acceleration is denoted by g. ρ is obtained using the following equation:

$$\rho=\alpha\rho_1+(1-\alpha)\rho_2 \tag{15}$$

Here, ρ1 and ρ2 represent the air and water densities, the two phases of the involved fluid. The α value varies from 1 to 0 depending on the location, where 1 denotes the presence of water and 0 shows the presence of air. Any number between these two values represent the interface.
Finally,

$$\nabla^2=\frac{\partial^2}{\partial x^2}+\frac{\partial^2}{\partial y^2}+\frac{\partial^2}{\partial z^2} \tag{16}$$

3.3.1.1 Equation of the Free Surface

With respect to the zero pressure at the surface, the free surface was analyzed with the volume-of-fluid (VoF) method. The following equation is used by VoF:

$$\frac{\partial \alpha}{\partial t}+\frac{\partial(\alpha u)}{x}+\frac{\partial(\alpha v)}{y}+\frac{\partial(\alpha w)}{z}=0 \tag{17}$$

As stated earlier in this paper, a powerful open-source CFD, i.e., OpenFOAM application, was used for the purpose of the numerical simulations.

The flow motion in a Parshall flume was simulated in this study with the help of seven different turbulence models: Standard $k-\varepsilon$, Realizable $k-\varepsilon$, and $RNG\ k-\varepsilon$ models; $k-\omega\ SST$ models; and Detached Eddy Simulation (DES) models, such as $k-\omega\ SST-DES$; as well as LES methods, including the Smagorinsky LES model and dynamic K LES model. In the following, a brief description of each selected model is provided.

3.3.1.2 Reynolds-Average Navier–Stokes (RANS) Approach

The Reynolds-average Navier–Stokes Model is currently the most popular approach for the simulation of fluid flow. This approach essentially uses a viscosity term to approximate the turbulence equations. K is a term in these models that represents the fluctuations of the turbulence kinetic energy per unit mass.

3.3.1.2.1 Standard $k-\varepsilon$ model

This model requires two additional transport equations: one for turbulent kinetic energy (k) and another for energy dissipation (ε). Apart from its poor performance in large adverse pressure gradient cases, it is known as one of the most popular turbulence models [65]. This model comes from the Reynolds-averaged Navier–Stokes (RANS) category where modeling is applied to all properties of fluid motion.

The equation for turbulent kinetic energy k and dissipation ε is shown below:

$$\frac{\partial(\rho k)}{\partial t}+\frac{\partial(\rho k u_i)}{\partial x_i}=\frac{\partial}{\partial x_j}\left[\frac{\mu_t}{\sigma k}\frac{\partial k}{\partial x_j}\right]+2\mu_t E_{ij}.E_{ij}-\rho\varepsilon \qquad (18)$$

$$\frac{\partial(\rho\varepsilon)}{\partial t}+\frac{\partial(\rho\varepsilon u_i)}{\partial x_i}=\frac{\partial}{\partial x_j}\left[\frac{\mu_t}{\sigma\varepsilon}\frac{\partial\varepsilon}{\partial x_j}\right]+C_{1\varepsilon}\frac{\varepsilon}{k}\,2\mu_t E_{ij}.E_{ij}-C_{2\varepsilon}\rho\frac{\varepsilon^2}{k} \qquad (19)$$

ε is the component that controls the turbulence scale where k represents the turbulence kinetic energy. The reader is referred to [41] for further details and values of the coefficients.

3.3.1.2.2 Realizable $k-\varepsilon$ model

The latest improved form of the three $k-\varepsilon$ models is the realizable $k-\varepsilon$ model [66,67]. There are two significant differences when this model is compared to the standard k-epsilon model.

Firstly, formulation of the turbulence viscosity has been revised. Secondly, the dissipation rate transport equation is explained based on the equation of transport of the mean-square vorticity [67,68].

$$\frac{\partial}{\partial t}(\rho k) + \frac{\partial}{\partial x_j}(\rho k u_j) = \frac{\partial}{\partial x_j}\left[\left(\mu + \frac{\mu_t}{\sigma_k}\right)\frac{\partial k}{\partial x_j}\right] + G_k + G_b - \rho\varepsilon - Y_M + S_K \qquad (20)$$

$$\frac{\partial}{\partial t}(\rho\varepsilon) + \frac{\partial}{\partial x_j}(\rho\varepsilon u_j) = \frac{\partial}{\partial x_j}\left[\left(\mu + \frac{\mu_t}{\sigma_\varepsilon}\right)\frac{\partial \varepsilon}{\partial x_j}\right] + \rho C_1 S\varepsilon - \rho C_2 \frac{\varepsilon^2}{k + \sqrt{\nu\varepsilon}} + C_{1\varepsilon}\frac{\varepsilon}{k}C_{3\varepsilon}G_b + S_\varepsilon \qquad (21)$$

The reader is referred to [69] for further details and value of the coefficients.

3.3.1.3 LES Approach

3.3.1.3.1 Smagorinsky LES Model

This model was originally developed within the metrological community to simulate atmospheric air currents [70]. As a well-known subgrid-scale model according to [71], the Smagorinsky model estimates the shear as

$$\nu_t^{Smag} = \left(C_{Smag}\Delta\right)^2 |\bar{S}| \qquad (22)$$

$$\overline{S_{ij}} = \frac{1}{2}\left(\frac{\partial \overline{u_i}}{\partial x_i} + \frac{\partial \overline{u_j}}{\partial x_j}\right) \qquad (23)$$

where

$$|\bar{S}| = \sqrt{2\overline{S_{ij}S_{ij}}} \qquad (24)$$

The reader is referred to [70] for further details and values of the coefficients.

One of the main disadvantages of this model is the lack of ability to predict the energy transfer from subgrid-scale structures to the greater resolved scales; thus, the model is totally dissipative. Another problem with the Smagorinsky model is that its coefficient has to be adjusted for every flow field. However, it is still one of the well-known models in the field of CFD. The Smagorinsky

model is easy to use in numerical simulations. If the Smagorinsky coefficient is adjusted based on the local characteristics of the fluid motion, it can generate more accurate results [71].

3.3.1.3.2 The Dynamic One-Equation Model

The SGS stresses determine how successful an LES model can be. As a simple model, in the Smagorinsky model, the factor of the proportionality is a fixed value that has to be determined before running the model. In reality, the factor is a flow-dependent value and is not defined as a single universal constant. The weak point of the model comes from this section. There have been attempts to improve this model [72,73]. Moreover, this model is completely dissipative, and there is always a transformation of large-to-small scale for the energy.

On the other hand, dynamic models are the best choice to substitute the Smagorinsky model. In this model, the C value of the subgrid eddy viscosity is determined while the simulation is computed [74]. In recent decades, a one-equation dynamic model has been presented [75]. The equation of the dynamic model is presented below.

$$\frac{D}{Dt}(\rho k) = \nabla.(\rho D_k \nabla_k) + \rho G - \frac{2}{3}\rho k \nabla.u - \frac{C_e \rho k^{1.5}}{\Delta} + s_k \qquad (25)$$

where the C_e and S_k coefficients are derived from local flow properties [69]. The reader is referred to [76] for further details.

3.3.1.4 DES Approach

3.3.1.4.1 $k-\omega\ SST-DES$

While the RANS model is derived through Reynolds temporal averaging, the LES model is the result of spatial filtering. Between these two methods, the difference is the magnitude of the generated eddy viscosity. This is one of the main reasons for the development of the DES model, which has the ability to cover the weaknesses of LES when it comes to treating wall regions with very fine mesh [77].

The RANS approach is used in the near-wall region by the DES method where, at the same time, the LES model is applied to the rest of the region excluding the wall region. The region associated with the LES model is usually the core turbulent area, where large-scale turbulences play a major role. Within this area, the DES approach uses a LES subgrid-scale model, while for the near-wall region, it uses the RANS model [78].

A DES-improved form of the k-ω SST method is the k-ω SST DES approach [79,80]. Recently, in the aerodynamic field, DES has been widely implemented due to its computational speed and quality of results. It is proven to be less computationally expensive, and it generates better results than steady RANS [81,82].

The turbulence specific dissipation rate equation is given by

$$\frac{D}{Dt}(\rho\omega) = \nabla.(\rho D_w \nabla\omega) + \rho\gamma\frac{G}{\nu} - \frac{2}{3}\rho\gamma\omega(\nabla.u) - \rho\beta\omega^2 - \rho(F_1 - 1)CD_{k\omega} + S_\omega \quad (26)$$

and the turbulence kinetic energy is calculated as

$$\frac{D}{Dt}(\rho k) = \nabla.(\rho D_k \nabla k) + min(\rho G, (c_1\beta^*)\rho k\omega) - \frac{2}{3}\rho k(\nabla.u) - \rho\frac{k^{1.5}}{\bar{d}} + s_k \quad (27)$$

the length scale, $\bar{d}$, is given by

$$\boldsymbol{min}\ (C_{DES}\Delta, \frac{\sqrt{k}}{\beta^*\omega}) \quad (28)$$

and the turbulence viscosity is obtained using

$$\nu_t = \alpha_1 \frac{k}{max(\alpha_1\omega, b_1F_{23}S)} \quad (29)$$

The reader is referred to [83] for further details and value of the coefficients.

3.3.2 Numerical Setup

3.3.2.1 Numerical Solution Details

The combination of the finite volume method with the VoF method was used in the model. To solve the governing equation of motion, the "interFoam" solver was implemented in OpenFOAM. The temporal term was discretized with the help of a Eulerian scheme, excluding besides the Gauss linear method, which is used for the gradient term. For the Laplacian, the corrected Gauss linear method was applied. The divergence terms were discretized using a Gauss vanLeer plus Gauss linear scheme. The linear scheme was used to discretize the interpolation term.

The tolerance level was defined for each individual variable, while the desired convergence was expected to be achieved where an iterative solver was used in the processing. The Gauss–Seidel

technique was applied with a level of accuracy of 10^{-5} for the fraction of liquid (α), 10^{-8} for pressure, and 10^{-8} for the velocity.

3.3.2.2 Initial Conditions

The flume had a fixed inlet flow velocity for each case, i.e., a discharge of 20 l/s or 30 l/s as the initial conditions. There was no initial acceleration or dissipation defined in the model. There was no flow across the walls, i.e., there was no liquid coming in or getting out through the wall boundaries at the defined locations. Initial water surface was set to be constant everywhere.

3.3.2.3 Boundary Conditions

There were different boundary conditions employed in this simulation as illustrated in Figure 20. Hydraulically smooth walls were considered in this study, and standard wall functions were employed. Water discharge was specified at the inlet. Zero gradient condition was considered at the outlet. The free surface was tracked based on the volume-of- fluid method based on a zero-pressure condition at the interface of air and water. Figure 20 below shows the boundary segments from the side view and top view of the simulated Parshall flume.

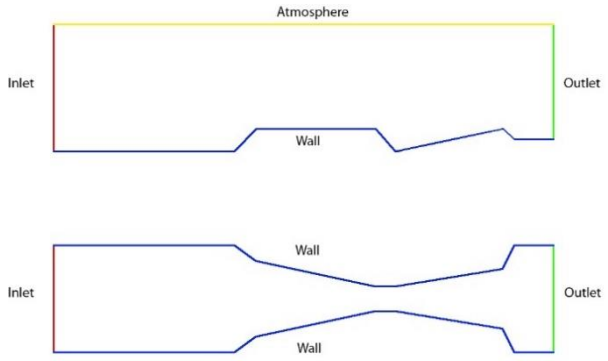

Figure 20: Side view and top view of the boundary condition of the modeled Parshall flume.

3.3.2.4 Mesh Analysis

In this study, in order to determine the optimum size of the mesh, mesh sensitivity analysis was conducted. The mesh grid used in this paper is a structured mesh. The purpose of this analysis is to find the finest mesh size for which the results will not be affected further.

Figure 21 shows the mesh sensitivity analysis performed on the Parshall flume. The maximum cell number was 263,700 cells for this structure. The optimal case in terms of computational cost and

changes in results is that illustrated in Figure 21b, with a total of 74,496 cells. Greater reduction applied on the cell size did not significantly change the numerical results.

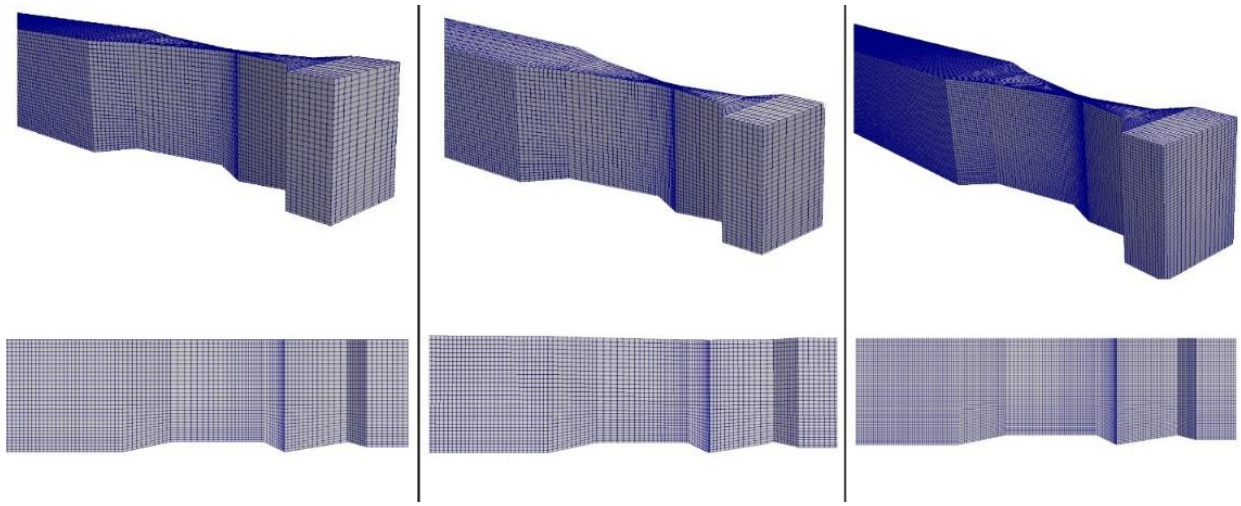

(a) (b) (c)

Figure 21: Mesh convergence analysis. Side view and 3D views of the Parshall flume mesh: (a) the mesh with a total of 52,200 cells; (b) the mesh with a total of 74,496 cells; (c) the mesh grid with a total of 263,700 cells.

In Figure 22, the results of the mesh sensitivity analysis are provided for the cross-sections 4–6. As the size of the original coarse mesh became finer, the simulated water levels approached the values of the experimental data. In this study, the initial number of cells was 52,200, and it was gradually increased to 74,496 and further to 263,700 cells. The results from the last two finer meshes show negligible difference; hence, the mesh containing 74,496 cells was selected and further used to implement the remaining turbulence models.

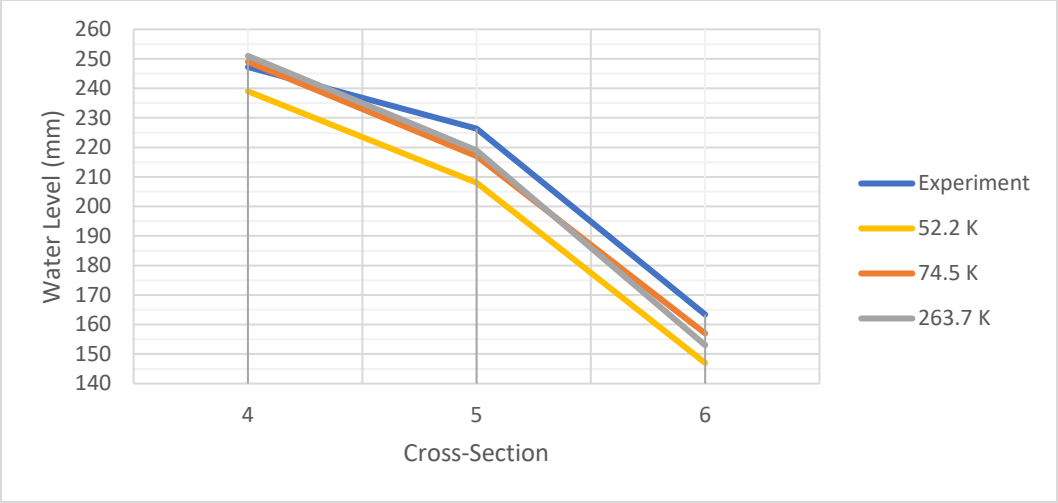

Figure 22: Mesh analysis graphs for the cross-section 4, 5, and 6.

3.3.2.5 Data

The experimental tests were conducted in the hydraulic laboratory of Firat University, Elazig, Turkey (Dursun, 2016). The tests were performed in a rectangular channel with the dimensions of 0.4 by 5 by 0.6 m in width, length, and depth, respectively. The purpose of these experiments was to determine the changes in the quantity of the dissolved oxygen of the stream before and after a Parshall flume structure was introduced. The dimensions of the Parshall flumes that was used in this research were the same as the 3-inch (7.62 cm) Parshall flume with a 45 degree wing wall. The discharge in the experiment was measured using an electromagnetic flow meter.

The model was run for 300 time-steps where, after 120 steps, water levels became steady; water surface fluctuations, for instance, were limited to +/-0.003m. The water level is shown using a post-data analysis software called ParaView. At the point of interest, two vertical planes (perpendicular to each other) were introduced, where the intersection line between the two planes was set to pass the desired point. The Y-coordinate (water level) of the line was extracted using the calculator filter; for example, the water level at each desired time step is shown afterwards in the tabulated mode in a separate window in ParaView.

3.4 Results

The numerical simulation for the experimental case conducted by [43] is performed in this study. The Parshall flume used in this study is a 3-inch Parshall flume modified to meet the experimental

criteria. OpenFOAM was used as an open source CFD tool to carry out the numerical simulation of the Parshall flumes.

Switching from a coarse size mesh grid to a finer grid size in the mesh sensitivity analysis led to some change seen in the numerical simulation model results. As the flow rate decreased from 30 to 10 l/s, the model tended to produce better results. This pattern is observed in the $k-\varepsilon$ model as well as the other RANS models.

Water surface elevations in seven cross-sections were compared with the experimental results with three different flowrate values, i.e., 10, 20, and 30 l/s. Figure 23 shows water surface elevation for the flowrate of 10 l/s using seven various models. As shown in Figure 23, all models follow the same pattern as the experimental data. Figures 24 and 25 are introduced to show more clarified view of the water level data. Based on the results of various turbulence models used in simulations, the $k-\varepsilon$ turbulence model provides the most accurate simulation compared to the other models used in this study.

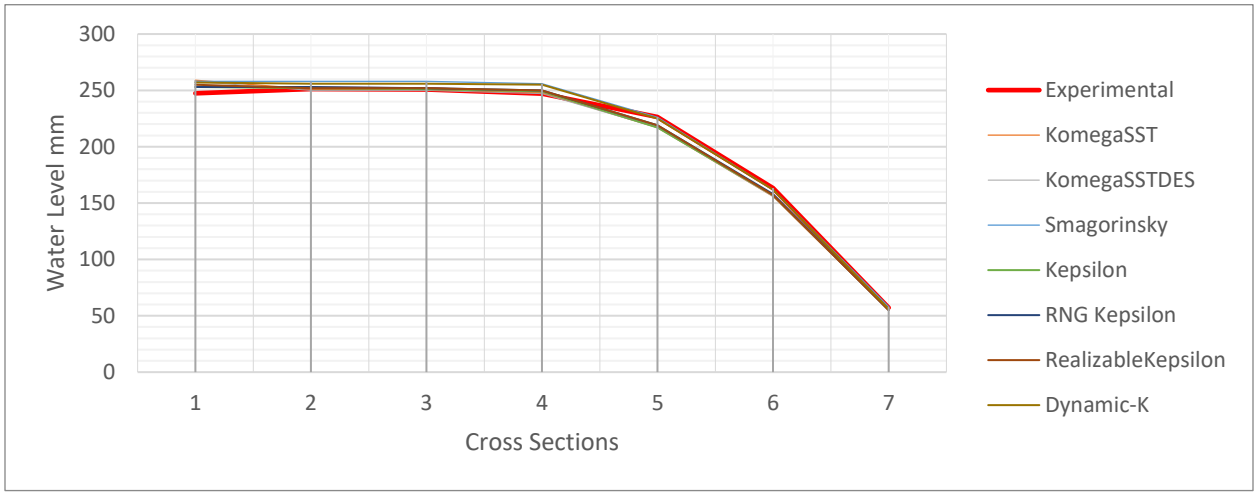

Figure 23: Comparison of experimental water level results (obtained with the average measuring error of 1.93–2.58 %) with the numerical simulation results for the discharge of 10 l/s.

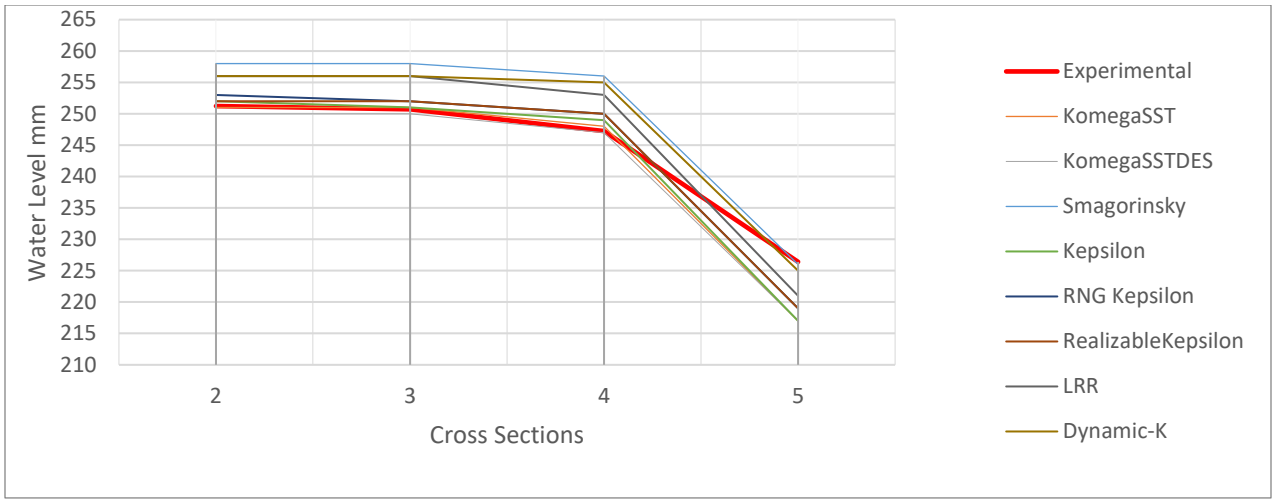

Figure 24: Comparison of experimental water level results (obtained with the average measuring error of 1.93–2.58 %) with the numerical simulation results for the discharge of 10 l/s (for cross-sections 2, 3, 4, and 5).

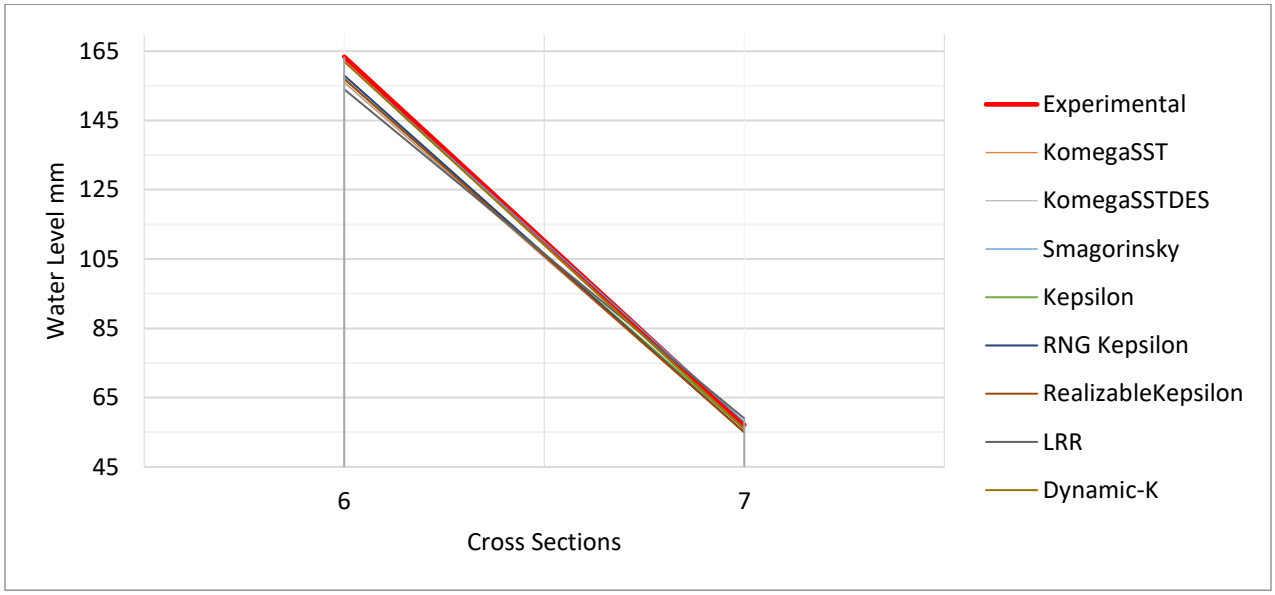

Figure 25: Comparison of experimental water level results (obtained with the average measuring error of 1.93–2.58%) with the numerical simulation results for the discharge of 10 l/s (for cross-sections 6 and 7).

The locations of the cross-sections in the Parshall flume are denoted in Figure 26 where at all critical locations, a cross-section is introduced. The reason for choosing the cross-section locations,

as shown in Figure 26, is that in the laboratory experiment conducted by Dursun in 2016, the same locations were chosen; hence, water level data were also available for them.

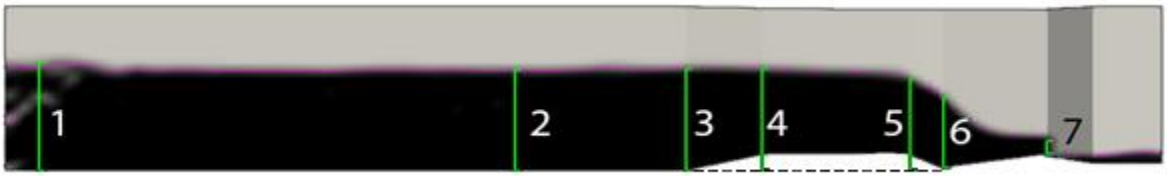

Figure 26: Location of cross-sections of Parshall flume.

In Figure 27, the fluid flow in the Parshall flume with a flowrate of 10 l/s is illustrated. As the stream lines indicate, the velocity of the fluid prior to the flume throat displays a maximum of 1 m/s, and by the time it reaches the narrow section with a declining floor, the speed rapidly increases by 50%. This is the section where the fluid experiences supercritical flow. It continues to increase by the end of the divergence section where maximum velocity is reached (red arrows), i.e., 2 to 2.5 m/s. Once the fluid reaches the inclined slope in the divergence section downstream, the flume forces it to develop a hydraulic jump.

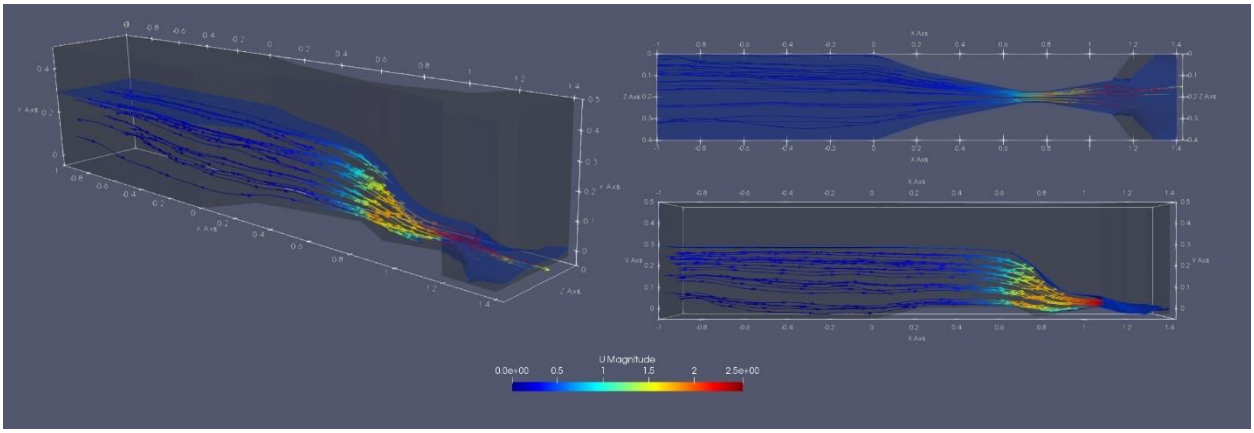

Figure 27: 3D, top, and side views of the Parshall flume.

The velocity profiles of all seven turbulence models at cross-section 5, where the numerical models exhibited the maximum velocity, are shown in Figure 28. The comparison between different velocity profile shows that in the seven different turbulence models, the values are almost identical, with a difference margin of 0.04 m/s at the maximum velocity points. The maximum recorded

velocity in the flume for different models is within the range of 1.26–1.28 m/s in the different models. The “y” axis is the local coordinate of the flume throat defined in the OpenFOAM computational domain.

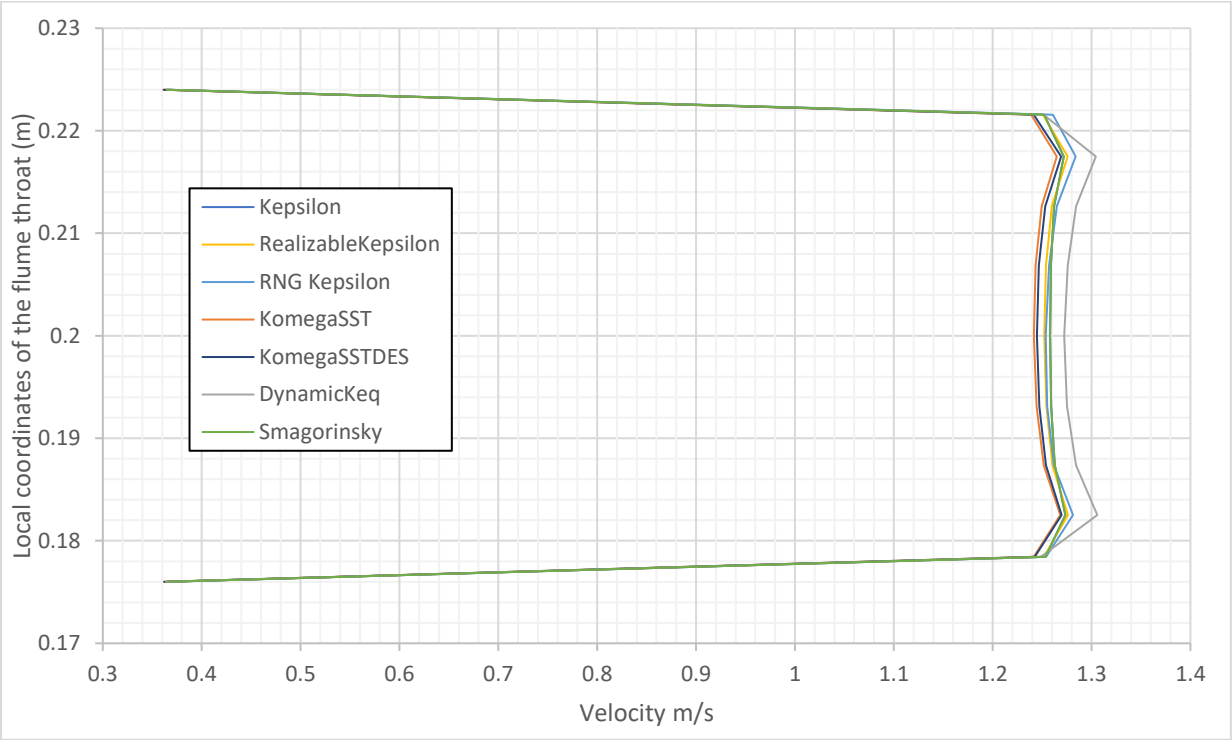

Figure 28: Comparison of the velocity profile at cross-section 5 and the results obtained using the investigated turbulence models.

As illustrated in Figure 29, the velocity is constant upstream of the midsection of the converging area. At the end of this section, the flow is forced to increase its velocity due to the narrow design of the throat combined with a sharply slopped bed. The velocity streamlines after the throat section of the flume show that the velocity magnitude is greater than that observed throughout the rest of the structure. Once the flow immediately exits the divergence section, it attains maximum velocity.

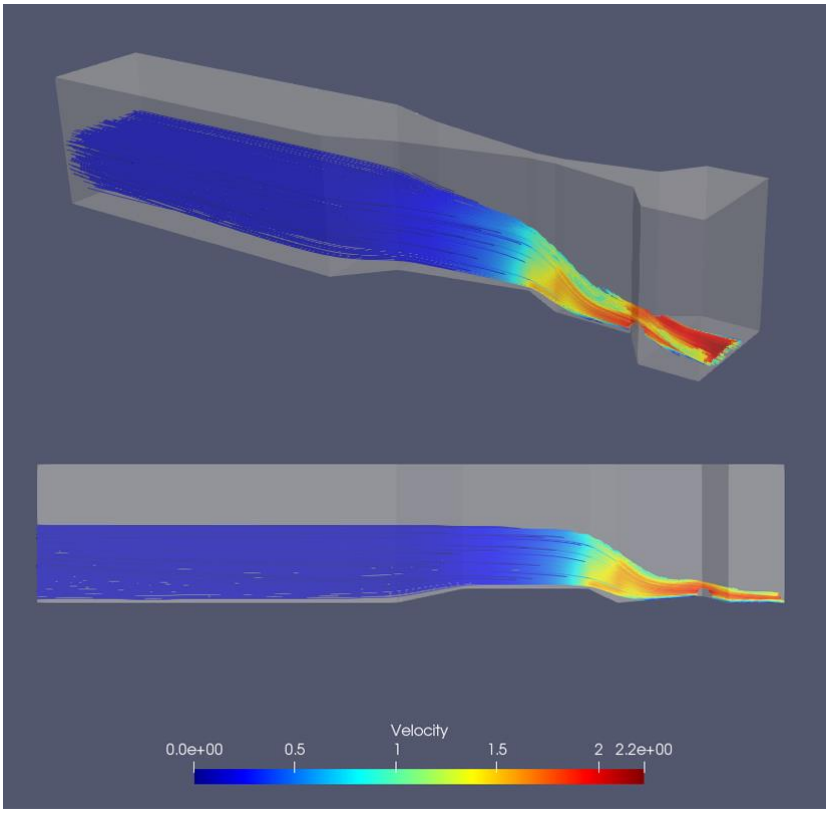

Figure 29: 3D and side view of the velocity field of the flume with a flowrate of 10 l/s.

The flume's pressure field is represented in Figure 30. In the section between cross-sections 5 and 6, the pressure is negative. As illustrated in this figure, due to the throat section, the pressure is built up in the upstream, while when passing section 5 toward downstream, the value of the pressure drops rapidly.

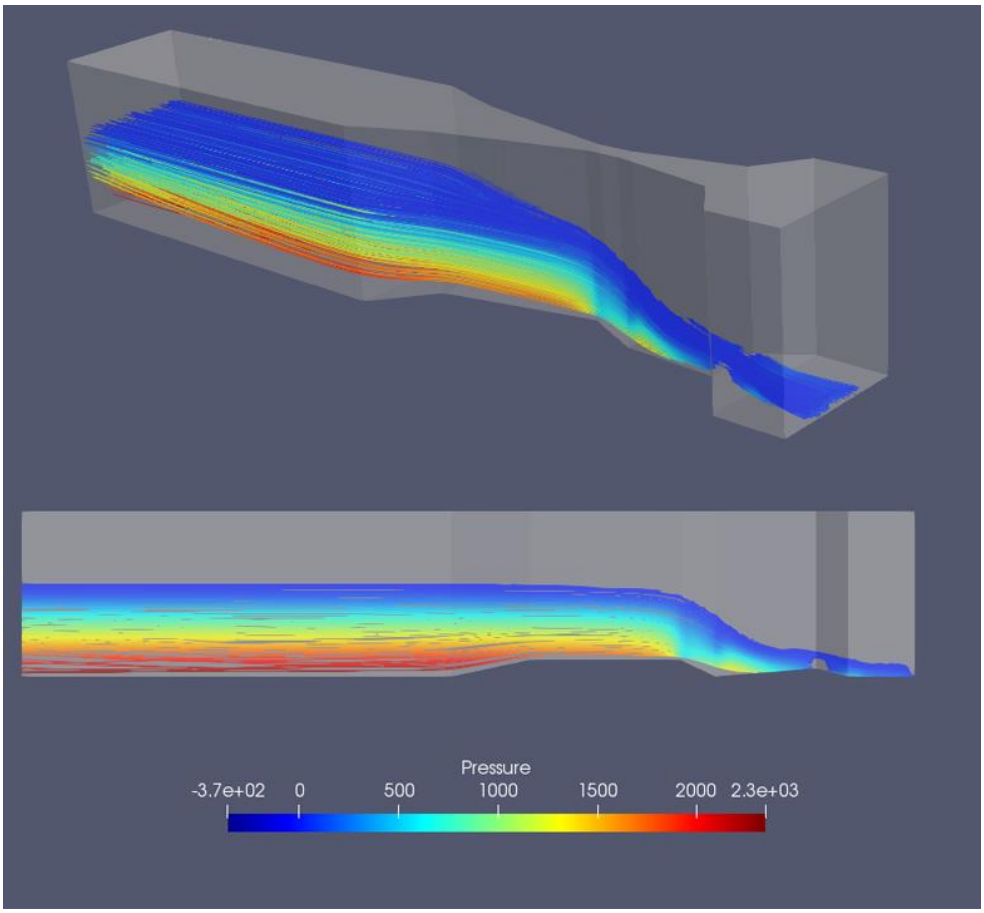

Figure 30: 3D and side view of the pressure field in the flume with a flowrate of 10 l/s.

3.5 Discussion

The percentage difference of water level values of the numerical models and the experimental data is specified in Table 3 below. The calculation is performed based on the following relationships [41]:

$$Error = \frac{|H_{exp} - H_{sim}|}{H_{exp}} \times 100 \quad (30)$$

$$RMSE = \sqrt{\frac{\Sigma^{(h_{exp}-h_{sim})^2}}{n}} \quad (31)$$

$$R^2 = \frac{\sum(\hat{y} - \bar{y})^2}{\sum(y - \bar{y})^2} \quad (32)$$

$$CRMSE = \sqrt{\frac{\sum_{i=1}^{n}\left((X_i^{calc} - X_{mean}^{calc}) - (X_i^{expr} - X_{mean}^{expr})\right)^2}{n}} \qquad (33)$$

Here, the root mean square error (RMSE), centered root mean square error (CRMSE), and correlation coefficient (R) are used in order to compare the simulation results with experimental data. The results from the above formulas are presented in Table 3, where different types of error analysis are applied in order to determine the reliability of the numerical simulations.

Table 3: The error percentage, root mean square error (RMSE), standard error, R^2 , and centered root mean square error (CRMSE) of the simulated data vs. experimental data.

	Error percentage							Avrg. Err %	RMSE	Stndr err	R^2	CRMSE
Cross-Sections	1	2	3	4	5	6	7					
K epsilon	2.30%	0.31%	0.11%	0.71%	4.16%	3.91%	2.03%	1.93%	0.49%	0.23%	0.996	0.47%
RNG K epsilon	2.30%	0.70%	0.51%	1.12%	3.27%	3.30%	3.78%	2.14%	0.44%	0.18%	0.997	0.43%
Realizable K epsilon	3.11%	0.31%	0.51%	1.12%	3.27%	3.91%	3.78%	2.29%	0.49%	0.00%	0.996	0.49%
K omega SST	4.73%	0.09%	0.11%	0.31%	4.16%	4.52%	3.78%	2.53%	0.64%	0.08%	0.993	0.63%
K omega SST DES	4.33%	0.49%	0.29%	0.10%	4.16%	4.52%	3.78%	2.52%	0.61%	0.14%	0.993	0.60%
Dynamic-K	3.92%	1.90%	2.10%	3.14%	0.62%	0.85%	2.03%	2.08%	0.55%	0.09%	0.998	0.43%
Smagorinsky	4.33%	2.69%	2.90%	3.54%	0.18%	0.85%	1.47%	2.28%	0.65%	0.08%	0.998	0.45%

Among the seven different turbulence models applied in this study, the Smagorinsky and dynamic K equation models provide the least average error values. This model provides the minimum error percentages not only in the average value of all of the cross-sections but also within the first three, i.e., 1, 2, and 3.

By calculating the root mean square error for all the turbulence models, the results show that two models, $k - \varepsilon$ and dynamic K LES, provide the lowest values, 1.93% and 2.08%, respectively, while the $k - \omega\ SST$ model has a greater value compared to the others. However, for comparison

of the R^2 values of this turbulence model, the Smagorinsky and dynamic K LES models have the closest value to 1, i.e., 0.998.

The ranges of the average error percentage for all of the turbulence models are within a narrow domain a minimum value of 1.93 % and a maximum value is 2.53%. While most of the turbulence models used in this study provided reliable error percentages, the $k-\omega\ SST$ model was the only one that generated results with a high average error of 2.53% and RMSE of 0.64%, and the lowest R^2 was also recorded for this model.

Table 3 and Figure 31 tabulate the results of the different numerical simulations at various locations in the flume, i.e., at the seven cross-sections. The average values and the statistical analysis that were discussed earlier in this section are also included here.

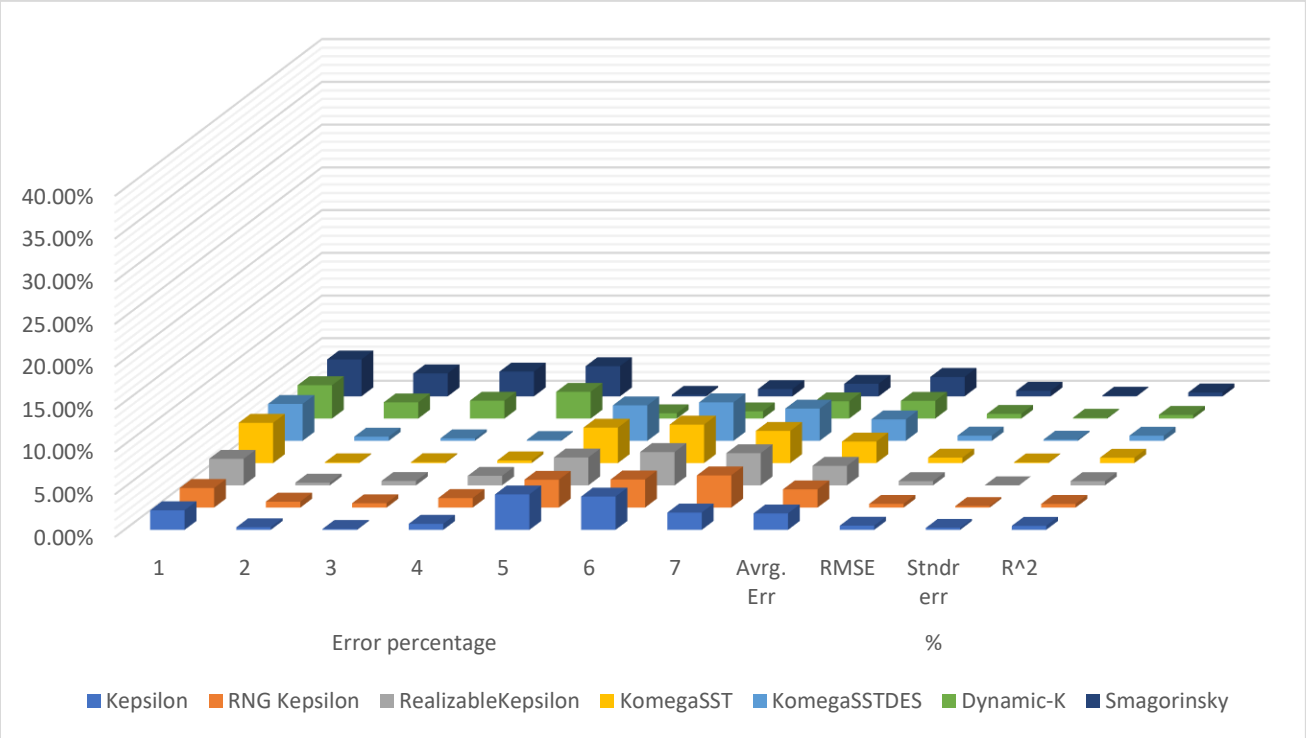

Figure 31: Errors calculated for the model results corresponding to the different turbulence models used.

At cross-section 1, the error percentages for all the models were larger than those calculated at the next cross-section (cross-section 2). Since the location of the first cross-section was chosen very close to the defined inlet of the flume, the unsteady water surface affected the results at this point.

3.5.1 RANS Models:

The best average performance was obtained using the standard k–ε turbulence model. The other turbulence models that fall into this family showed less accuracy than the LES models. However, the difference percentages at sections 2–4 are better than those obtained using the LES and DES models.

3.5.2 DES Model:

The only DES model used in this study, $k-\omega\ SST\ DES$, provided almost the same average result as those obtained using the $k-\omega\ SST$, which has the greatest average error percentage among the models. The second highest average error percentage was observed for the DES family of turbulence models.

3.5.3 LES Model:

Two LES models were used in this study. The water surface elevation results from the Smagorinsky model and dynamic K LES are similar to those of the RANS model family. The average error value, as mentioned earlier, is the lowest for dynamic K LES following the standard $k-\varepsilon$ model.

The pressure and velocity fields for all the models follow same pattern, where the low velocity of the flow is converted to supercritical flow just after entering the throat section of the flume. The pressure field exhibits opposite behavior as the initial high-pressure flow enters the throat of the flume: the pressure drops and reaches a negative value in the throat over a short distance.

At the sections where the velocity is locally maximum, the pressure value drops dramatically. This is due the higher viscous losses occurring with the high velocity flow.

3.6 Conclusions

The main objective of this study was the numerical examination of fluid motion in a Parshall flume. Assessing the results of different turbulence models, such as standard $k-\varepsilon$, realizable $k-\varepsilon$, RNG $k-\varepsilon$, $k-\omega$ SST, $k-\omega$ SST DES, Smagorinsky, and the dynamic K LES. reveals that despite some poor performance of $k-\omega\ SST$ within two cross-sections, the same as the rest of the turbulence models except DES family models, this method estimates the water level accurately enough overall.

This study shows that the results from a turbulence model, in general, a CFD model like OpenFOAM, can provide reliable solutions to Parshall flume design problems. CFD models are able to simulate Parshall flumes to find the optimum design specifications for different scenarios like design changes to increase the efficiency of Parshall flumes. The results are provided with the lowest cost compared to experimental methods.

At the first location chosen to collect data (cross-section 1), the quality of simulated results was not adequate, as discussed in the previous section. To eliminate this issue, the authors recommend conducting further studies on this type of structure.

This study can be further expanded by proposing some slight changes in the design of the Parshall flume, for example, increasing the reliability in terms of the gauge reading of the stilling well at the converging section and also providing more accurate empirical relationships with respect to these changes.

It is recommended as a continuation of this study to conduct a detailed investigation into finding a proper correction factor for the numerical simulated models when different higher flow rates are used. In this study, the simulation data with a 10 l/s flowrate achieved the lowest error value compared to the experimental results, while those with larger flowrates, such as 20 or 30 l/s, where experimental data were available, demonstrated higher error values.

In order to conduct more accurate assessments of numerical model performance, it is recommended that future studies use more sources of experimental data to reduce the impact of experimental data error on the assessment of simulated results.

Chapter 4

Numerical Simulation of Flow in Parshall Flume Using Selected Nonlinear Turbulence Models

4.1 Abstract

This study uses a computational fluid dynamics (CFD) approach to simulate flows in Parshall flumes, which are used to measure flowrates in channels. The numerical results are compared with the experimental data, which show that choosing the right turbulence model, e.g., $v^2 - f$ and LC, is the key element in accurately simulating Parshall flumes. The Standard Error of Estimate (SEE) values were very low, i.e., 0.76% and 1.00%, respectively, for the two models mentioned above. The Parshall flume used for this experiment is a good example of a hydraulic structure for which the design can be more improved by implementing a CFD approach compared with a laboratory (physical) modeling approach, which is often costly and time-consuming.

4.2 Introduction

Data from downscaled physical models of different hydraulic structures, such as dams, weirs, etc., were, in the past, the main resource for predicting the consequences of extreme damage. In recent years, with advancements in computing facilities and numerical modeling methods, numerical simulations have become a powerful and popular approach in the design of hydraulic structures [84].

There are various reasons, such as irrigation and quality control, for the importance of measuring the flowrate in an open channel, and this has led different individuals to come up with various ideas and designs for discharge measurement devices. One of the most popular devices is the Parshall flume, a modification of the Venturi flume, developed by Ralph L. Parshall in the 1930s. The major difference between this flume and the Venturi flume is the drop that was introduced in the throat's bed elevation. This design, with a negative bed slope starting at the beginning of the throat section, helps fluid gain speed and, shortly before exiting the throat, a relatively gentle positive slope reduces the speed of the fluid at the exit of the throat section. The relationship between the head at two locations within the flume, i.e., the throat and upstream, provides a value for the flowrate in the open channel [85].

The available sizes for Parshall flumes are limited, and in addition, within this limited range, manufacturers tend to contravene the original specifications provided by Parshall as the inventor. To create a custom-size Parshall flume, many experiments have to be undertaken by the manufacturers to ensure the accuracy of the flowrate within the device. It is costly and time-consuming to run the necessary laboratory experiments for a new size, and using a Computational Fluid Dynamics (CFD) model can significantly accelerate the process [86].

Computer simulations are an essential tool in the design and optimization of hydraulic structures at present, and recent advancements in computing hardware now also allow researchers and engineers to solve previously impossible equations. Fluid motion is one of the most complicated engineering phenomena, and a particular approach to solving a fluid's governing equations depends on the hardware limitations and available time. Various turbulence models are available within different computational fluid dynamics simulation software, and obtaining the best possible hydraulic structural design is possible through the use of CFD simulations. It is important to choose the best model with respect to the cost of calculations and accuracy. Therefore, in this paper, three nonlinear turbulence models from the RANS family were chosen to simulate the flow of water in a 3-inch Parshall flume, and the data from the simulations are compared with the experimental results from a study conducted by Dursun [43].

The study by Wright et al. [46] on the Parshall flume rating curve revealed that calibration for low-discharge flows for the Parshall flume had not been carried out; therefore, there was a bias in the results provided by Parshall himself for the proposed relationship. In their paper, they tried to provide a solution to this flaw, and so a numerical model was established to address the effect of the viscosity of the fluid on the depth discharge relationship. Experiments on a variety of flumes that carried only 15% of the recommended discharge revealed that the flowrate was overpredicted by 25%. The proposed numerical model for the low discharges provided a good match with the experimental data obtained in the laboratory.

Khosronejad et al. [42] implemented a Large Eddy Simulation (LES) model to determine the accuracy of Parshall flume discharge results in comparison with the experimental data. Their study was conducted on two Parshall flumes that were placed in a parallel arrangement, and the results were taken either from the flow passing through an individual flume when the other flume was closed or with the flow passing through both flumes at the same time. In addition to the flow measurement device used in this experiment, a dye dilution approach was also implemented to

determine flow rates in the field. The difference between the standard rating curve value and the modeled value according to their study was, at maximum, 10%, while the discharge was at the lower flow rate for all three different scenarios, i.e., flows passing through flumes individually or in parallel, and was a minimum of 1.3% when the discharge was between 1.13 and 1.7 m^3/s in the parallel flow case. It was concluded that a Parshall flume could provide more accurate results when operated at higher flowrates.

Davis and Deutsch [1] conducted studies on Parshall flumes with nonstandard positioning: the slope of the stream, the upstream velocity profile, and alterations in Parshall flume geometry were investigated in this research. Due to the implementation of SOFA-LUMP, a 3D finite-difference code, the simulated flowrates were accurate enough and the computational cost was under the expected budget. A downside of this study was the neglect of the viscosity effects in the numerical model; however, the numerical results were close to the experimental findings. The authors concluded that the proposed numerical model could be used as a guideline to determine the results for nonstandard Parshall flumes, and that the numerical model was the best substitute for laboratory experiments or field installations for accurate results.

Sun et al. [2] investigated the flow in a flume with symmetrical curve obstructions on the flume's sides, and the results revealed that there was an incremental velocity increase within the throat section and a sudden flowrate decrease due to the introduction of a submerged flow condition at the end of that section. A comparison of water levels between the laboratory experiments and the numerical simulations showed a 4.7% error value, which was described as a good agreement. Due to its high accuracy and lower head loss, the proposed curved flume was believed to be an ideal choice for implementation from mild sloped flows to flat ones, e.g., for agriculture and irrigation systems.

Savage et al. [4] tackled the common problem of nonstandard entrance wingwalls in Parshall flumes, which is often neglected. To obtain proper results, it is important to know the best upstream location to measure the head for the flume. It was shown that CFD is a better tool, providing more accurate data compared to the costly physical "build and test" method. This paper introduced a correction factor for a range of different sizes (2-8 ft) of Parshall flumes, to adjust their results, and the implementation of this study for a nonstandard Parshall flume with a free-flow condition increased the accuracy of the discharge results from a 60% error to just +/-5%.

In a study by Heyrani et al. [39], the data from seven different turbulence models were compared with the experimental results from Dursun[43]. In the paper, it was concluded that, among the Reynolds-average Navier–Stokes (RANS), Large Eddy Simulation (LES), and Detached Eddy Simulation (DES) models, the best performance was achieved by the $k-\varepsilon$ model from the RANS family, while the Dynamic K LES model was in second place. The water level results from the CFD simulations provided an error of less than 1.93%-2.08% compared to the experimental findings and were reasonably acceptable for further implementation. Although several turbulence models were examined in the study, some important ones remained unused, which are the subject of the present paper.

The objective of this paper is to extend the study by Heyrani et al. (2021) with more sophisticated, and potentially more accurate, turbulence models in order to develop highly accurate yet efficient modeling approaches for Parshall flumes. Two nonlinear $k-\varepsilon$ models, which have proved to be highly accurate in certain fluid problems, are considered. In addition, the v^2-f model, which is a compromise between the computational efficiency of two-equation models and the accuracy of the Reynolds Stress Models (RSM), is also considered in this study.

This paper is organized as follows. Governing equations and description of turbulence models are provided in Section 2, and numerical details such as mesh, boundary, and initial conditions are then described in Section 3. Next, results and discussions are presented in Section 4, and some concluding results complete the study.

4.3 Methodology

4.3.1 Description of CFD Model

As one of the most reliable tools to analyze the behavior of fluids, Computational Fluid Dynamics (CFD) is capable of calculating a wide range of related parameters by taking advantage of the recent development of computer processors. The parameters that are accurately calculated by CFD include flow velocity, temperature and pressure.

CFD models are capable of providing solutions for the flow equations or describing the behavior of a fluid when it interacts with rigid boundaries or obstacles along its path. With respect to the conservation of mass, energy, and momentum, the Navier–Stokes system of equations is derived for viscous fluids [63].

As a reliable open-source solver for computational fluid dynamics models, OpenFOAM is implemented in this study to perform reliable simulations. This computing platform uses the Finite Volume Method (FVM) and includes many specific libraries developed in C++. It is an object-oriented toolbox that can simulate a wide range of flow problems, such as two-phase flows and free-surface flows, with a wide range of turbulence models. It also has the ability to numerically solve continuum mechanics problems. [87].

Three nonlinear turbulence models are used to simulate the flow motion in this paper, i.e., the LC low-Reynold, SQ low-Reynold, and $v^2 - f$ models, which are briefly discussed in the following section.

4.3.2 Governing Equations

A viscous incompressible fluid flow is governed by a set of general three-dimensional systems of equations called the Navier–Stokes system, which consists of momentum and continuity equations. The system is described as follows [40,41]:

$$\frac{\partial u}{\partial x} + \frac{\partial v}{\partial y} + \frac{\partial w}{\partial z} = 0 \qquad (34)$$

Equation 34 is the continuity equation, followed by the three momentum equations (Equations 35-37) for different directions, i.e., x, y, and z directions.

$$\frac{\partial u}{\partial t} + u\frac{\partial u}{\partial x} + v\frac{\partial u}{\partial y} + w\frac{\partial u}{\partial z} = -\frac{1}{\rho}\frac{\partial p}{\partial x} + \nu\nabla^2 u \qquad (35)$$

$$\frac{\partial v}{\partial t} + u\frac{\partial v}{\partial x} + v\frac{\partial v}{\partial y} + w\frac{\partial v}{\partial z} = -\frac{1}{\rho}\frac{\partial p}{\partial y} + \nu\nabla^2 v \qquad (36)$$

$$\frac{\partial w}{\partial t} + u\frac{\partial w}{\partial x} + v\frac{\partial w}{\partial y} + w\frac{\partial w}{\partial z} = -\frac{1}{\rho}\frac{\partial p}{\partial z} + \nu\nabla^2 w - g \qquad (37)$$

In the above equations, fluid density is denoted by ρ, the three spatial directions of velocity are represented by u, v, and w, p denotes the total pressure, time is symbolized by t, and g is the gravitational acceleration.

4.3.2.1 RANS

The Reynolds-Averaged Navier–Stokes Model is the dominant practical method for simulating the motion of a fluid. Other methods, such as Large Eddy Simulation (LES), are computationally more expensive and still impractical for engineering applications. The viscosity-related properties of the fluid are essentially used to estimate the impact of turbulence. The variation in the turbulent kinetic energy (k) is described by an equation for k.

A variety of turbulence models are available under this category, and the application of three non-linear approaches to form a comparison with the experimental data forms the main objective of this study.

4.3.2.1.1 $v^2 - f$ Model

A modified version of the $k - \varepsilon$ model, where k represents the turbulent kinetic energy and ε denotes the energy dissipation, is called the $v^2 - f$ turbulence model, which consists of four equations to simulate the effect of turbulence to find a solution for fluid flow motion. It has two extra equations for velocity and relaxation factors, as well as the two general kinetic energy and dissipation equations. This model falls between the categories of the Reynolds Stress Models (RSM) and the original $k - \varepsilon$ model. In order to evaluate eddy viscosity with this model, the new term v^2, which represents the velocity, is implemented instead of the term for kinetic energy. The governing equations of this model are as follows:

$$\frac{\partial k}{\partial t} + \frac{\partial k u_i}{\partial x_i} = P - \varepsilon + \frac{\partial}{\partial x_j}\left(D k_{eff} \frac{\partial k}{\partial x_j}\right) + S_k \qquad (38)$$

$$\frac{\partial \varepsilon}{\partial t} + \frac{\partial \varepsilon u_i}{\partial x_i} = \frac{C'_{\varepsilon 1} P - C_{\varepsilon 2} \varepsilon}{T} \frac{\partial}{\partial x_j}\left(D \varepsilon_{eff} \frac{\partial \varepsilon}{\partial x_j}\right) + S_\varepsilon \qquad (39)$$

$$\frac{\partial \overline{V^2}}{\partial t} + \frac{\partial \overline{V^2} u_i}{\partial x_i} = kf - 6\overline{V^2} \frac{\varepsilon}{k} \frac{\partial}{\partial x_j}\left(D k_{eff} \frac{\partial \overline{V^2}}{\partial x_j}\right) + S_{\overline{V^2}} \qquad (40)$$

$$f - L^2 \frac{\partial^2 f}{\partial {x_i}^2} = (C_1 - 1) \frac{\frac{2}{3} - \frac{\overline{V^2}}{k}}{T} + C_2 \frac{P}{k} + \left(\frac{5\overline{V^2}/k}{T}\right) + S_f \qquad (41)$$

In the above equations, the length and time-scales for turbulence are denoted by L and T, while f represents the solution to the last equation. The elliptic operator is used by the $v^2 - f$ model to calculate a similar term to the strain–pressure correlation term of the RSM. There are four different

constant C terms, i.e., C_1, C_2, $C'_{\varepsilon 1}$, and $C_{\varepsilon 2}$, which are considered the constants, and the four S terms, i.e., S_k, S_ε, $S_{\overline{V^2}}$, and S_f, which are expected to be defined by the user as source terms. The reader is referred to [88] for further details and values of the coefficients.

4.3.2.1.2 Shih et al. (1998) Quadratic $k-\varepsilon$ Model (SQ)

This model is derived from the direct implementation of a basic turbulence relationship. To propose a novel algebraic equation for the Reynolds stress, an essential turbulent relationship has been applied. Two limitations are defined based on their realizability and the theory of rapid distortion and, within the inertia sublayer, the coefficients of the model are regulated using simple flows, such as surface flow and homogenous shear flow.

Quadratic and cubic terms of average velocity in the model were proposed for Reynolds stresses. This is a short version of the general formula for mean velocity gradients and turbulent stresses [89]. The rapid distortion theory was used to determine the coefficients of the model's constraints [90] of realizability [91].

The equations used to model the general turbulent shear flow are:

$$\rho_{,t} + \left(\rho U_j\right)_{,j} = 0 \tag{42}$$

$$\left(\rho U_i\right)_{,t} + \left(\rho U_i U_j\right)_{,j} = -P_{,i} + \left[\mu\left(U_{i,j} + U_{j,i} - \frac{2}{3}U_{k,k}\delta_{ij}\right) - \rho\overline{u_i u_j}\right]_{,j} \tag{43}$$

$$\left(\rho k\right)_{,t} + \left(\rho U_i k\right)_{,i} = \left[\left(\mu + \frac{\mu_T}{\sigma_k}\right)k_{,j}\right]_{,j} - \rho\overline{u_i u_j}U_{i,j} - \rho\varepsilon \tag{44}$$

$$\left(\rho\varepsilon\right)_{,t} + \left(\rho U_i \varepsilon\right)_{,i} = \left[\left(\mu + \frac{\mu_T}{\sigma_\varepsilon}\right)\varepsilon_{,j}\right]_{,j} + C_1 f_1 \rho S\,\varepsilon - C_2 f_2 \rho\frac{\varepsilon^2}{k + \sqrt{v\varepsilon}} + C_3\frac{\mu\mu_T}{\rho}S_{,j}S_{,j} \tag{45}$$

where S in the above equation is defined as:

$$S = \sqrt{2S_{ij}S_{ij}}\,, \qquad S_{ij} = \frac{1}{2}\left(U_{i,j} + U_{j,i}\right) \tag{46}$$

The nonlinear model for the Reynolds stresses is:

$$
\begin{aligned}
-\rho\overline{u_i u_j} &= -\frac{2}{3}\rho k\,\delta_{ij} + \mu_T\left(U_{i,j} + U_{j,i} - \frac{2}{3}U_{k,k}\delta_{ij}\right) \\
&+ A_3\frac{\rho k^3}{2\varepsilon^2}\left(U_{k,i}U_{k,j} - U_{i,k}U_{j,k}\right) \\
&+ A_5\frac{\rho k^4}{\varepsilon^3}\Big[U_{k,i}U_{k,p}U_{p,j} + U_{k,j}U_{k,p}U_{p,i} - \frac{2}{3}\Pi_3\delta_{ij} \\
&- \frac{1}{2}U_{l,l}\left(U_{i,k}U_{k,j} + U_{j,k}U_{k,i} - \frac{2}{3}\Pi_1\delta_{ij}\right) \\
&- \frac{1}{2}U_{l,l}\left(U_{k,i}U_{k,j} + U_{i,k}U_{j,k} - \frac{2}{3}\Pi_2\delta_{ij}\right)\Big]
\end{aligned} \qquad (47)
$$

$$
\Pi_1 = U_{i,j}U_{j,i} \quad , \qquad \Pi_2 = U_{i,j}U_{i,j} \ , \ \Pi_3 = U_{i,k}U_{i,p}U_{p,k} \qquad (48)
$$

The equations used to obtain the coefficients value of μ_T and A_3 to A_5 are provided below:

$$
\mu_T = C_\mu f_\mu \rho\frac{k(k+\sqrt{v\varepsilon})}{\varepsilon}, A_3 = \frac{\sqrt{1 - \frac{9}{2}C_\mu^2\left(\frac{kS^*}{\varepsilon}\right)^2}}{0.5 + \frac{3}{2}\frac{k^2}{\varepsilon^2}\Omega^*\,S^*}, A_5 = \frac{1.6\,\mu_T}{\frac{pk^4}{\varepsilon^3}\frac{7(S^*)^2 + (\Omega^*)^2}{4}} \qquad (49)
$$

$$
C_\mu = \frac{1}{4 + A_s U^*\frac{k}{\varepsilon}}\ , \qquad C_1 = max\left\{0.43, \frac{\eta}{5+\eta}\right\}, \qquad C_2 = 1.9, \qquad C_3 = 1.0, \qquad (50)
$$

$$
\sigma_k = 1.0, \qquad \sigma_\varepsilon = 1.2, \qquad U^* = \sqrt{(S^*)^2 + (\Omega^*)^2}\ , \qquad S^* = \sqrt{S_{ij}^* S_{ij}^*}, \qquad (51)
$$

$$
\Omega^* = \sqrt{\Omega_{ij}\Omega_{ij}}, \qquad \Omega_{ij} = \frac{1}{2}\left(U_{i,j} - U_{j,i}\right), \qquad S_{ij}^* = S_{ij} - \frac{1}{3}S_{kk}\delta_{ij}, \qquad (52)
$$

$$
\eta = \frac{S\,k}{\varepsilon}, \qquad A_s = \sqrt{6}\,cos\,\phi\,, \qquad \phi = \frac{1}{3}arccos\left(\sqrt{6}W^*\right), \qquad W^* = \frac{S_{ij}^* S_{ji}^* S_{ki}^*}{(S^*)^3} \qquad (53)
$$

The reader is referred to [44] for further details and values of the coefficients.

4.3.2.1.3 Lien (1996) Cubic Turbulence Model (LC)

A new version of an eddy-viscosity model for turbulent flows with high Reynolds numbers was derived in [15] by implementing a nonlinear association between the parameters of strain and Reynolds stresses. For low-Reynolds conditions, vorticity tensors were also included in this relationship to identify all the variations in the turbulence length scale close to the wall in an asymptotic manner.

Using series-expansion, a general and coordinate invariant formula for strains and stresses is possible, as follows:

$$\frac{\overline{u_i' u_j'}}{k} = \frac{2}{3}\delta_{ij} - \frac{\nu_T}{k}S_{ij} + C_1\frac{\nu_T}{\epsilon}\left[S_{ik}S_{kj} - \frac{1}{3}\delta_{ij}S_{kl}S_{kl}\right] + C_2\frac{\nu_T}{\epsilon}\left[\Omega_{ik}S_{kj} + \Omega_{jk}S_{ki}\right] + C_3\frac{\nu_T}{\epsilon}\left[\Omega_{ik}\Omega_{jk} - \frac{1}{3}\delta_{ij}\Omega_{kl}\Omega_{kl}\right] + HOT \quad (54)$$

where C_μ and C_1 to C_3, proposed by [92] and only applicable to high-Reynolds areas, are:

$$C_\mu = \frac{0.667}{A_1 + S + 0.9\Omega}\Big|_{A_1=1.25}, \quad (55)$$

$$C_1 = \frac{3/4}{(1000 + S^3)}, \qquad C_2 = \frac{15/4}{(1000 + S^3)}, \qquad C_3 = \frac{19/4}{(1000 + S^3)} \quad (56)$$

$$S_{ij} = \frac{\partial u_i}{\partial x_j} + \frac{\partial u_j}{\partial x_i}, \qquad \Omega_{ij} = \frac{\partial u_i}{\partial x_j} + \frac{\partial u_j}{\partial x_i}, \qquad S = \frac{k}{\epsilon}\sqrt{\frac{1}{2}S_{ij}S_{ij}}, \quad (57)$$

$$\Omega = \frac{k}{\epsilon}\sqrt{\frac{1}{2}\Omega_{ij}\Omega_{ij}}.$$

To inspect the consequence of streamline curvature, a cubic correction proposed by [93] is also used:

$$HOT = C_4\frac{\nu_T k}{\epsilon^2}\left(S_{ki}\Omega_{lj} + S_{kj}\Omega_{li}\right)S_{kl} + C_5\frac{\nu_T k}{\epsilon^2}\left(S_{kl}S_{kl} - \Omega_{kl}\Omega_{kl}\right)S_{ij} \quad (58)$$

where:

$$C_4 = -10C_\mu^2 \qquad C_5 = -2C_\mu^2 \quad (59)$$

The turbulent viscosity ν_T obtained from the $k-\varepsilon$ modelling framework is described as:

$$\nu_T = C_\mu\frac{k^2}{\epsilon} \quad (60)$$

The reader is referred to [45] for further details and values of the coefficients.

4.3.3 Numerical Setup

The interFoam solver from the OpenFOAM family was chosen as the solver in this study, as it provides a blend of applications of the VoF method and the finite-volume method [39]. The Euler and Crank–Nicolson schemes were implemented as first- and second-order time schemes, respectively, to discretize the temporal term, while the Gauss linear method was applied for the gradient terms. The results from the two different temporal discretization schemes used in this study showed no significant differences, i.e., no significant improvement was observed when the second-order scheme was used. Therefore, using either method has no effect on the reduction in error. In other words, the time scheme has a negligible impact as the source of error. Within this solver, different schemes were used for different purposes, such as the corrected Gauss linear scheme for the Laplacian scheme and a linear scheme for the purpose of discretization of the interpolation terms.

As the initial condition, the inflows of the flume for different scenarios were constant, i.e., 10 l/s, 20 l/s, and 30 l/s. Similar to Heyrani et al. [39], the flow passing through the walls was considered to be zero, and no dissipation or acceleration was initially defined in the model.

4.3.3.1 Boundary Conditions

Figure 32 provides a schematic side and top view of the boundary condition considered in this simulation, where the flow enters and exits from one end to another while passing above the bed, which was defined as a wall. Over the flow is the atmosphere boundary, and the condition at the outlet is zero gradient. The volume of fluid method was implemented for the surface of the flow with regard to the zero-pressure state where the two fluids, i.e., liquid and air, meet.

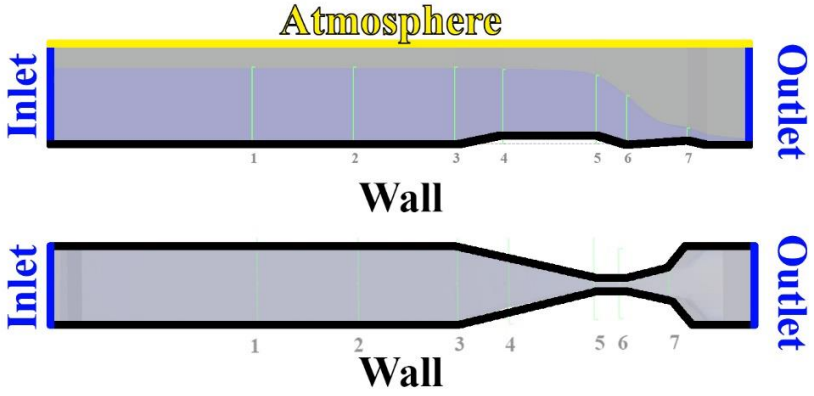

Figure 32:Side and top view of boundary condition of the modeled Parshall flume.

4.3.3.2 Mesh Sensitivity Analysis

Implementing the right mesh size, i.e., the mesh closest to the optimum grid size, allows for the simulation to produce the results that are the closest to the actual data, i.e., experimental results, with an optimal computational cost. For the simulations in this study, a mesh sensitivity analysis was performed to determine the best grid size for the structured mesh that was used.

In this procedure, the refined mesh resolution was progressively increased until no further changes were obtained in the results. Figure 33 describe the four steps taken to find the optimum grid size in this study. This was started with 52,000 cells in total, progressing to 270,000 over three steps. The data quality resulting from the progression to the second step, i.e., from 52,000 to 75,000 cells, had significant changes, but on proceeding to 270,000, there were no significant changes recorded in the quality of the simulated data. Therefore, no further increase in the number of cells is recommended after 75,000.

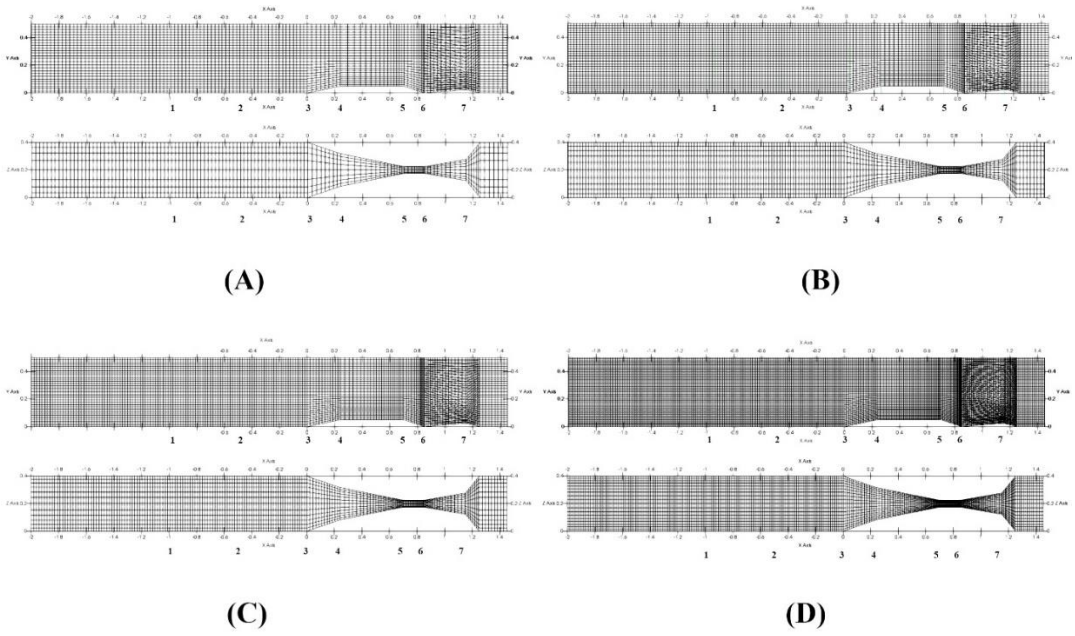

Figure 33: Mesh sensitivity analysis: side and top views of the Parshall flume mesh with different cell numbers: (A) with 27,000 cells; (B) with 52,000 cells; (C) with 75,000 cells; (D) with 270,000 cells.

4.3.4 Data

The trials that resulted in the experimental data were conducted by [43] at the hydraulic laboratory of Firat University in Elazig, Turkey. All experiments were completed in a flume with a rectangular shape and fixed dimensions of 0.4 m width, 5 m length, and 0.6m depth. Although the scope of Dursun's study was the measurement of dissolved oxygen in the fluid before and after entering and exiting the flume, in the present study, only data for water levels were used. Flowrates of 10, 20, 30, and 40 l/s were chosen, which were measured with the help of an electromagnetic flow meter within a modifiable Parshall flume to obtain results that were sufficient to draw conclusions.

The time taken for the simulation to reach steady state was 50 seconds. With respect to the existing hardware that performed the simulation, i.e., Intel Xeon Processor E5-2683 v3 (35M Cache, 2.00 GHz) the total time taken to achieve steady-state, i.e., 50 seconds, was approximately 4 hours. Considering the total number of the cells used in all three simulations, i.e., 75000, the nonlinear model is not a costly model and could be considered in the future by other researchers.

The optimum number of time-steps to achieve a steady water level was found to be 150. The maximum height fluctuations were found to be less than 2% of the steady level height. ParaView was used as post-processing software to demonstrate the water levels and other properties of the flow passing through the flumes. To determine the height of a column of water as a representative segment in each selected cross-section, the line of intersection between two perpendicular planes passing through the column point was found. Then, using the value of the Y coordinate of each datapoint, the water level was determined.

4.4 Results

The water levels at different sections of the flume were measured for comparison with the experimental results obtained by Dursun [43]. Figure 27 illustrates the geometry and dimensions of the Parshall flume used in the simulation. Water enters the main channel, which has a width of 40 cm, i.e., cross-sections 1 and 2, and, with the help of wing walls, it gradually enters the throat section, which has a 5-cm wall-to-wall distance. The length of the throat, i.e., the distance between cross-sections 5 and 6, is 15 cm. Finally, the flow passes the divergence section, where the slope of the bed gradually becomes positive after cross-section 6.

As shown in Figure 34, seven locations were chosen along the x-axis to assess the water levels for this experiment. As, in the previous study by Heyrani et al. [39], the adjustment of the first sampling location was suggested to obtain more accurate results, cross-section number one was shifted forward, to where fewer fluctuations occur. The locations of the remaining cross-sections were selected as at the beginning of each transition in the flume, i.e., cross-sections 3 and 4 were where the convergence section starts and cross-section 5 was at the start of the throat section. The remaining cross-sections followed the same pattern.

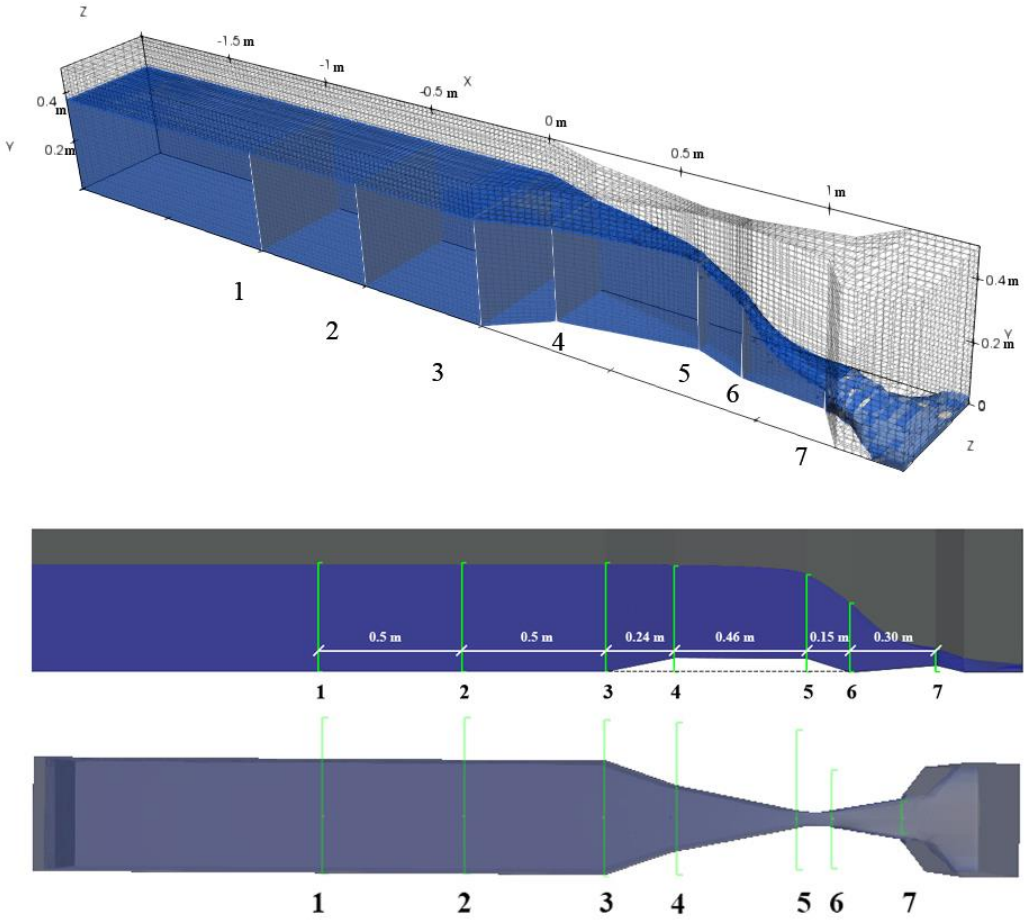

Figure 34: Location of cross-sections: 3D view (top), side view (middle), and top view (bottom).

The model was run with four different grid sizes to find the most suitable one, to obtain better-quality data. Among the different cell quantities tried in this study, i.e., 27,000, 52,000, 75,000, and 275,000, the results tended to remain the same with cell numbers of 52,000 and above.

The models were also run with three different flowrates, i.e., 10 l/s, 20 l/s and 30 l/s, and the smallest error was achieved for the 20 l/s discharge.

Figure 35 illustrates the water levels obtained using the three different turbulence models versus the experimental results from Dursun [43]. The performance of the nonlinear models was found to be more precise compared to the other turbulence models used by Heyrani et al. [39]. The error value derived with Equation 62 for the $v^2 - f$ model, which was the lowest among the three, was 0.76%.

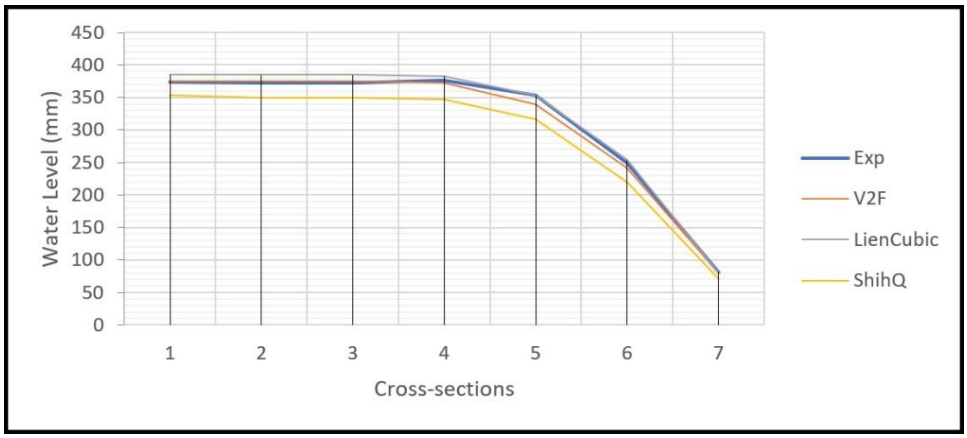

Figure 35: Comparison of water levels over the flume for the $v^2 - f$, LC, and SQ $k - \varepsilon$ models versus the experimental results.

Figure 36 shows the velocity gradient of the flow passing through the flume. The contraction at the beginning of the throat, i.e., cross-section 5, forces the flow to gain velocity until it reaches its highest point at cross-section 7, where it experiences the maximum velocity downstream at the second diverging section. Parshall flume's design leads to an increase in flow velocity at certain sections, while the flowrate remains constant.

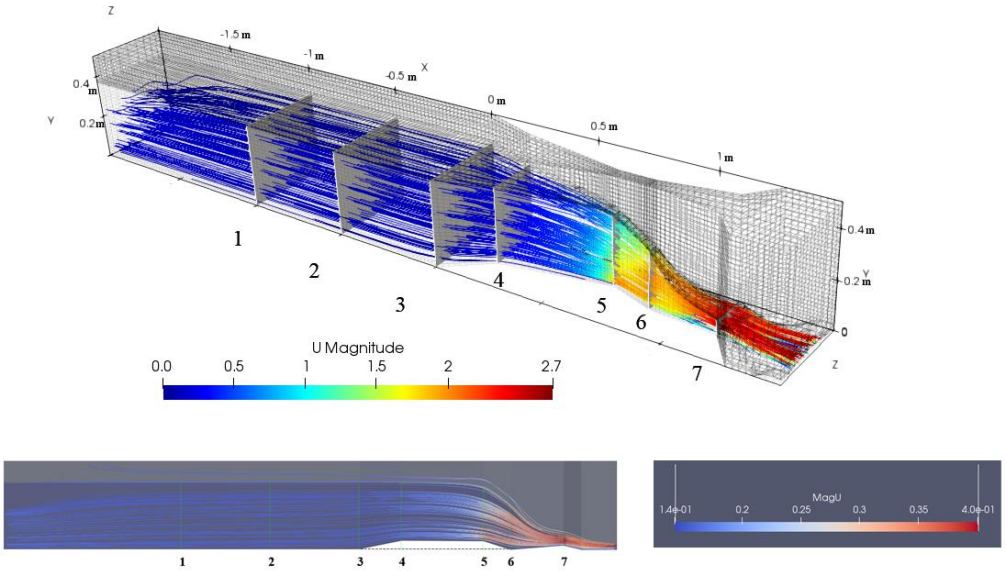

Figure 36: Velocity distribution gradient map.

The velocity profiles at cross-sections 5, 6, and 7 are presented in Figure 37. As shown in Figure 36, the flow speed variation gradually increases along the flow path. At different cross-sections in Figure 37, the maximum speeds were 0.97, 1.21, and 2.45 m/s, respectively, from cross-sections 5 to 7. Due to the shape of the flume, the distribution of the velocity profiles was varied in shape, e.g., at cross-section 5 it was distributed evenly, but as the flow moves forward, the velocity concentration shifted toward the center of the cross-section. The diverging shape of section 7 is the reason that the velocity distribution was concentrated at the sides and not the center.

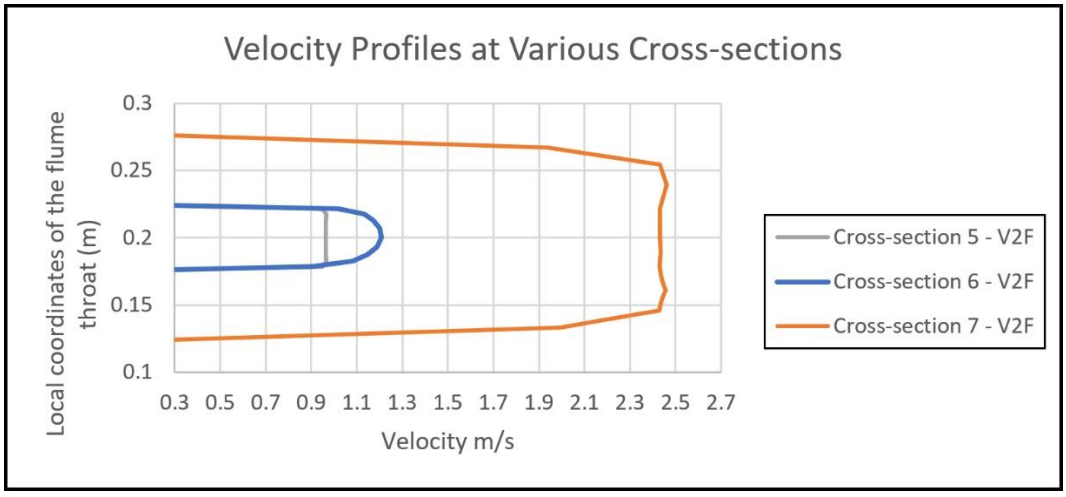

Figure 37: Velocity profiles for different cross-sections.

As illustrated in Figure 38, the flow's pressure field gradient was the lowest when the flow achieved a higher speed from cross-sections 5 to 7. Due to the presence of the throat contraction, a higher pressure was present downstream over the entire flow up to the start of the throat section.

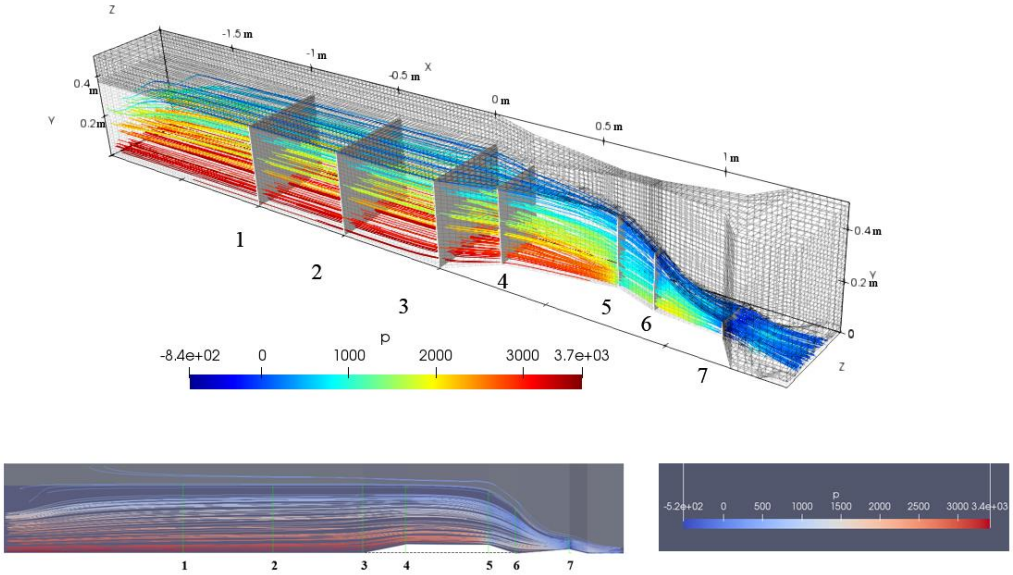

Figure 38: Pressure distribution gradient map.

4.5 Discussion

Different methods of comparing of the water levels estimated from OpenFOAM versus the experimental results from the case study are illustrated in Tables 1 and 2. The relationships used to calculate the error values are as follows:

$$Error = \frac{\left|x_{exp} - x_{sim}\right|}{x_{exp}} \tag{61}$$

$$Standard\ Error\ of\ Estimate\ (SEE) = \sqrt{\frac{\sum_{i=1}^{n}\left(x_{exp_i} - x_{sim_i}\right)^2}{n-2}} \tag{62}$$

$$R^2 = \frac{\sum_{i=1}^{n}\left(x_{exp_i} - \overline{x_{exp}}\right)^2}{\sum_{i=1}^{n}\left(x_{sim_i} - \overline{x_{exp}}\right)^2} \tag{63}$$

The Standard Error of Estimate (SEE) and the correlation coefficient (R) were calculated to estimate the errors of the simulation data. Table 4 and 5 shows the calculated error values. Equation 61 was applied to each individual cross-section and returned a separate error value for each of them, while Equations 62 and 63 provided a single overall value for each dataset, i.e., data from the LC simulation or the $v^2 - f$ model. To represent a single value for an error obtained by Equation 61, an average value was considered for all seven cross-sections.

Table 4: Error percentage calculated by Equation 61 of the estimated values for the three turbulence models across 7 cross-sections.

	Error percentage						
Cross-sections	1	2	3	4	5	6	7
$\boldsymbol{v^2 - f}$	0.29%	0.55%	0.79%	1.05%	3.92%	3.13%	2.83%
LienCubic(LC)	2.97%	3.23%	3.48%	1.60%	0.25%	2.10%	1.60%
ShihQ(SQ)	5.59%	6.42%	5.93%	7.95%	10.70%	11.57%	12.67%

Table 5: Average error, Standard Error of Estimate (SEE), Square of Correlation coefficient R^2 vs. experimental data

Turbulence Model	**Average Error %**	**SEE %**	$\boldsymbol{R^2}$	$\boldsymbol{(1 - R^2)}\%$
$\boldsymbol{v^2 - f}$	1.79%	0.76%	0.9971	0.29 %
LienCubic(LC)	2.17%	1.00%	0.9985	0.15 %
ShihQ(SQ)	8.69%	3.09%	0.9959	0.41 %

In an overall analysis of the error percentages, for the first four cross-sections, the $v^2 - f$ turbulence model provided the least amount of error, while the SQ model returned the highest amount of error for the same sections. Moving to the subsequent sections, $v^2 - f$ lost its superiority over the LC turbulence model, where, for all three remaining cross-sections, the LC model provided the least amount of error. The SQ model in this study delivered unacceptable

results compared to the other two, and as the average error percentages in Table 2 show, the $v^2 - f$ model was higher than the rest.

As described above, different methods were used to determine how far the simulation results were from the experimental ones. The standard square of estimate is one useful method for estimating the exactness of any prediction. The values produced by this method were 0.76% for the $v^2 - f$ model, 1.00% for the LC model, and 3.09% for the SQ model. This is another proof of the accuracy of the $v^2 - f$ model for this scenario. The correlation coefficient and the root mean square value are also counted as two other proofs of the superiority of the $v^2 - f$ turbulence model.

4.5.1 SQ Model:

The error values from this turbulence model's estimates show higher error percentages than the different methods, and the overall performance of this model was the poorest among the three. As shown in Figures 39 and 40, the average error values for the different cross-sections increased rapidly compared to the other two models. The maximum error value is recorded when the mean value of the error percentages for the seven different cross-sections is calculated.

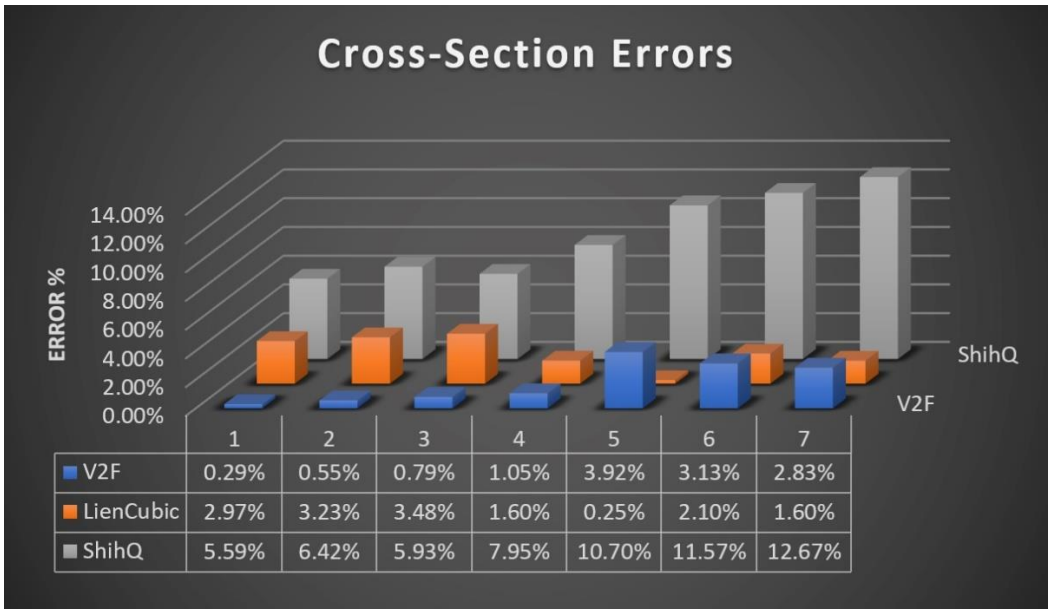

	1	2	3	4	5	6	7
V2F	0.29%	0.55%	0.79%	1.05%	3.92%	3.13%	2.83%
LienCubic	2.97%	3.23%	3.48%	1.60%	0.25%	2.10%	1.60%
ShihQ	5.59%	6.42%	5.93%	7.95%	10.70%	11.57%	12.67%

Figure 39: Calculated error magnitude for different cross-sections.

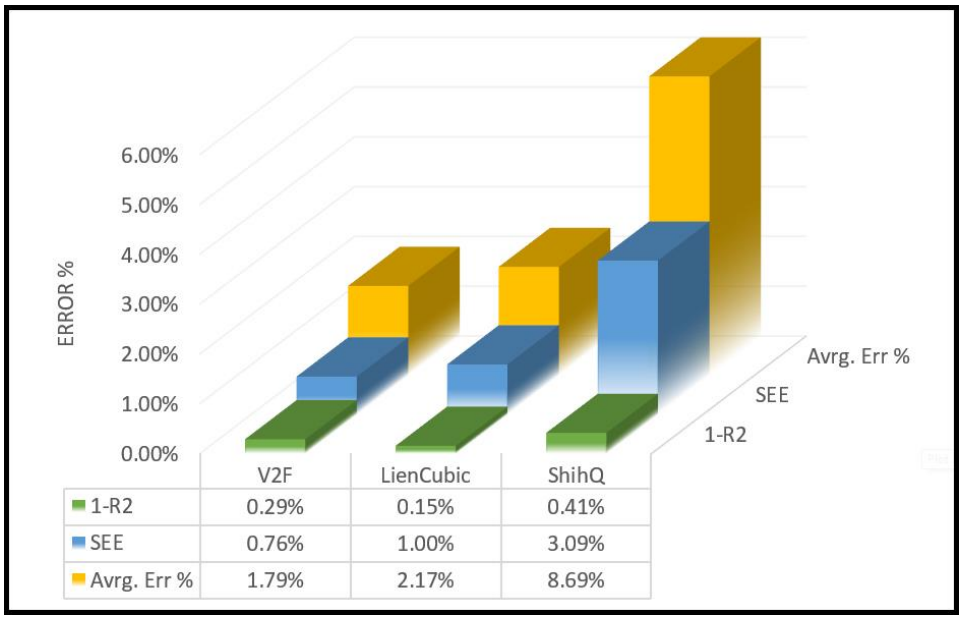

Figure 40: SEE, Average error, and $1 - R^2$ values

4.5.2 LC Model:

The correlation coefficient values that were closest to the experimental data were obtained from this model, i.e., 1-0.15%=0.9985 (99.85%), as shown in Figure 33. Additionally, the last three cross-sections tended to have the lowest error percentage values under the Lien Cubic model. This model produces error values that are almost identical to the $v^2 - f$ model, but slightly higher. Compared to the SQ model, after the $v^2 - f$ model, the data from the LC model are considered reliable.

4.5.3 $v^2 - f$ Model:

Of all the methods used to determine the error percentages of the estimated water levels, compared to the experimental one, this model provided the least error and was the most accurate. Aside from the lack of accuracy regarding the last three cross-sections, i.e., 5, 6, and 7, this model is the most recommended based on the results of this study.

4.6 Conclusions

The objective of this research was to study the reliability of numerical simulations of a Parshall flume using various nonlinear turbulence models. This is the first time that these state-of-the-art turbulence models have been employed to investigate the hydrodynamic performance of the Parshall flumes.

This study was specifically performed in alignment with the previous research conducted by Heyrani et al. [39]; however, the methods and turbulence models described here have been enhanced to provide more accurate results. Additionally, the recommendations offered in the other paper are implemented in this study where applicable, i.e., in the selection of locations for cross-section number 1. The following points are the main highlights of this research:

The comparison of three nonlinear turbulence models, i.e., the LC, SQ, and $v^2 - f$ models, reveals that the results obtained from these nonlinear models, except for the SQ model, lead to higher accuracy when compared with the experimental data, as shown in Tables 1 and 2, where the mean error values over all seven cross-sections are 1.79% and 2.17% for the $v^2 - f$ and LC models, respectively.

The use of $v^2 - f$ and LC models in this study is considered a significant improvement since, in the previous study by Heyrani et al.[39], with the similar initial criteria of the model parameters, none of the seven turbulence models from the three different families of RANS, LES and DES were able to provide the accuracy of the $v^2 - f$ and LC results when compared to the experimental data, especially the $v^2 - f$ model. However, these two non-linear turbulence models could be considered when the highest accuracy is demanded under similar conditions.

The performance of the quadratic model in this simulation was not adequate and led to a high error percentage, well beyond the desired boundary. Hence, it is strongly recommended that, if the nonlinear model is chosen, the quadratic model is not used when dealing with Parshall flume modeling with similar specifications and flowrate value.

The results strongly support the possibility of using CFD simulation as a reliable and cost-effective solution for a variety of different hydraulic projects. It was not only proven to be cost-effective compared to laboratory-scale simulations, but is also less time-consuming, depending on how powerful the computer system is.

With respect to the enhancement of the Parshall flume design, implementing CFD software is a key element to improving common designs that are used and approved by many different authorities. More studies and laboratory experiments are needed to determine the optimum design, but the results from this study support the possibility of skipping or supplementing the use of experimental data and substituting them with bias-corrected simulation data.

Although the findings presented in this study show acceptable level of error, which are less than 1% with the Standard Error of Estimate method, more research is needed to determine the best

combination of different turbulence models for use under various hydraulic conditions, to design Parshall flumes. This will be undertaken with the aim of determining the best numerical approach.

Chapter 5

Conclusions and Recommendations for Future Work

5.1 Conclusions

The aim of this study was to provide valuable insight into the implementation of CFD methods in designing hydraulic structures, as a reliable source of data. This is performed based on the shape of structure and predefined parameters that contributed to the flow simulation. In conclusion;

- The results from Chapters 3 & 4 indicate that the simulated flow obtained from $k-\varepsilon$ turbulence models provide the least error in comparison to other models. Hence, among the three distinctive families of numerical approaches, i.e., RANS, LES and DES, the best approach was proven to be RANS.
- The non-linear turbulence model, v^2-f turned out to be the most accurate model to describe the behavior of the flow in Parshall flume compared to other models. The model demonstrates 7.3% improvement in error analysis compared to the standard $k-\varepsilon$ turbulence model which provided the least error in the linear models' section. Nonetheless, all turbulence models that have been used in both studies provide errors ranging from 2 to 9%.
- The flow rate in all simulations was set based on the available experimental data i.e., 10, 20 and 30 l/s. With respect to the initial setup of the model parameters and resolution in preliminary simulations the 10 l/s case was selected as a typical case. Further investigation in higher discharge value is necessary in order to run the simulation with higher flow rate number.
- It should be mentioned that section 1 was highly affected by inflow turbulence.
- Among the papers that been selected for the review paper in Chapter 2, lack of technical paper on application of CFD on Parshall flume, a sustainable measuring hydraulic structure, was identified. Hence, it has been strongly recommended that scholars conduct studies on the benefits of the using CFD models to design Parshall flumes.
- OpenFOAM, as an open-source CFD, provided accurate time-history of water level results when flow simulation was carried out using various turbulence models.

- The idea of using numerical models to simulate the flow for a hydraulic structure was tested for a Parshall flume with a relatively narrow throat (7.62 cm). It is concluded that the simulated flow using numerical modeling in such structures provides reliable results, and close to the laboratory data. Hence, further application of this method for structures in the narrow throat Parshall flumes i.e., (15.24-cm and 22.86-cm) is strongly recommended.
- The importance of this study is revealed when protection of the environment is in focus. While testing sophisticated designs requires experimental facilities, financial resources and time, these constraints occasionally block the development of new designs, some of the limitations in design optimization are eliminated by incorporating specific CFD software. The maneuverability in design can be named as one of the innovative techniques to overcome many challenges that requires out of the box thinking.
- While the same grid size had been set for all the simulations i.e., RANS, LES and DES, RANS models performed more accurately compared to the other two methods. Therefore, the grid size in RANS method is not appropriate to use with LES and DES. Hence, it is concluded that LES and DES require to have finer mesh grid size to provide more realistic simulation results, which will computationally be expensive and impractical for engineering design applications
- Among the linear turbulence models in RANS method, the highest error obtained from the results of the $k-\omega\ SST$ model. Since the only DES turbulence model that has been used in this study was $k-\omega\ SST\ DES$, a possible reason for having a relative higher error when using the linear turbulence models is due to $k-\omega\ SST$ portion of the model.
- Using numerical modeling for flow simulation is economical when unexpected changes to the design of hydraulic structures are demanded in the final design stages. While using a CFD approach, any last-minute amendment to the geometry of the structure or to any primary parameters that are set for the initial condition is possible.
- When it comes to provide constructive recommendation on the future application of the linear and nonlinear turbulence models that have been used in this study for the Parshall flume, it is important to know the nature of the application prior to provide any suggestion. To fulfill any practical engineering needs, the implementation of linear turbulence models from RANS approach like Standard $k-\varepsilon$ is strongly suggested due to the fact that model setup it less complicated compared to nonlinear one. The computational cost is cheaper

and the quality of the produced results lies within the acceptable range for the engineering purposes. For any further academic application i.e., modeling with higher resolution, the nonlinear turbulence model i.e., $v^2 - f$ is highly recommended based on the findings in chapters 3 and 4.

- In this study, 9 models out of 10 provided water level values with less than 3% error where just one turbulence model i.e., Shih Quadratic (SQ) was unable to simulate the flow with the same level of accuracy compared to the rest of the turbulence models. Therefore, it can be interpreted as a limitation of SQ model to generate quality results of the flow passing through the 7.62 cm throat size Parshall flume. This might be due to the assumptions and parameterization of this model that may not conform to the present case. Further investigation with different sizes of Parshall flume and discharge value is strongly recommended to draw a concrete conclusion on the performance of the SQ turbulence model in Parshall flume's flow simulation.
- This study used a single size Parshall flume i.e., 7.62 cm in throat size, and implement multiple turbulence models ranging from linear to nonlinear models from 3 different numerical approaches i.e., RANS, LES and DES. The selected flow rate in all experiments were set to 10 l/s. The results of this study have been considered as a solid benchmark for any future investigation that will employ the numerical simulation to simulate the flow in the Parshall flume. The error analysis in Table 16-19 and Table 21 are unique to the configurations set in this research, and it is not suitable to be used for other sizes of Parshall flume as well. Therefore, future studies on different Parshall flume sizes are recommended.
- The computational cost of all models was between 4 to 4.5 hours.
- Accessibility feature of the computational fluid dynamic software has been considered as a great advantage to engineers and scholars. Various proposed designs of the Parshall flume as a flow measurement device for the open channels can be analyzed with lower budget than laboratory experiments. The acceptance of the CFD results provides the unique opportunity to propose the efficient design of the Parshall flume while the high accuracy of the simulated water level will help engineers to construct a proper rating curve with accurate constants.

5.2 Recommendations for Future Work

Although a large number of models were used in this study, only a small throat size Parshall flume i.e., 7.62-cm, have been investigated and more study on larger Parshall flumes remains to be performed. Therefore, it is recommended to pursue same investigation on more different throat sizes of Parshall flume i.e., 15.24-cm, 22.86-cm, 30.48-cm etc. Such flumes have been used in various industrial setups such as wastewater treatment plants.

The results of numerous turbulence models from RANS, LES and DES methods i.e., 10 linear and nonlinear models, have been contributed to this research. Implementation of more turbulence models such as LRR and SSG etc., and also, employment of DNS method for flow simulation with high resolution grid mesh are recommended for any future studies.

Since limited experimental data were used in this study, conducting a program of laboratory experiments with additional parameters i.e., velocity and temperature, would be desirable. Appropriate selection of the experimental sample data found to be pertinent as the results from the CFD would be checked against the experimental data.

The discharge in current study was limited to a single flow rate value due to lack of available experimental data. Performing accurate physical simulation on a specific size of Parshall flume will provide more datasets for simulation results to be compared with. In addition, a study of non-standard Parshall flumes is another research avenue that is recommended.

Further studies on Parshall flumes with larger throat sizes are recommended since the scope of this study only covers a small throat size Parshall flume.

Since the accuracy of flow simulations using numerical models is proportional to mesh grid size, it is recommended to use high performance computing systems with high processing capacity. This will greatly improve the quality of the results as it will be possible to achieve high resolution. Although performing this step is determined by mesh sensitivity analysis as explained in different sections in the thesis, i.e., section 2.4, fine mesh grids can capture more details of the flow compared to the coarse mesh size in LES and DES models.

The Parshall flume, is a simple measuring device that runs on only the energy of flow, with minimal maintenance requirements. Using devices that run on such sources of energy, i.e., internally powered rather than using external sources, lay out a strong foundation to protect our environment for generations to come. Hence, further numerical study on the Parshall flumes is strongly recommended.

Appendix

A1 Numerical Modeling methods:

A1.1 Direct Numerical Simulation (DNS):

In another definition, DNS refers to a total 3D and time dependent solution of the Navier-Stokes (NS) equation, in order to harvest answers for the rapid velocity of the fluid as a function of time and location. Although this is the whole purpose of DNS, regrettably, it is not achieved for the massive number of real flow conditions since the transport equations have a high degree of complexity. The Flow in a channel or over a plate are examples of limited geometries that DNS has been applied to. Intricate knowledge of programming is necessary and a tremendous amount of computation is required to run the DNS simulation. Like other CFD software, the main concern is addressed as any problems with numerical accuracy, the stability of the solutions, boundary condition's specification, convergence and the ideal use of the resources of computations. In order to picture a full detailed field of a turbulent flow, the size of the grids that should be solved with the equation must be 30 to 100 micrometers for the fluids, like water, that have low viscosity. The chosen time steps also should be small enough to capture the details of the turbulent flow, like unsteadiness and fluctuational nature. The resolution of the flows with higher Reynolds numbers requires significant computing requirements since the eddy's scales become much smaller compared to the previous small eddies, and the frequency of fluctuation grow larger. Overall, as a result of this, DNS application is suitable for the flows where the turbulence scale varies from low to moderate.

As an example, 5 to 20 million nodes in the field of flow are the expected numbers for a flow with a low Reynolds number. It also requires plenty of hours of costly complex computing time, i.e., 250 to 400 hours. It is not feasible to implement DNS for highly complex turbulent flows since the tremendous computing time and data storage is not possible at present. At this moment, DNS is considered to be a research tool to verify the results of an experiment or to analyze the perfect flow when its re-creation in the lab is not possible.

A1.2 Reynolds-Averaged Navier-Stokes equations (RANS):

As discussed, in DNS, it is difficult to find the total solutions to the transport equation of fluid due to mathematical complexity; in addition, the required capacity for the computation and time are considered to be the main issues. On the bright side, the practical application for the majority of

engineering purposes is available when it is not required to find the fine details of the fluctuations in the turbulent flows. In most cases, information provided on the mean flow is adequate, and the behaviors of each eddy is not of major concern.

As an alternative to using a very fine grid size as the cell size (10 to 100 micrometers) to illustrate the smallest eddies, a normal mesh size of 0.5 cm is implemented, for example, to find the mean flow in stirred tanks. Because of this improvement, the computation node's number is decreased to a level that can be easily handled, like 20 k to 100 k. Likewise, since the most rapid events are happening so quickly, the resolution of every sudden property of turbulent flow requires the time interval span of about 10 microseconds for discretization. But now, since in the mean flow, the changes take place so slowly, any term related to time can be resolved using larger time steps. For many cases, it is practical to adopt the fact that the mean flow is motionless, so the variables dependent on time can be totally ignored. Thus, the equation is continued to provide the solution only for the position variables [94].

A1.3 Large Eddy Simulation (LES)

In 1963, Smagorinsky proposed the Large Eddy Simulation (LES) model to predict the flow of the atmosphere. Later on, Deardoff, in 1970 [95] and Schumann [96], five years later in 1975, implemented this method in engineering flow problems. The preliminary development of LES from 1960 to 1980 was quite slow. It has been applied in the flows' building-block, mixing layers, homogenous turbulence and flows in simple channels. The rise of computing power allowed for a breakthrough in development of LES between 1980 to 1990; therefore, the community of LES users grew rapidly. Proportionally, the application of LES has shifted from simple problems to more complex ones like multi-phase flows. Aside of the recent computer power breakthrough, the main reason that LES became more popular was the fact that the RANS techniques fundamentally are not able to deal with certain types of complicated turbulent flow problems. Few parameters are included in the acceptance of LES, like the numbers of articles that are published every year in international journals, while the surge in the number of contributed talks at various conferences has had a great impact on LES recognition. Also, the large number of contributors around the world is another reason for the popularity of LES, and the availability of LES in different commercial CFD software can be highlighted as well. Lastly, there are many resources available that specifically deal with LES [97–108].

The LES approach is unlike the typical time-averaged RANS approach, where additional transport equations are solved to find the Reynolds stresses. In the LES method, motions with large scales are computed directly, while only the small-scale flows are modeled. Compared to DNS, LES has reduced the computational cost significantly. In contrast to RANS, LES is more accurate since large eddies that are modeled in RANS are solve directly. These eddies contain the turbulence energy of the flow and are accountable for the majority of the turbulent mixing and the transfer of momentum. The smallest size of eddy that can be resolved in the LES model is the same size as the grid cell size.

Moreover, the eddies with small scales tend to be more homogeneous and isotropic compared to the large ones. Hence, modelling the Sub-Grid Scale (SGS) motions is easier compared to the one for all scales within a single model, like what happens in the RANS approach. This is one of the reasons that LES models are the most promising numerical tools to simulate the transitional flow more realistically [103].

A1.4 Detached-Eddy Simulation (DES)

Due to an explicit cutoff frequency, LES is able to determine the degree of precision of the description of the fluctuations in turbulent flow. Results with high accuracy can be achieved at an inexpensive cost with no implementation of the very fine mesh resolution. As a result, DES, a combination of both RANS and LES is utilized, where near-wall regions are handled by RANS, whilst the most of the bulk region of the flow is solved through LES.

The base model in DES is the RANS model. Switching from RANS to LES in DES, requires some modifications. The most important one is to relate the turbulent length scale to the grid size. The turbulent length scale that shows up in the equation of transport provides the turbulent variables for the RANS model by its solution.

As discussed earlier, for RANS closure in the attached near-wall layers, and in the regions away from the walls where the eddy viscosity has the same scale as the grid size's squares, the SGS model is used. A region of transition occurs where the RANS and LES meet and a single solution field is continuous in an application sense. This means that there is no artificial transition between two different domains [105].

In the comparison between the DES model and URANS, DES was found to be more expensive in solving a flow in three dimensions. This is due to the size of the time steps in the simulation, which needs to be smaller; besides, refinement is necessary for the grid within some areas of the flow to

record the dynamically significant eddies in that section. Still, less than one order of magnitude is the increment that results from using DES, while compared to URANS, DES improves the accuracy of the results in most scenarios [109].

DES has a number of downsides; for example, due to the concerns toward the transition zones from RANS to LES, Travin [110] recommended implementing a blending function to achieve a smooth transition from an upwind scheme that is used in the RANS domain to the centered scheme that is used in the LES domain. The eddy viscosity is dramatically decreased without attaining the energy balance released from carrying eddies, in migration from the RANS domain to the LES domain. In the case of wall-bounded flows, several assessments on DES and LES or DNS [111–113] resulted so that even the so-called logarithmic law of the wall can be affected. With the adverse pressure gradient presence, an anomalous behavior of the model is found by Breuer [114].

A2 Further Discussion:

A2.1 Primary and secondary results of CFD

Within the results of a numerical simulation, some parameters are available directly from the output of the CFD i.e., water level, pressure, temperature and velocity, while others need to be calculated using the primary findings of the turbulence model. Flow discharge and Froude number are among the secondary parameters of the water flow that need to be derived from principal results of a CFD.

It should be mentioned that all sections were considered to ensure uniform accuracy of the model rather than just considering sections between cross-sections 4 and 5 in order to prevent local accuracy only.

The available water level data from the physical experiments on 27 modified Parshall flumes provide a reliable source to compare the simulated water level data against, at various cross sections through the flume [43]. Due to the lack of experimental results on other essential parameters i.e., velocity, reliability of the model regarding those parameters cannot be scrutinized. Therefore, no further analysis has been done on simulated data other than the water level.

An example of a calculated parameter can be found in Table 6 where the Froude numbers of simulated flow by 7 linear turbulence models have been calculated using the available velocity data at cross section no. 5, illustrated in Fig. 28. Froude number is a dimensionless value that acts

as an indicator to provide the type of flow, whether it is sub- or super- critical, at any point of interest along the flow.

Equation 64 provide the formula to calculate the Froude number, [115]

$$Fr = \frac{U}{\sqrt{g \times H_d}} \qquad (64)$$

Where U is the velocity, g is the gravitational acceleration and H_d is the hydraulic mean depth.

When the Froude number is less than 1, the flow categorized as sub-critical, and it is counted as the Super critical when the Froude number is greater than 1. Critical flow is the result of the Froude number equal to 1.

In the Parshall flume structure, the main goal of the converging section's shape is to transform the flow type from sub-critical ($Fr < 1$) to super-critical ($Fr > 1$). The Froude number calculation shows that the flow type at the entrance of the throat section at cross section 5 is nearly critical as the Froude number is slightly below 1 in all the simulations i.e., ($Fr \approx 1$). Since this type of situation had been anticipated where flow type is not yet super-critical, Therefore, a steep inclined drop had been introduced to the beginning of the throat section, right after the throat entrance, i.e., the stretch between cross section no. 5 to 6, to rectify this issue. The combination of the contraction and the negative inclination in the throat section is to assured that the flow attain enough velocity to transit into super-critical type. Table 6 provides the Froude numbers for all the cross-sections between 2 to 7.

Table 6: Result of the Froude number calculation for the numerical models and the experimental simulation at cross-section 2 to 7 using linear and nonlinear turbulence models

Turbulence models/Cross-section number		**2**	**3**	**4**	**5**	**6**	**7**
Linear Turbulence Models	$K-\varepsilon$	0.06	0.06	0.15	0.93	1.03	3.76
	RNG $K-\varepsilon$	0.06	0.06	0.15	0.92	1.02	3.84
	K omega SST	0.06	0.06	0.15	0.93	1.03	3.88
	Smagorinsky	0.06	0.06	0.14	0.86	0.97	3.43
	Dynamic K	0.06	0.06	0.14	0.88	0.98	3.77
	$K-\omega$ **SST DES**	0.06	0.06	0.15	0.93	1.03	3.90
	Realizable $K-\varepsilon$	0.06	0.06	0.15	0.92	1.02	3.84
Non-linear Turbulence Models	v^2-f	0.06	0.06	0.14	0.87	0.95	3.65
	LC	0.06	0.06	0.16	0.98	1.07	3.91
	SQ	0.06	0.06	0.16	0.99	1.10	4.19
Physical Simulation	**Experimental**	0.06	0.06	0.15	0.86	0.97	1.51

For all the turbulence models, the Reynolds number (Re) at each cross section was calculated using equation 65.

$$Re = \frac{Vd}{\nu} \qquad (65)$$

Where V is the mean velocity, d is the hydraulic radius and ν is the kinetic viscosity of the water.

The Reynolds number graphs are illustrated in Figure 90 to Figure 99. Based on the Reynolds numbers the flow classified as transitional flow in cross-sections 2 and 3, and turbulent flow over the remaining cross sections. The Reynolds number graph for the experimental simulation is presented in Figure 100.

Table 7: Result of Reynolds number calculation for the numerical models and the experimental simulation at cross-section 2 to 7 using linear and nonlinear turbulence models

Turbulence Models		2	3	4	5	6	7
Linear Turbulence Models	$K-\varepsilon$	11073	11086	15829	26044	27568	45995
	RNG $K-\varepsilon$	11059	11071	15790	25823	27494	46192
	$K\ \omega\ SST$	11078	11091	15849	25995	27670	46273
	Smagorinsky	10927	10928	15443	24889	26691	45187
	Dynamic K	10985	10986	15562	25172	26841	46027
	$K-\omega\ SST\ DES$	11080	11087	15829	25947	27595	46314
	Realizable $K-\varepsilon$	11054	11064	15773	25823	27434	46184
Non-linear Turbulence Models	v^2-f	10980	10984	15566	24986	26345	45738
	LC	11318	11336	16273	26887	28247	46347
	SQ	11372	11389	16390	26955	28578	46938
Physical Simulation	Experimental	11186	11086	15898	24876	26596	37120

As illustrated in Figure below, the variation of flow velocity in vertical direction at cross-section 5 started with rapid changes in magnitude and direction and reaches constant velocity at 50s where it is recorded as 0.36 m/s in downward direction. When the flow reaches the throat section, it experiences a back flow for a few seconds until it has been dissipated due to loss of initial momentum. The large oscillation that is shown on the Figure 41 is illustrating the changes in vertical velocity of the flow at the beginning of the throat section of the Parshall flume. It should be noted that transverse velocity is very small.

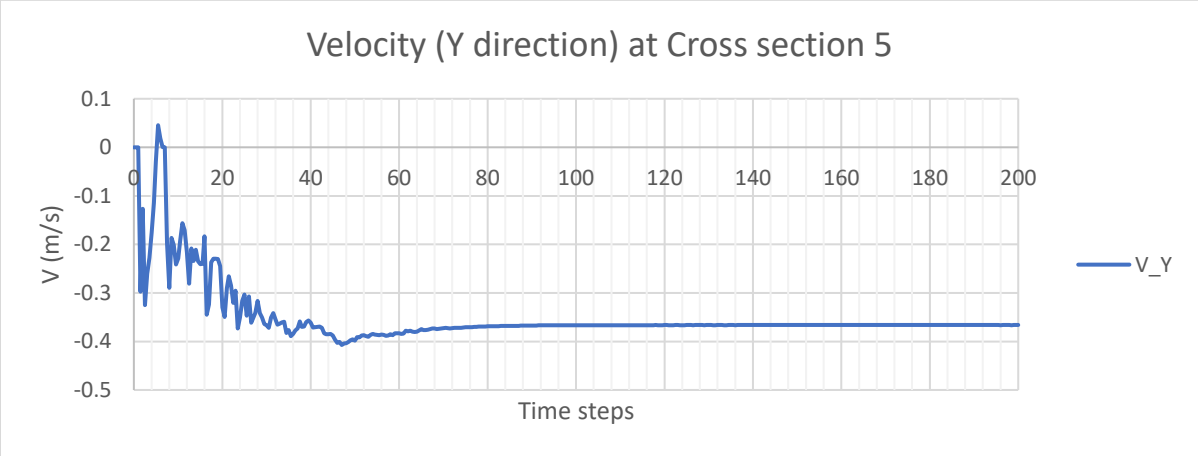

Figure 41: Velocity variation in Y direction (vertical) at Cross-section 5

A2.2 CFD Data validation

In order to analyze the accuracy of the simulated water level data from OpenFOAM, mathematical calculation based on the energy principle (Bernoulli's equation) were carried out on 4 cross sections shown in Figure 42 i.e., cross section no. 2, 4, 5 and 6. Besides, a new cross section has been analysed based on the interpolation between cross section 5 and 6 where the location of the critical depth has been determined i.e., half the distance. Figure 42 shows the location of the cross sections used to validate the simulation data that mentioned above.

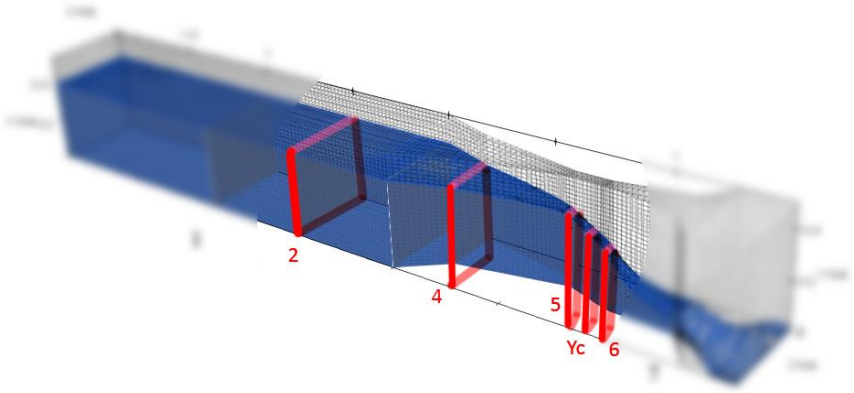

Figure 42: Selected cross sections for data comparison

Starting with the simulated water level data at cross section no. 2, the water level of the subsequent cross sections has been calculated. Detailed results of the calculation are shown in Table 7 and Figure 43. The error analysis proves that simulated and experimental data have an acceptable average bias against the calculated results using principle of energy. Simulation results from CFD provide an average error of 3.97% against the dataset generated by calculation. Nevertheless, the value for the calculated water level at cross section 2 has been obtained by applying the energy equation between critical depth cross section and cross section no. 2.

Table 8: Comparison between three different datasets i.e., experimental, simulated and analytical datasets

		Cross section 2	Cross section 4	Cross section 5	Cross section Y_c	Cross section 6
Experimental Water level (m)		0.251	0.247	0.226	0.175	0.145
Simulated Water level (m)		0.250	0.249	0.217	0.168	0.139
Calculated Water level (m)		0.239	0.249	0.210	0.160	0.130
Velocity (m/s)		0.105	0.171	0.952	1.250	1.538
Q (L/s)		10	10	10	10	10
Error analysis	**Experimental Vs. Calculated Water level**	5.02%	0.80%	7.62%	9.37%	11.54%
	Simulated Vs. Calculated water level	4.60%	0.00%	3.33%	5.00%	6.92%

Figure 43 provide an illustration of the experimental and simulation data against the calculated water level results.

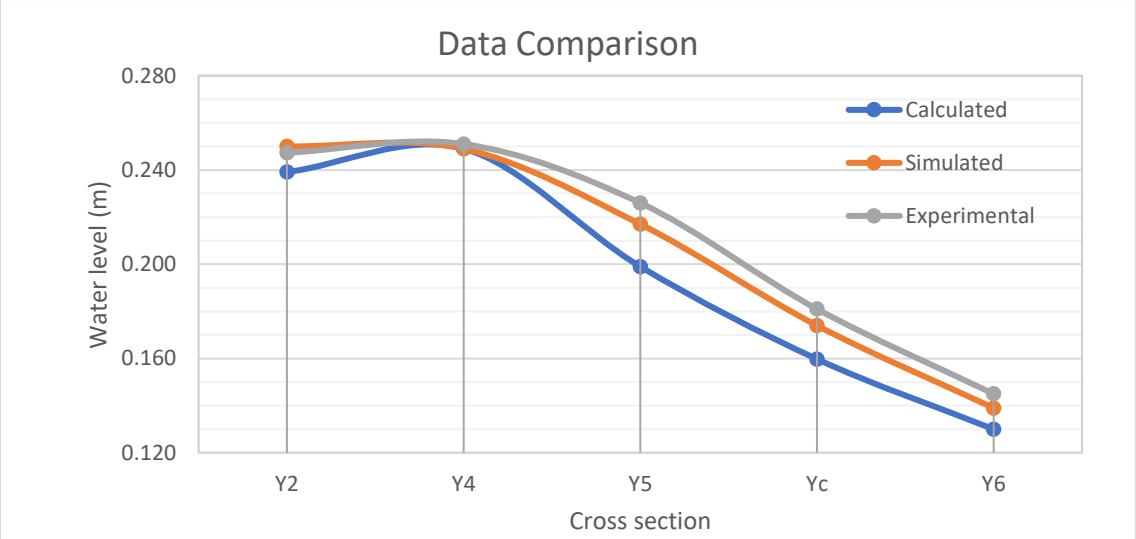

Figure 43: Comparison between different water level dataset

99 preliminary simulations have been carried out on various modifications of Parshall flume according to the experimental specifications in a study [43]. Figure 44 and Table 12 provide specifications of the Parshall flume used in the experimental study. A total number of 27 shape altered Parshall flumes (please refer to fig. 44 and Table 8 for more details) have been used in flow simulation in OpenFOAM. The preliminary results indicate which of the modified Parshall flumes was selected to be tested with multiple linear turbulence models. The standard $k-\varepsilon$ model has

been selected due to its simplicity in setup. Detailed results have been tabulated in this appendix section along with the graphs containing the illustrations of the water level at various cross sections. Error analysis has been performed for all the 99 simulations against the experimental results. To reduce the computational time the mesh grid size of the block mesh in preliminary setups were set to be coarse due to the large number of experiments. Each Parshall flume have been simulated at least with 3 different flowrates i.e., 10 l/s, 20 l/s and 30 l/s, while flume no. 10 to no. 27 were simulated with an additional flowrate value of 40 l/s. The error analysis for all the preliminary simulations indicates the candidate flume to be simulated using 7 linear turbulence models with fine mesh grid. Table 9 to 19, and figures 45 to 71 are showing the results of the preliminary simulations along with their error analysis.

Based on the result of 99 simulation on 27 different configurations of Parshall flumes, simulation on selected modifications of flume i.e., F1 and F5, were carried out using 3 non-linear turbulence models. The preliminary results of the simulation with coarse mesh have tabulated and illustrated in Table 20 and Figures 72 through 77. The results of the error analysis using Equation (30) is available in Table 21 in this appendix section.

To compare the error of the 7 linear turbulence models in Chapter 3 and the 3 nonlinear turbulence models used in chapter 4, figure 43 provides an illustrated comparison. As mentioned earlier $v^2 - f$ shows the best average error among all. Overall, the majority of the turbulence models perform with error less than 3% except Shih Quadratic i.e., 8.69% error. Also, it might be possible to improve the quality of the results for LES and DES models by making the mesh grid further fine.

The variation in the Froude number for the tested Parshall flume at cross sections number 2 to 7 in each model is illustrated in Figure 79 to Figure 88. The Froude number graph's pattern shows a tranquil flow entering the Approach are i.e., cross sections 3 to 4, and passing through the Crest area at cross sections 4 to 5. Due to the tapered reduction at Converging section, the reduction of the cross-sectional area causes the flow velocity to increase. Starting from throat section at cross-sections 5 to 7, the flow type rapidly changes to critical and supercritical flow. The specific geometry design of the Parshall flume's throat section i.e., sharp steep descend of the floor and parallel side walls, are designed to ensure the achievement of the critical flow in this section. Three main sections of the Parshall flume i.e., Converging section, Throat section & Diverging section

are shaded in each graph with different colors. The Froude number graph of the experimental data is shown in Figure 89.

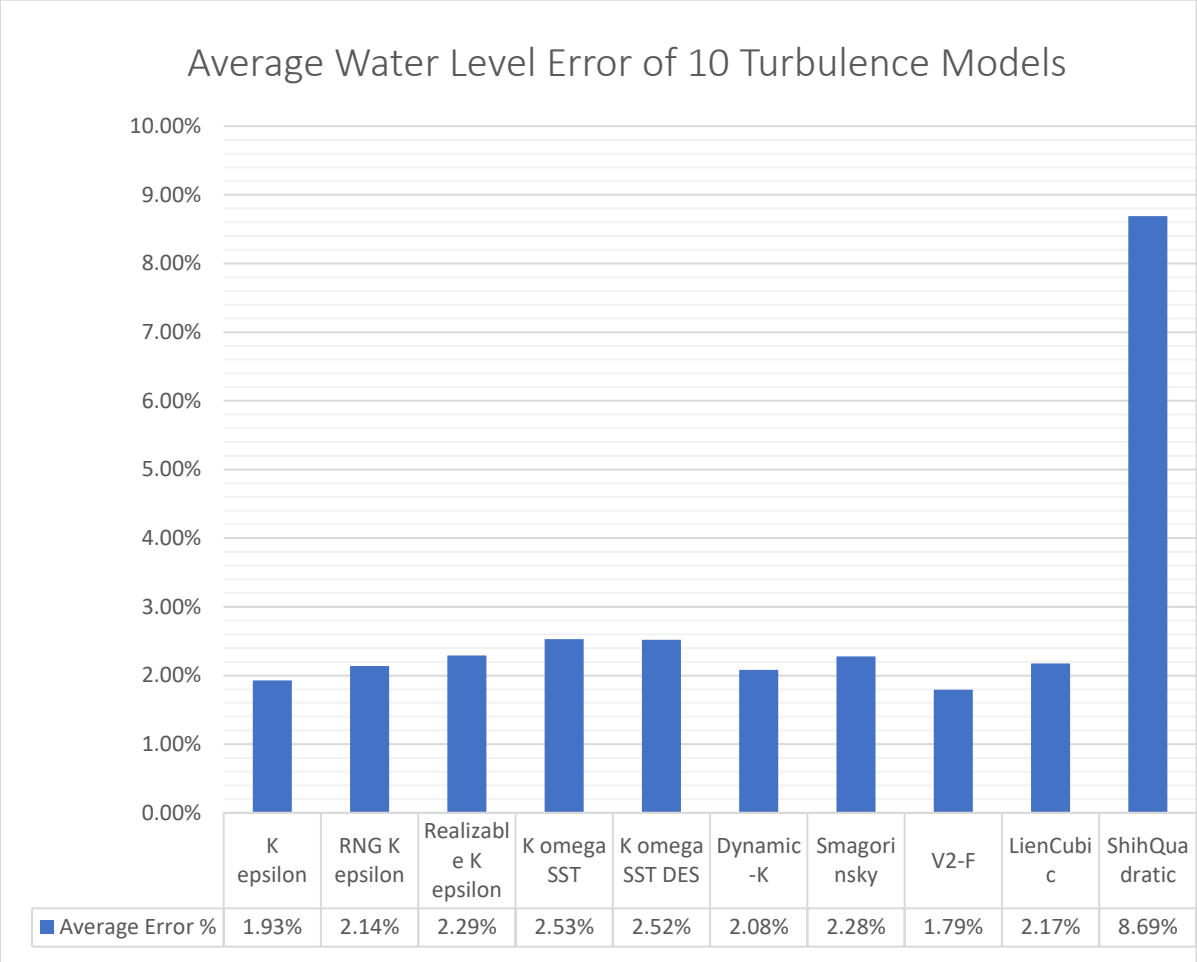

Figure 44: The average water level error percentage of different turbulence models

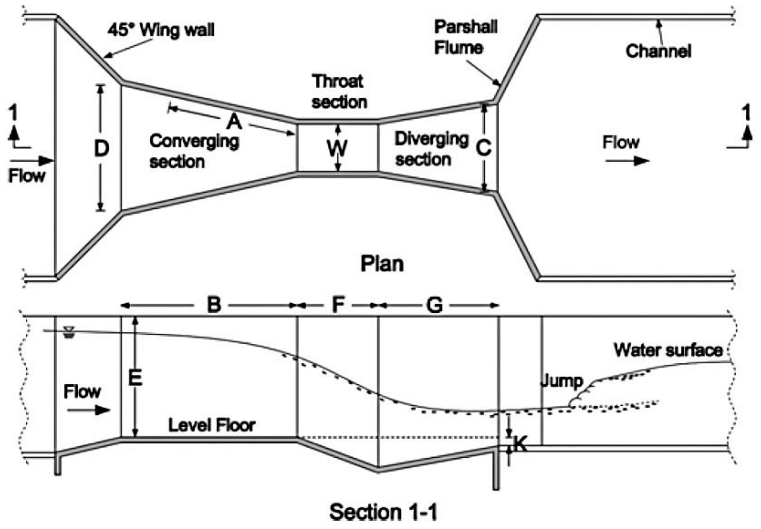

Figure 45: Geometry details of the Parshall flume used in this study [43]

Table 9: Parshall flume dimensions used for preliminary simulations [43]

Flume No.	Flume Dimensions			Flume No.	Flume Dimensions		
	W (cm)	F (cm)	K (cm)		W (cm)	F (cm)	K (cm)
F1	5.00	10	2.50	**F15**	7.62	15	7.62
F2	5.00	10	5.00	**F16**	7.62	20	2.50
F3	5.00	10	7.62	**F17**	7.62	20	5.00
F4	5.00	15	2.50	**F18**	7.62	20	7.62
F5	5.00	15	5.00	**F19**	10.0	10	2.50
F6	5.00	15	7.62	**F20**	10.0	10	5.00
F7	5.00	20	2.50	**F21**	10.0	10	7.62
F8	5.00	20	5.00	**F22**	10.0	15	2.50
F9	5.00	20	7.62	**F23**	10.0	15	5.00
F10	7.62	10	2.50	**F24**	10.0	15	7.62
F11	7.62	10	5.00	**F25**	10.0	20	2.50
F12	7.62	10	7.62	**F26**	10.0	20	5.00
F13	7.62	15	2.50	**F27**	10.0	20	7.62
F14	7.62	15	5.00				

Table 10: Experimental results vs. preliminary data from OpenFOAM for Parshall Flumes #1 to #5

Flume No.	Source	Q (L/s)	dim	Water level @ each cross-section (mm)						
				1	2	3	4	5	6	7
F1	Experimental	10	W=5	240	242	243	247	224	163	67
		20	F=10	347	349	353	352	331	261	89
		30	K=2,5	423	425	434	433	403	341	115
	Simulation	10	W=5	242	242	242	241	208	151	33
		20	F=10	352	332	332	330	295	230	52
		30	K=2,5	430	413	412	408	373	305	73
F2	Experimental	10	W=5	247	251	251	247	226	163	57
		20	F=15	354	356	358	356	331	263	78
		30	K=2,5	438	439	440	441	415	349	102
	Simulation	10	W=5	261	254	254	252	220	158	57
		20	F=15	370	361	360	358	324	256	77
		30	K=2,5	456	438	440	437	404	336	99
F3	Experimental	10	W=5	279	281	280	278	254	191	83
		20	F=20	394	396	397	399	368	304	113
		30	K=2,5	476	479	480	477	453	379	125
	Simulation	10	W=5	286	285	285	283	254	187	56
		20	F=20	400	401	401	399	364	292	79
		30	K=2,5	471	456	457	454	413	348	93
F4	Experimental	10	W=5	244	246	247	248	229	150	62
		20	F=15	357	357	360	363	339	246	83
		30	K=2,5	440	442	446	446	425	331	105
	Simulation	10	W=5	249	249	249	247	220	139	32
		20	F=15	365	365	365	363	328	234	56
		30	K=2,5	446	430	431	428	395	294	71
F5	Experimental	10	W=5	259	262	264	263	241	149	62
		20	F=10	374	373	372	377	354	249	81
		30	K=2,5	458	457	461	459	439	323	102
	Simulation	10	W=5	266	266	266	265	234	151	57
		20	F=10	382	382	382	380	346	243	79
		30	K=2,5	470	472	472	469	432	327	100

Table 11: Experimental results vs. preliminary data from OpenFOAM for Parshall Flumes #6 to #10

Flume No.	Source	Q (L/s)	dim	Water level @ each cross-section (mm)						
				1	2	3	4	5	6	7
F6	Experimental	10	W=5	273	275	276	276	251	158	86
		20	F=15	386	388	389	390	367	268	108
		30	K=2,5	472	473	475	476	447	347	126
	Simulation	10	W=5	285	285	285	283	249	165	56
		20	F=15	407	408	407	405	371	266	76
		30	K=2,5	476	468	469	464	434	331	90
F7	Experimental	10	W=5	257	261	258	259	239	144	61
		20	F=20	381	385	383	382	357	237	80
		30	K=2,5	466	471	470	470	448	322	100
	Simulation	10	W=5	255	255	254	253	226	133	32
		20	F=20	376	376	376	374	342	218	53
		30	K=2,5	453	460	458	453	416	286	70
F8	Experimental	10	W=5	266	266	266	270	246	141	54
		20	F=15	380	381	382	382	360	235	77
		30	K=2,5	466	469	471	471	448	313	96
	Simulation	10	W=5	271	271	271	269	241	139	57
		20	F=15	378	373	371	369	335	218	72
		30	K=2,5	462	448	446	442	414	280	87
F9	Experimental	10	W=5	289	290	287	291	266	152	91
		20	F=15	409	408	409	411	385	260	111
		30	K=2,5	493	488	489	501	489	356	135
	Simulation	10	W=5	290	289	289	288	254	142	56
		20	F=15	409	410	409	407	373	248	75
		30	K=2,5	486	474	474	471	427	305	89
F10	Experimental	10	W=7.5	194	194	192	195	167	128	64
		20	F=10	282	285	284	286	252	209	83
		30	K=2,5	353	353	357	356	319	270	101
		40		408	410	413	414	378	327	118
	Simulation	10	W=7.5	190	187	187	186	162	123	31
		20	F=10	278	271	272	269	239	197	49
		30	K=2,5	352	339	339	335	297	253	71
		40		420	390	391	387	350	299	88

Table 12: Experimental results vs. preliminary data from OpenFOAM for Parshall Flumes #11 to #14

Flume No.	Source	Q (L/s)	dim	Water level @ each cross-section (mm)						
				1	2	3	4	5	6	7
F11	Experimental	10	W=7.5	209	213	211	210	180	127	61
		20	F=10	297	302	302	303	269	208	82
		30	K=5	367	371	369	370	331	275	98
		40		424	427	432	429	387	333	115
	Simulation	10	W=7.5	208	206	206	203	176	129	54
		20	F=10	310	310	309	306	271	219	76
		30	K=5	369	363	363	361	326	279	95
		40		439	417	418	413	376	328	111
F12	Experimental	10	W=7.5	234	237	234	232	203	148	84
		20	F=10	320	326	327	327	294	240	106
		30	K=7,5	389	395	394	393	362	308	126
		40		440	447	451	452	421	365	146
	Simulation	10	W=7.5	236	235	234	231	204	158	52
		20	F=10	333	321	320	317	283	237	71
		30	K=7,5	386	388	387	383	350	299	90
		40		457	430	430	426	388	343	105
F13	Experimental	10	W=7.5	189	191	193	195	171	112	60
		20	F=15	288	289	292	291	268	190	80
		30	K=2.5	360	360	364	364	336	252	99
		40		414	415	417	419	392	307	116
	Simulation	10	W=7.5	195	194	194	192	166	106	31
		20	F=15	290	279	278	275	242	177	49
		30	K=2.5	360	348	347	343	310	232	66
		40		427	430	430	425	387	301	93
F14	Experimental	10	W=7.5	212	212	212	213	184	110	59
		20	F=15	304	303	304	304	272	191	83
		30	K=5	374	376	375	377	347	262	98
		40		426	430	430	431	401	312	116
	Simulation	10	W=7.5	216	213	213	211	184	112	54
		20	F=15	312	312	312	309	274	201	75
		30	K=5	357	354	353	348	312	235	86
		40		440	425	423	416	379	297	108

Table 13: Experimental results vs. preliminary data from OpenFOAM for Parshall Flumes #15 to #18

Flume No.	Source	Q (L/s)	dim	Water level @ each cross-section (mm)						
				1	2	3	4	5	6	7
F15	Experimental	10	W=7.5	232	233	232	226	200	115	81
		20	F=15	323	325	323	321	294	212	101
		30	K=7.5	394	396	398	396	364	271	124
		40		449	452	457	454	429	335	143
	Simulation	10	W=7.5	238	230	230	227	194	116	51
		20	F=15	338	338	337	334	299	225	73
		30	K=7.5	388	394	388	384	346	266	86
		40		434	431	431	425	390	304	98
F16	Experimental	10	W=7.5	201	202	200	201	178	104	62
		20	F=20	300	304	300	299	274	178	80
		30	K=2,5	374	377	378	377	350	244	103
		40		434	438	440	441	411	298	119
	Simulation	10	W=7.5	197	195	194	193	168	99	30
		20	F=20	296	285	284	281	252	167	48
		30	K=2,5	378	363	364	361	328	224	67
		40		420	422	422	418	381	269	83
F17	Experimental	10	W=7.5	215	214	214	215	187	102	57
		20	F=10	309	308	310	311	280	177	77
		30	K=2,5	380	383	383	384	355	240	94
		40		435	440	442	439	413	295	110
	Simulation	10	W=7.5	215	213	213	211	185	102	54
		20	F=10	310	290	289	287	256	164	68
		30	K=2,5	367	362	362	359	323	215	86
		40		391	322	326	327	301	196	77
F18	Experimental	10	W=7.5	231	233	233	227	202	103	78
		20	F=10	324	326	326	322	295	180	99
		30	K=5	395	400	402	401	371	246	118
		40		457	459	459	457	428	299	138
	Simulation	10	W=7.5	237	236	235	234	205	104	51
		20	F=10	320	304	302	300	266	172	65
		30	K=5	383	373	320	366	327	225	81
		40		458	374	373	370	334	229	80

Table 14: Experimental results vs. preliminary data from OpenFOAM for Parshall Flumes #19 to #22

Flume No.	Source	Q (L/s)	dim	Water level @ each cross-section (mm)						
				1	2	3	4	5	6	7
F19	Experimental	10	W=7.5	161	163	162	161	135	102	61
		20	F=10	236	238	240	241	205	170	76
		30	K=7,5	298	303	302	305	266	227	95
		40		349	352	353	354	315	276	113
	Simulation	10	W=7.5	150	150	149	147	121	79	28
		20	F=10	238	231	232	229	193	151	45
		30	K=7,5	298	289	286	282	243	189	61
		40		335	295	294	290	253	193	63
F20	Experimental	10	W=7.5	180	180	181	180	143	99	57
		20	F=15	252	255	254	256	217	168	74
		30	K=2.5	318	318	319	317	276	227	88
		40		361	369	363	370	326	274	107
	Simulation	10	W=7.5	168	168	167	164	134	85	52
		20	F=15	249	241	239	237	202	154	67
		30	K=2.5	322	310	302	298	258	208	83
		40		332	290	289	285	244	199	79
F21	Experimental	10	W=7.5	204	202	206	203	175	124	86
		20	F=15	283	283	284	284	251	202	101
		30	K=5	344	343	345	345	311	261	118
		40		392	395	395	396	363	311	137
	Simulation	10	W=7.5	197	196	196	193	161	109	52
		20	F=15	288	288	287	284	242	192	69
		30	K=5	337	319	317	314	271	223	79
		40		370	285	282	279	238	191	68
F22	Experimental	10	W=7.5	168	167	169	169	144	94	58
		20	F=15	250	252	256	251	220	157	77
		30	K=7.5	315	316	315	313	284	218	93
		40		363	366	370	368	331	269	106
	Simulation	10	W=7.5	155	154	154	152	127	76	27
		20	F=15	253	238	236	234	199	141	44
		30	K=7.5	300	300	299	296	258	187	62
		40		332	284	278	276	241	177	57

Table 15: Experimental results vs. preliminary data from OpenFOAM for Parshall Flumes #22 to #26

Flume No.	Source	Q (L/s)	dim	Water level @ each cross-section (mm)						
				1	2	3	4	5	6	7
F23	Experimental	10	W=7.5	179	184	182	184	152	87	56
		20	F=20	258	262	260	260	219	156	76
		30	K=2,5	322	322	325	323	281	212	91
		40		368	372	374	371	332	255	109
	Simulation	10	W=7.5	175	174	174	171	141	78	52
		20	F=20	258	253	254	251	212	150	68
		30	K=2,5	339	305	306	303	265	198	83
		40		366	329	329	328	285	211	89
F24	Experimental	10	W=7.5	234	237	234	232	203	148	84
		20	F=10	320	326	327	327	294	240	106
		30	K=2,5	389	395	394	393	362	308	126
		40		440	447	451	452	421	365	146
	Simulation	10	W=7.5	196	196	195	193	160	81	52
		20	F=10	284	265	264	261	226	151	64
		30	K=2,5	350	309	308	305	266	193	76
		40		410	343	343	339	298	225	84
F25	Experimental	10	W=7.5	189	191	193	195	171	112	60
		20	F=10	288	289	292	291	268	190	80
		30	K=5	360	360	364	364	336	252	99
		40		414	415	417	419	392	307	116
	Simulation	10	W=7.5	162	161	160	159	133	74	28
		20	F=10	255	255	254	251	216	143	48
		30	K=5	305	303	304	301	262	178	60
		40		345	321	321	317	279	188	65
F26	Experimental	10	W=7.5	212	212	212	213	184	110	59
		20	F=10	304	303	304	304	272	191	83
		30	K=7,5	374	376	375	377	347	262	98
		40		426	430	430	431	401	312	116
	Simulation	10	W=7.5	179	179	178	177	147	74	52
		20	F=10	266	247	219	212	207	126	66
		30	K=7,5	316	306	300	298	265	178	82
		40		388	388	387	383	339	241	104

Table 16: Experimental results vs. preliminary data from OpenFOAM for Parshall Flumes #27

Flume No.	Source	Q (L/s)	dim	Water level @ each cross-section (mm)						
				1	2	3	4	5	6	7
F27	Experimental	10	W=7.5	232	233	232	226	200	115	81
		20	F=15	323	325	323	321	294	212	101
		30	K=2.5	394	396	398	396	364	271	124
		40		449	452	457	454	429	335	143
	Simulation	10	W=7.5	201	200	199	198	164	74	51
		20	F=15	288	266	266	262	225	133	65
		30	K=2.5	342	314	316	313	270	180	77
		40		402	328	327	324	280	186	81

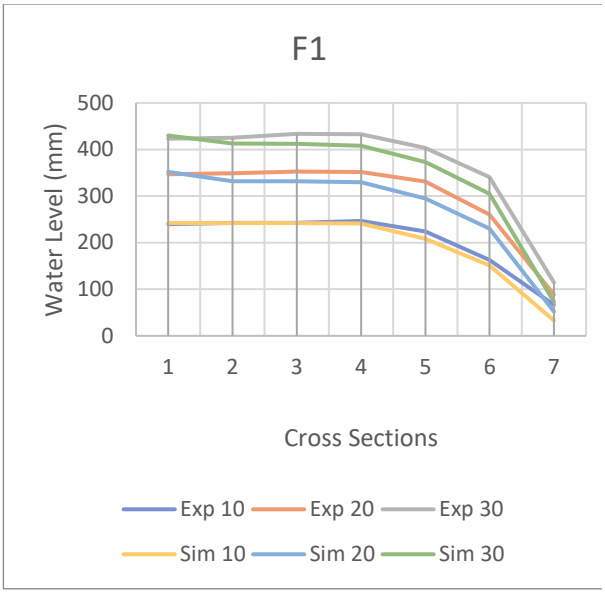

Figure 46: Experimental vs. simulation data in Parshall flume F1

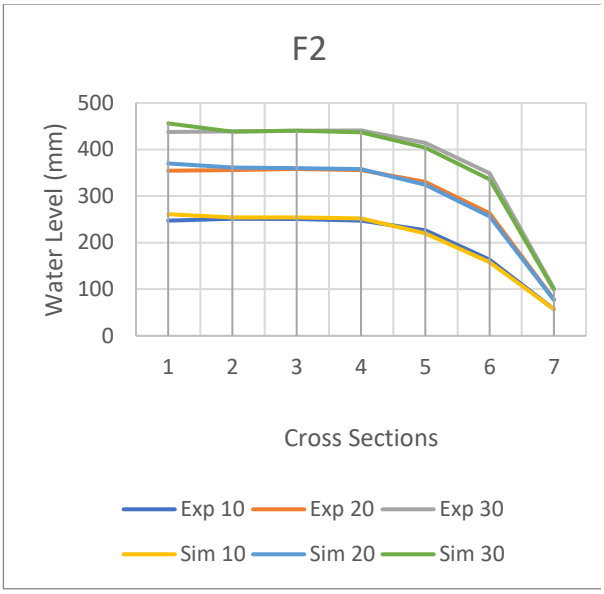

Figure 47: Experimental vs. Simulation data in Parshall flume F2

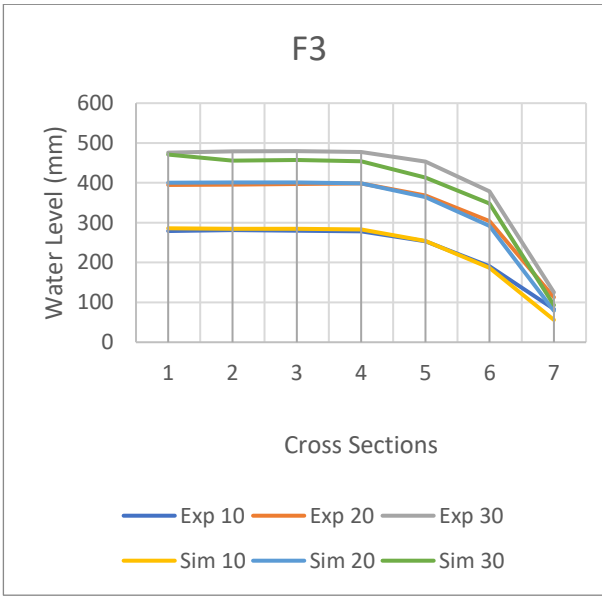

Figure 48: Experimental vs. Simulation data in Parshall flume F3

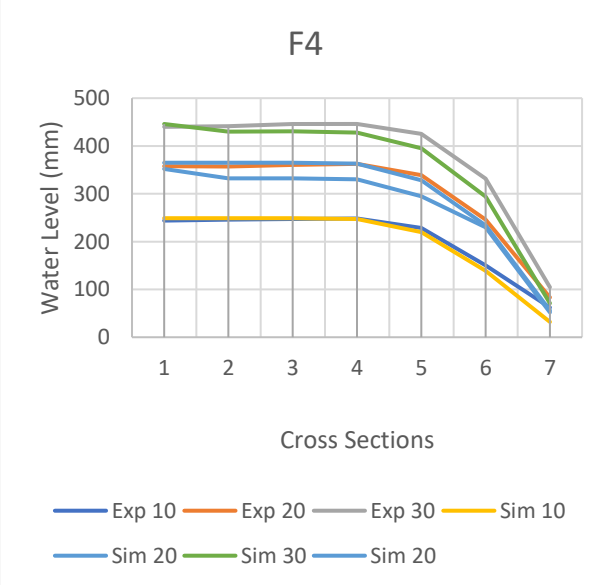

Figure 49: Experimental vs. Simulation data in Parshall flume F4

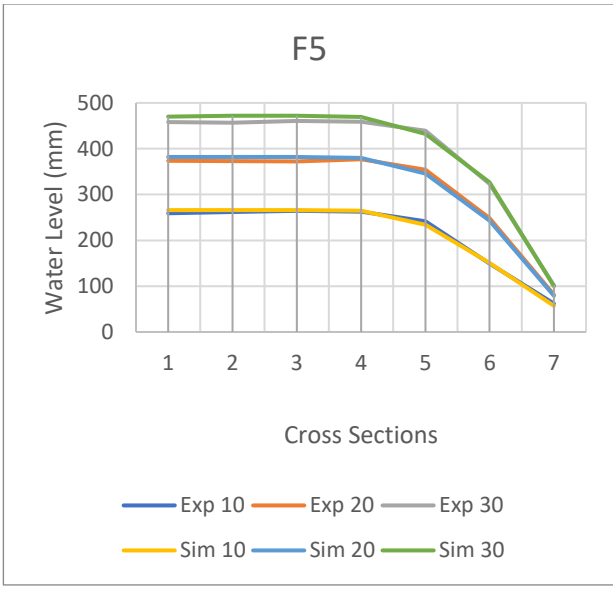

Figure 50: Experimental vs. simulation data in Parshall flume F5

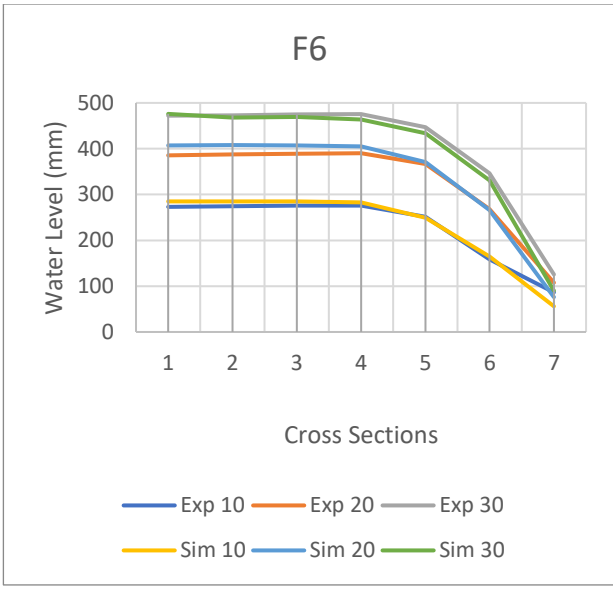

Figure 51: Experimental vs. simulation data in Parshall flume F6

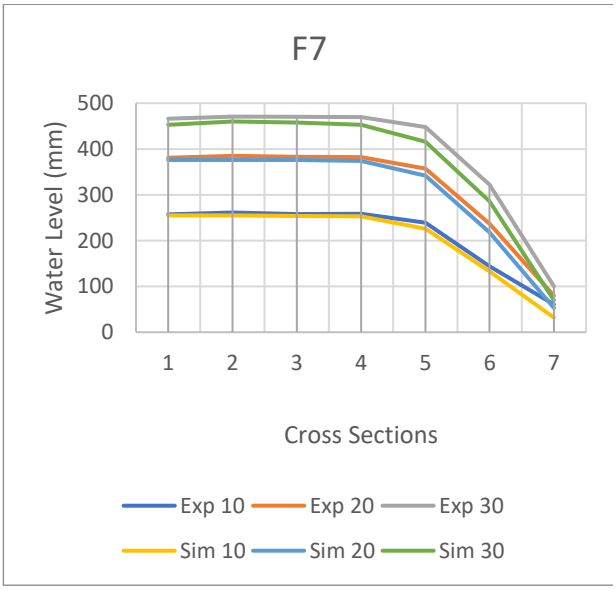

Figure 52: Experimental vs. simulation data in Parshall flume F7

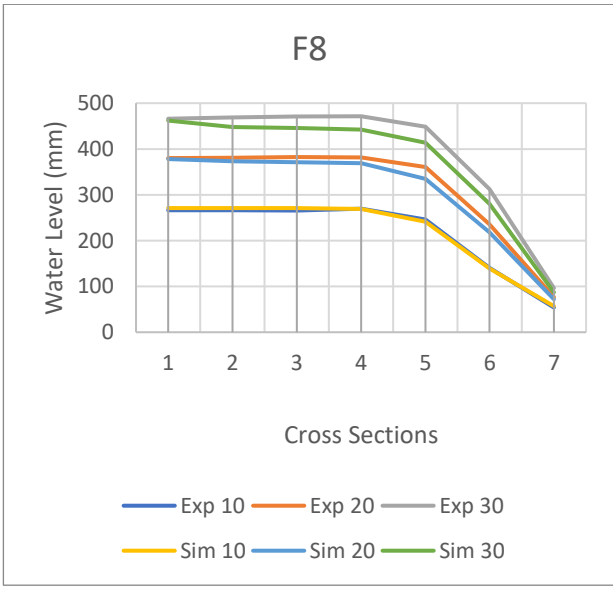

Figure 53: Experimental vs. simulation data in Parshall flume F8

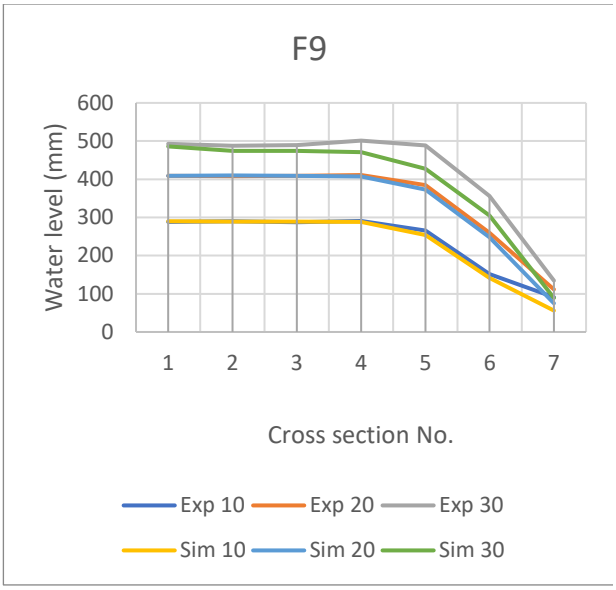

Figure 54: Experimental vs. simulation data in Parshall flume F9

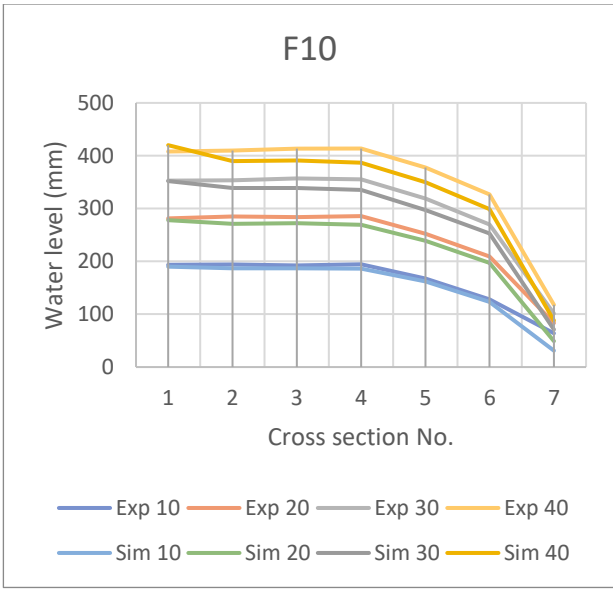

Figure 55: Experimental vs. simulation data in Parshall flume F10

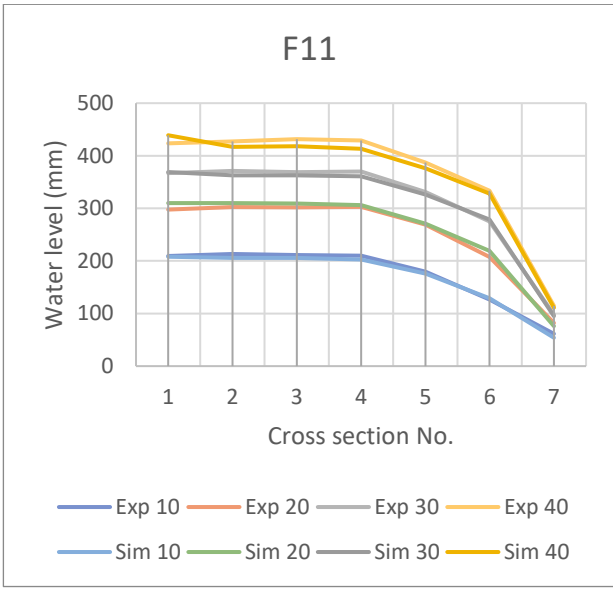

Figure 56: Experimental vs. simulation data in Parshall flume F11

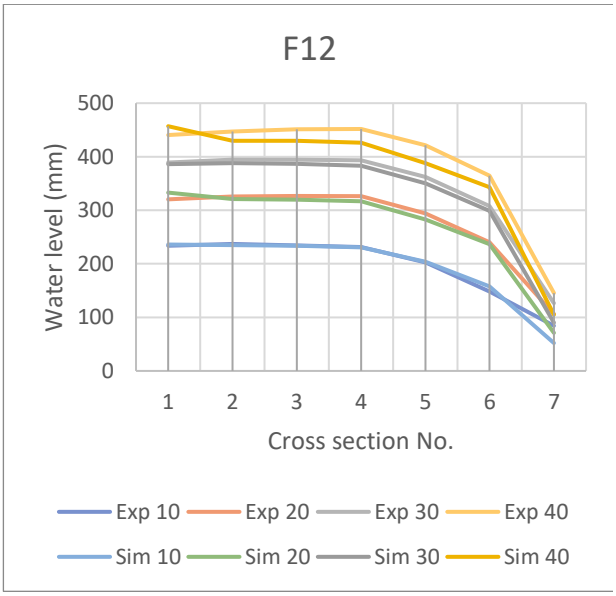

Figure 57: Experimental vs. simulation data in Parshall flume F12

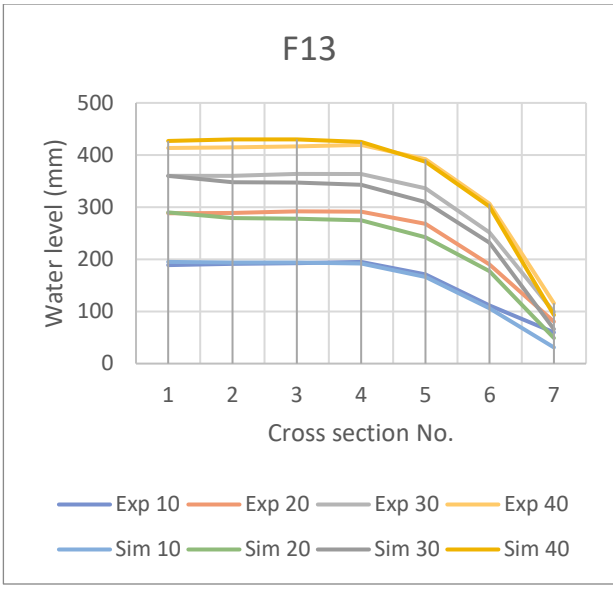

Figure 58: Experimental vs. simulation data in Parshall flume F13

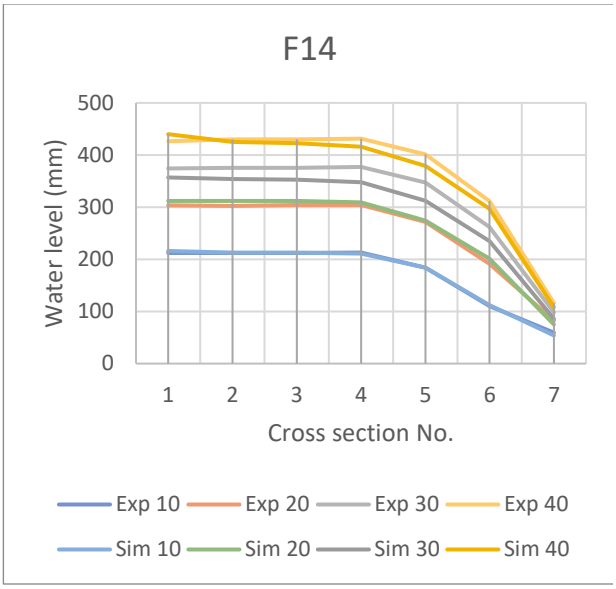

Figure 59: Experimental vs. simulation data in Parshall flume F14

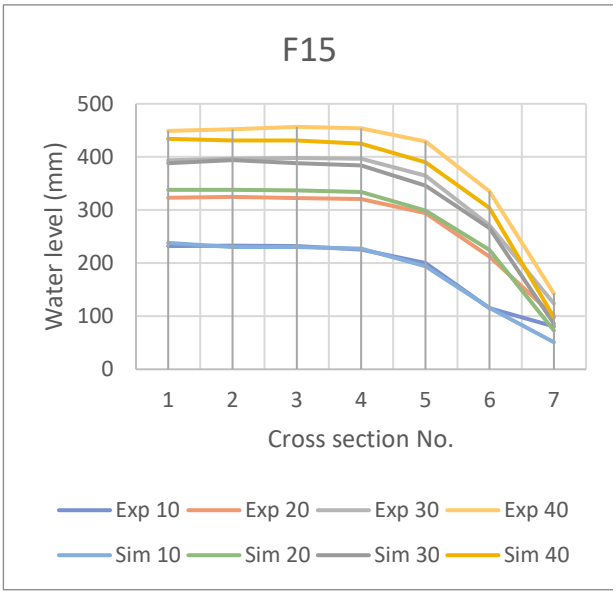

Figure 60: Experimental vs. simulation data in Parshall flume F15

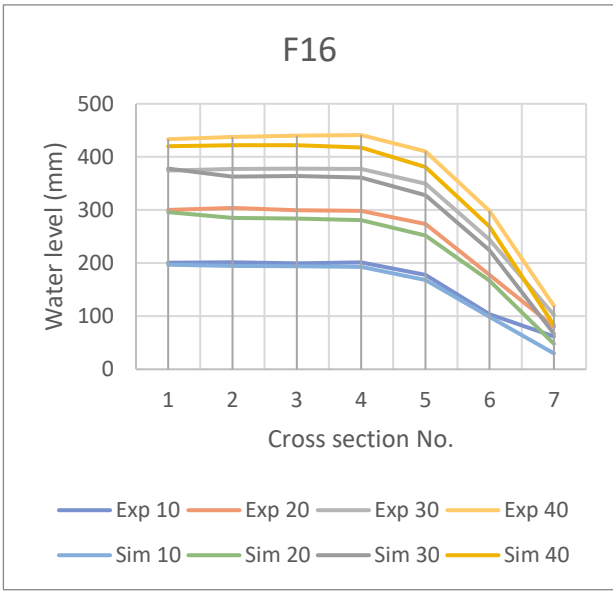

Figure 61: Experimental vs. simulation data in Parshall flume F16

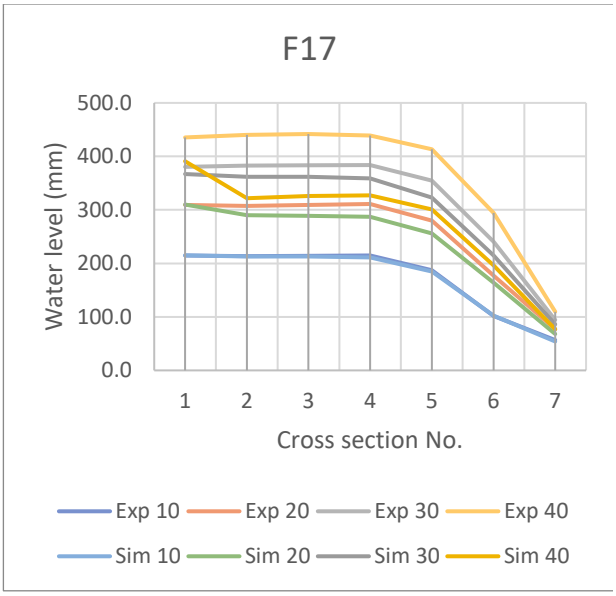

Figure 62: Experimental vs. simulation data in Parshall flume F17

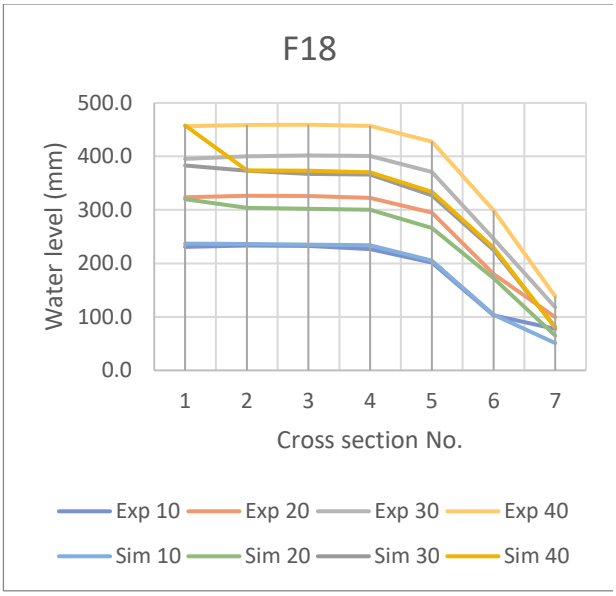

Figure 63: Experimental vs. simulation data in Parshall flume F18

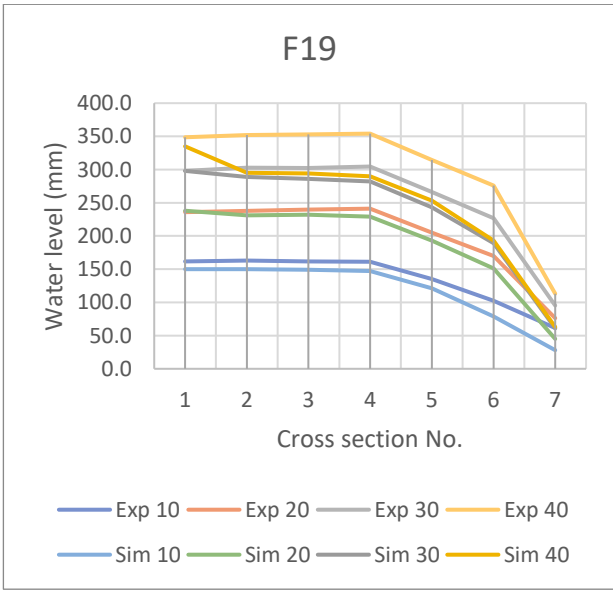

Figure 64: Experimental vs. simulation data in Parshall flume F19

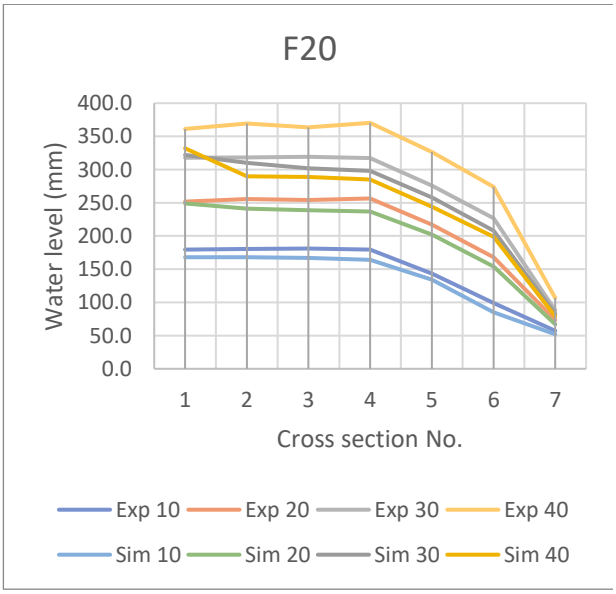

Figure 65: Experimental vs. simulation data in Parshall flume F20

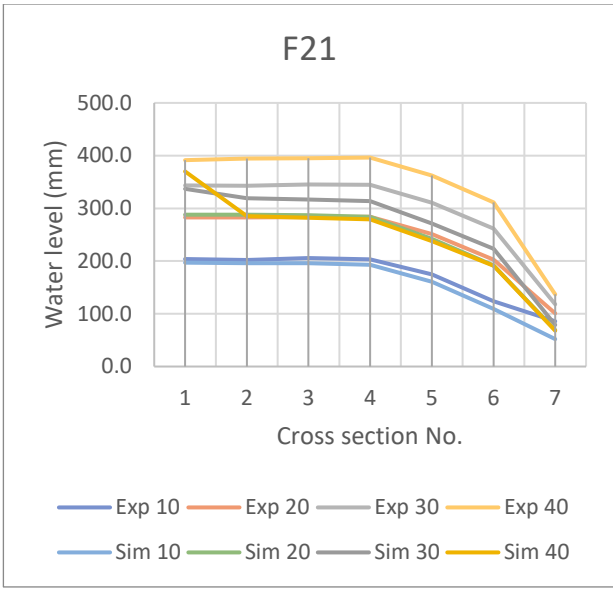

Figure 66: Experimental vs. simulation data in Parshall flume F21

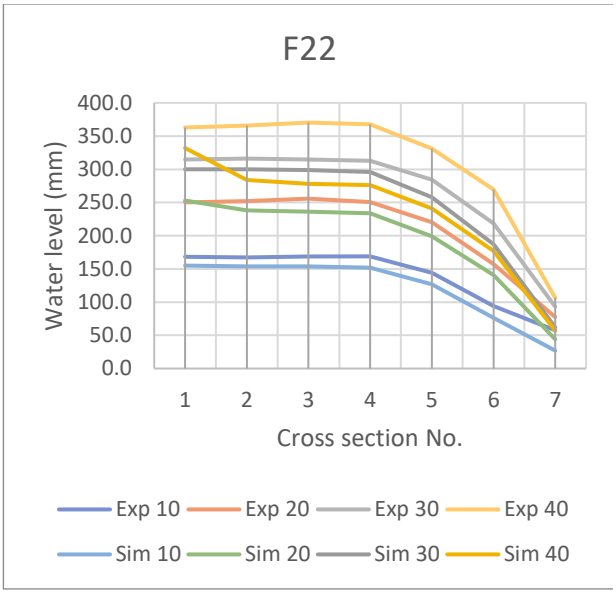

Figure 67: Experimental vs. simulation data in Parshall flume F22

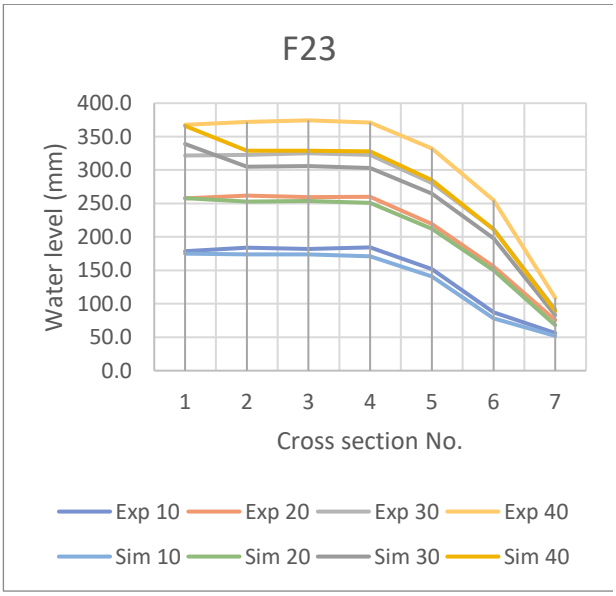

Figure 68: Experimental vs. simulation data in Parshall flume F23

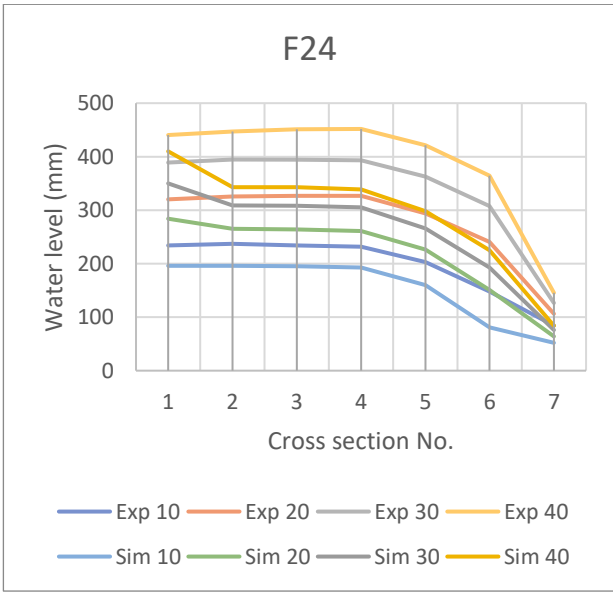

Figure 69: Experimental vs. simulation data in Parshall flume F24

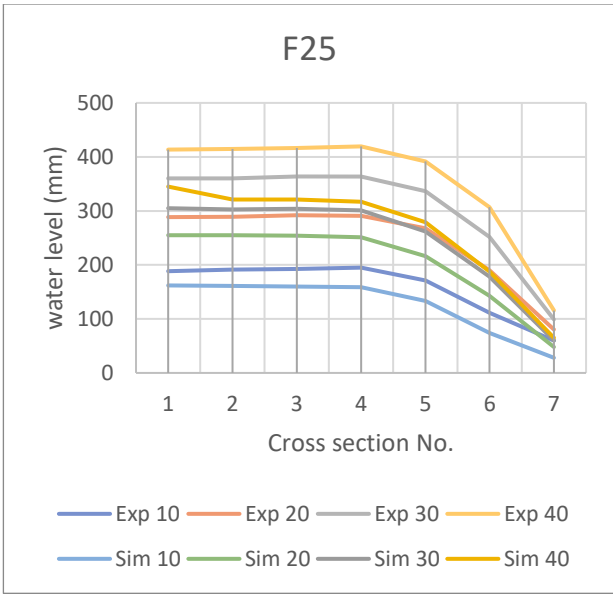

Figure 70: Experimental vs. simulation data in Parshall flume F25

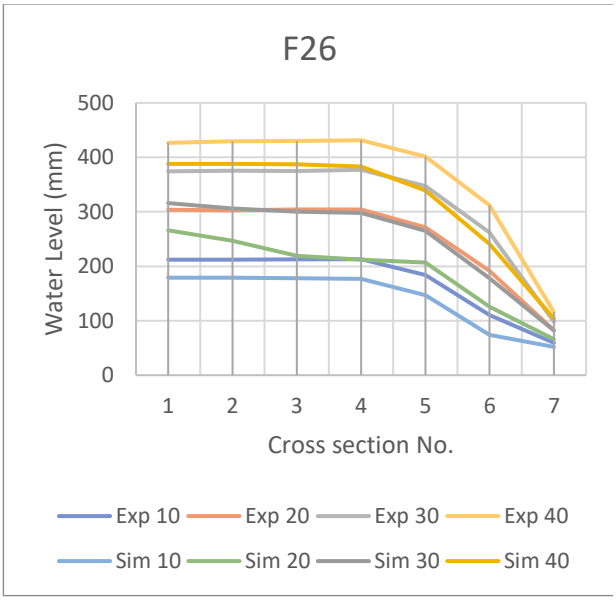

Figure 71: Experimental vs. simulation data in Parshall flume F26

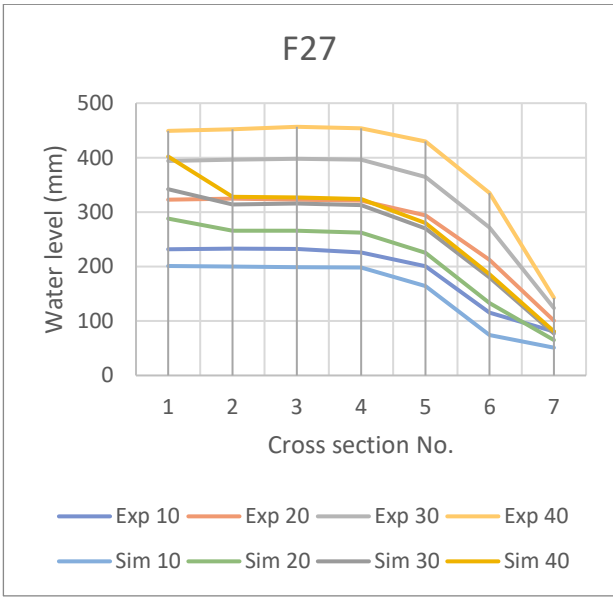

Figure 72: Experimental vs. simulation data in Parshall flume F27

Table 17: Error analysis on water level for flumes #1 to #7 using equation 30

Flume No.	Q (L/s)	Cross-Section No.							Overall error
		1	2	3	4	5	6	7	
	Error (Experimental result vs. Simulation data)								
F1	10	1.03%	0.15%	0.25%	2.28%	7.04%	7.42%	50.41%	**9.80%**
	20	1.46%	4.82%	5.84%	6.13%	10.90%	11.74%	41.24%	**11.73%**
	30	1.55%	2.91%	4.97%	5.71%	7.42%	10.55%	36.35%	**9.92%**
F2									
	10	5.54%	1.10%	1.30%	1.93%	2.83%	3.30%	0.28%	**2.33%**
	20	4.38%	1.36%	0.52%	0.54%	1.99%	2.81%	1.61%	**1.89%**
	30	4.16%	0.26%	0.06%	0.90%	2.54%	3.63%	2.66%	**2.03%**
F3									
	10	2.51%	1.27%	1.93%	1.75%	0.20%	1.85%	32.73%	**6.03%**
	20	1.42%	1.31%	0.89%	0.12%	1.19%	3.96%	29.95%	**5.55%**
	30	0.95%	4.79%	4.71%	4.89%	8.83%	8.20%	25.70%	**8.29%**
F4									
	10	2.01%	1.21%	0.66%	0.55%	3.88%	7.33%	48.54%	**9.17%**
	20	2.11%	2.13%	1.28%	0.10%	3.29%	4.98%	32.71%	**6.66%**
	30	1.33%	2.62%	3.35%	3.99%	7.09%	11.29%	32.07%	**8.82%**
F5									
	10	2.54%	1.48%	0.58%	0.79%	3.04%	1.05%	8.02%	**2.50%**
	20	2.16%	2.42%	2.67%	0.81%	2.22%	2.32%	2.83%	**2.21%**
	30	2.59%	3.27%	2.46%	2.27%	1.64%	1.24%	1.59%	**2.15%**
F6									
	10	4.25%	3.80%	3.32%	2.58%	0.96%	4.25%	35.16%	**7.76%**
	20	5.49%	5.17%	4.67%	3.80%	1.20%	0.89%	29.34%	**7.22%**
	30	0.84%	0.97%	1.19%	2.43%	2.91%	4.53%	28.29%	**5.88%**
F7									
	10	0.90%	2.44%	1.63%	2.19%	5.36%	7.53%	47.29%	**9.62%**
	20	1.36%	2.33%	1.78%	2.13%	4.28%	8.13%	33.58%	**7.66%**
	30	2.84%	2.27%	2.62%	3.57%	7.06%	11.27%	30.26%	**8.56%**

Table 18: Error analysis on water level for flumes #8 to #14 using equation 30

Flume No.	Q (L/s)	Cross-Section No.							Overall
		1	2	3	4	5	6	7	
	Error (Experimental result vs. Simulation data)								
F8	10	1.84%	1.84%	1.91%	0.25%	1.98%	1.29%	5.71%	**2.12%**
	20	0.51%	1.98%	2.99%	3.30%	7.04%	7.38%	6.34%	**4.22%**
	30	0.89%	4.41%	5.25%	6.24%	7.66%	10.40%	9.74%	**6.37%**
F9									
	10	0.49%	0.32%	0.55%	0.93%	4.45%	6.52%	38.58%	**7.41%**
	20	0.02%	0.47%	0.04%	0.99%	3.09%	4.68%	32.68%	**6.00%**
	30	1.44%	2.89%	3.14%	6.03%	12.59%	14.29%	33.86%	**10.61%**
F10									
	10	1.90%	3.62%	2.69%	4.38%	3.12%	4.18%	51.47%	**10.19%**
	20	1.25%	4.94%	4.14%	5.86%	5.33%	5.76%	41.08%	**9.76%**
	30	0.19%	4.04%	5.06%	5.77%	6.84%	6.15%	29.87%	**8.27%**
	40	2.98%	4.82%	5.40%	6.44%	7.30%	8.58%	25.28%	**8.69%**
F11									
	10	0.66%	3.40%	2.50%	3.20%	2.06%	1.83%	12.12%	**3.68%**
	20	4.21%	2.49%	2.44%	1.05%	0.84%	5.48%	7.41%	**3.42%**
	30	0.48%	2.21%	1.64%	2.50%	1.46%	1.39%	3.00%	**1.81%**
	40	3.66%	2.33%	3.16%	3.78%	2.80%	1.57%	3.18%	**2.93%**
F12									
	10	0.90%	0.89%	0.04%	0.27%	0.58%	6.74%	38.30%	**6.82%**
	20	3.95%	1.40%	2.07%	2.93%	3.74%	1.43%	33.17%	**6.96%**
	30	0.77%	1.67%	1.84%	2.59%	3.43%	2.78%	28.82%	**5.99%**
	40	3.78%	3.83%	4.67%	5.71%	7.86%	5.93%	27.84%	**8.52%**
F13									
	10	3.36%	1.32%	0.67%	1.54%	3.08%	4.98%	48.25%	**9.03%**
	20	0.55%	3.52%	4.79%	5.55%	9.65%	6.85%	39.09%	**10.00%**
	30	0.06%	3.33%	4.55%	5.66%	7.80%	7.76%	33.37%	**8.94%**
	40	3.21%	3.63%	3.19%	1.33%	1.22%	1.86%	19.63%	**4.87%**
F14									
	10	1.69%	0.28%	0.26%	0.92%	0.04%	1.63%	9.06%	**1.98%**
	20	2.78%	3.12%	2.56%	1.57%	0.86%	5.04%	9.09%	**3.58%**
	30	4.66%	5.73%	5.90%	7.72%	10.17%	10.24%	12.40%	**8.12%**
	40	3.21%	1.11%	1.62%	3.57%	5.54%	4.72%	6.83%	**3.80%**

Table 19: Error analysis on water level for flumes #15 to #20 using equation 30

Flume No.	Q (L/s)	Cross-Section No.							Overall
		1	2	3	4	5	6	7	
	Error (Experimental result vs. Simulation data)								
F15	10	2.64%	1.25%	0.90%	0.63%	3.14%	0.67%	36.80%	**6.58%**
	20	4.62%	4.10%	4.47%	4.14%	1.75%	5.97%	27.44%	**7.50%**
	30	1.46%	0.60%	2.48%	3.13%	5.04%	2.01%	30.50%	**6.46%**
	40	3.38%	4.68%	5.61%	6.35%	9.19%	9.26%	31.30%	**9.97%**
F16									
	10	1.83%	3.25%	2.83%	4.10%	5.37%	4.42%	51.46%	**10.47%**
	20	1.41%	6.22%	5.18%	5.89%	7.95%	5.96%	40.13%	**10.39%**
	30	1.03%	3.82%	3.67%	4.34%	6.18%	8.21%	34.72%	**8.85%**
	40	3.13%	3.56%	4.07%	5.26%	7.22%	9.80%	30.53%	**9.08%**
F17									
	10	0.17%	0.33%	0.59%	1.77%	1.10%	0.29%	4.68%	**1.28%**
	20	0.19%	5.76%	6.63%	7.72%	8.63%	7.41%	11.62%	**6.85%**
	30	3.54%	5.45%	5.56%	6.46%	9.01%	10.48%	8.77%	**7.04%**
	40	10.19%	26.82%	26.21%	25.51%	27.14%	33.45%	29.81%	**25.59%**
F18									
	10	2.57%	1.11%	0.89%	3.20%	1.66%	0.99%	34.24%	**6.38%**
	20	1.10%	6.86%	7.39%	6.96%	9.78%	4.43%	34.66%	**10.17%**
	30	3.15%	6.84%	20.35%	8.69%	11.76%	8.58%	31.37%	**12.96%**
	40	0.31%	18.49%	18.78%	19.02%	21.94%	23.49%	42.18%	**20.60%**
F19									
	10	7.09%	7.97%	7.95%	8.74%	10.41%	22.78%	54.38%	**17.05%**
	20	0.81%	2.95%	3.13%	5.04%	5.90%	11.11%	40.97%	**9.99%**
	30	0.02%	4.60%	5.39%	7.41%	8.75%	16.59%	35.98%	**11.25%**
	40	3.95%	16.19%	16.68%	18.11%	19.59%	29.98%	44.30%	**21.26%**
F20									
	10	6.47%	6.80%	7.79%	8.65%	6.61%	14.09%	9.20%	**8.52%**
	20	1.15%	5.66%	5.92%	7.60%	6.90%	8.36%	8.91%	**6.35%**
	30	1.35%	2.65%	5.40%	6.03%	6.45%	8.32%	5.63%	**5.12%**
	40	8.08%	21.46%	20.47%	23.05%	25.22%	27.32%	25.97%	**21.65%**

Table 20: Error analysis on water level for flumes #21 to #27 using equation 30

Flume No.	Q (L/s)	Cross-Section No.							Overall
		1	2	3	4	5	6	7	
	Error (Experimental result vs. Simulation data)								
F21	10	3.37%	2.97%	4.73%	5.11%	7.84%	11.78%	39.41%	**10.75%**
	20	1.87%	1.85%	1.22%	0.04%	3.62%	5.12%	31.53%	**6.46%**
	30	1.93%	6.98%	8.19%	8.97%	12.84%	14.69%	33.06%	**12.38%**
	40	5.53%	27.78%	28.58%	29.60%	34.35%	38.60%	50.31%	**30.68%**
F22									
	10	7.82%	8.00%	8.65%	10.00%	11.84%	19.06%	53.15%	**16.93%**
	20	1.19%	5.64%	7.76%	6.62%	9.68%	10.24%	43.21%	**12.05%**
	30	4.67%	5.10%	4.94%	5.39%	9.25%	14.30%	33.48%	**11.02%**
	40	8.52%	22.36%	24.94%	24.91%	27.18%	34.28%	46.46%	**26.95%**
F23									
	10	2.15%	5.33%	4.31%	7.25%	7.05%	10.61%	7.47%	**6.31%**
	20	0.10%	3.36%	2.16%	3.42%	3.32%	3.63%	10.11%	**3.73%**
	30	5.44%	5.42%	5.88%	6.13%	5.57%	6.56%	9.09%	**6.30%**
	40	0.42%	11.60%	12.10%	11.65%	14.27%	17.13%	18.27%	**12.21%**
F24									
	10	16.20%	17.33%	16.70%	16.67%	21.11%	45.28%	38.30%	**24.51%**
	20	11.35%	18.60%	19.21%	20.08%	23.13%	37.20%	39.76%	**24.19%**
	30	10.03%	21.69%	21.88%	22.43%	26.61%	37.25%	39.89%	**25.68%**
	40	6.89%	23.29%	23.96%	24.97%	29.23%	38.29%	42.27%	**26.99%**
F25									
	10	14.13%	15.92%	16.97%	18.46%	22.35%	33.66%	53.26%	**24.96%**
	20	11.58%	11.82%	13.01%	13.79%	19.36%	24.74%	40.33%	**19.23%**
	30	15.33%	15.83%	16.38%	17.21%	22.08%	29.23%	39.42%	**22.21%**
	40	16.61%	22.64%	22.96%	24.42%	28.78%	38.70%	43.83%	**28.28%**
F26									
	10	15.73%	15.73%	16.22%	16.89%	20.07%	32.85%	12.43%	**18.56%**
	20	12.37%	18.36%	28.01%	30.31%	23.80%	34.16%	20.00%	**23.86%**
	30	15.61%	18.51%	20.03%	20.98%	23.70%	32.01%	16.47%	**21.05%**
	40	8.99%	9.72%	9.99%	11.22%	15.51%	22.69%	10.28%	**12.63%**
F27	10	13.31%	14.13%	14.26%	12.23%	18.11%	35.78%	36.80%	**20.66%**
	20	10.85%	18.07%	17.54%	18.31%	23.43%	37.36%	35.39%	**23.00%**
	30	13.15%	20.78%	20.57%	21.04%	25.90%	33.69%	37.77%	**24.70%**
	40	10.50%	27.46%	28.39%	28.61%	34.80%	44.48%	43.21%	**31.07%**

Table 21: Experimental vs. simulated water level data using three non-linear turbulence models

Flume No.	Turbulence Model	Source	Q (L/s)	Water level @ each cross-section (mm)						
				1	2	3	4	5	6	7
F1	$v^2 - f$	Experimental	**10**	240	242	243	247	224	163	67
			20	347	349	353	352	331	261	89
			30	423	425	434	433	403	341	115
		Simulation	**10**	255	255	255	254	225	165	57
			20	369	369	369	366	332	269	81
			30	410	410	408	406	367	303	90
F1	Lien Cubic	Experimental	**10**	240	242	243	247	224	163	67
			20	347	349	353	352	331	261	89
			30	423	425	434	433	403	341	115
		Simulation	**10**	240	240	240	238	210	151	55
			20	352	348	344	344	309	244	77
			30	406	393	393	393	359	292	90
F1	Shih Quadratic	Experimental	**10**	240	242	243	247	224	163	67
			20	347	349	353	352	331	261	89
			30	423	425	434	433	403	341	115
		Simulation	**10**	241	240	240	238	211	150	54
			20	371	370	370	367	334	270	81
			30	423	423	416	413	379	313	93
F5	$v^2 - f$	Experimental	**10**	259	262	264	263	241	149	62
			20	374	373	372	377	354	249	81
			30	458	457	461	459	439	323	102
		Simulation	**10**	259	259	258	257	229	142	56
			20	375	375	375	373	340	241	79
			30	427	427	427	424	389	288	91
F5	Lien Cubic	Experimental	**10**	259	262	264	263	241	149	62
			20	374	373	372	377	354	249	81
			30	458	457	461	459	439	323	102
		Simulation	**10**	266	266	266	265	238	151	58
			20	385	385	385	383	353	254	80
			30	428	427	427	427	402	302	91
F5	Shih Quadratic	Experimental	**10**	259	262	264	263	241	149	62
			20	374	373	372	377	354	249	81
			30	458	457	461	459	439	323	102
		Simulation	**10**	256	255	255	253	225	137	55
			20	353	349	350	347	316	220	71
			30	433	435	430	429	393	291	90

Table 22: Error analysis on three non-linear turbulence models' data vs. experimental results

Flume No.	Turbulence Model	Q (L/s)	Cross-Section No.							Overall
			1	2	3	4	5	6	7	
			Error (Experimental result vs. Simulation data)							
F1	$v^2 - f$	10	6.45%	5.21%	5.11%	2.99%	0.56%	1.16%	14.34%	**5.12%**
		20	6.36%	5.79%	4.65%	4.11%	0.27%	3.22%	8.47%	**4.70%**
		30	3.17%	3.61%	5.90%	6.17%	8.91%	11.14%	21.53%	**8.63%**
F1	Lien Cubic									
		10	0.19%	0.98%	1.07%	3.50%	6.15%	7.42%	17.34%	**5.24%**
		20	1.46%	0.23%	2.44%	2.15%	6.67%	6.37%	12.99%	**4.62%**
		30	4.12%	7.61%	9.36%	9.18%	10.89%	14.37%	21.53%	**11.01%**
F1	Shih Quadratic									
		10	0.61%	0.98%	1.07%	3.50%	5.70%	8.03%	18.85%	**5.53%**
		20	6.93%	6.08%	4.93%	4.39%	0.88%	3.61%	8.47%	**5.04%**
		30	0.10%	0.55%	4.05%	4.56%	5.93%	8.21%	18.91%	**6.05%**
F5	$v^2 - f$									
		10	0.16%	1.19%	2.44%	2.25%	5.11%	4.97%	9.63%	**3.68%**
		20	0.29%	0.55%	0.79%	1.05%	3.92%	3.13%	2.83%	**1.79%**
		30	6.80%	6.57%	7.31%	7.54%	11.43%	10.84%	10.45%	**8.71%**
F5	Lien Cubic									
		10	2.54%	1.48%	0.58%	0.79%	1.38%	1.05%	6.41%	**2.03%**
		20	2.97%	3.23%	3.48%	1.60%	0.25%	2.10%	1.60%	**2.17%**
		30	6.58%	6.57%	7.31%	6.89%	8.47%	6.50%	10.45%	**7.54%**
F5	Shih Quadratic									
		10	1.31%	2.72%	3.58%	3.77%	6.77%	8.32%	11.25%	**5.39%**
		20	5.59%	6.42%	5.93%	7.95%	10.70%	11.57%	12.67%	**8.69%**
		30	5.49%	4.82%	6.66%	6.45%	10.52%	9.91%	11.43%	**7.90%**

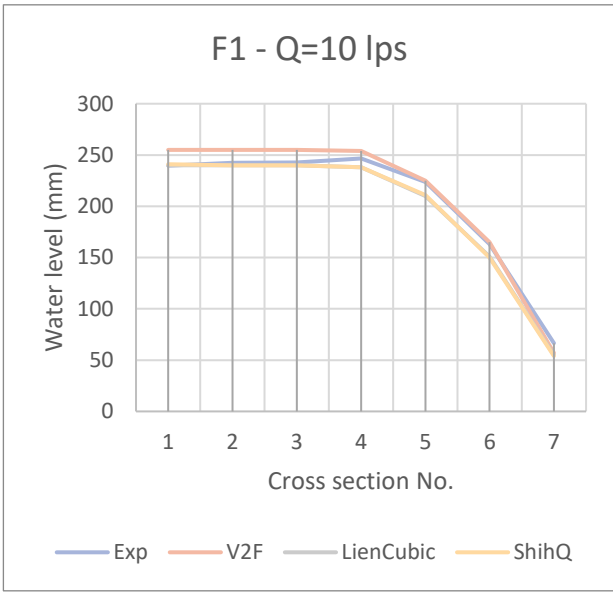

Figure 73: Experimental vs. simulation data in Parshall flume F1 - 10 l/s

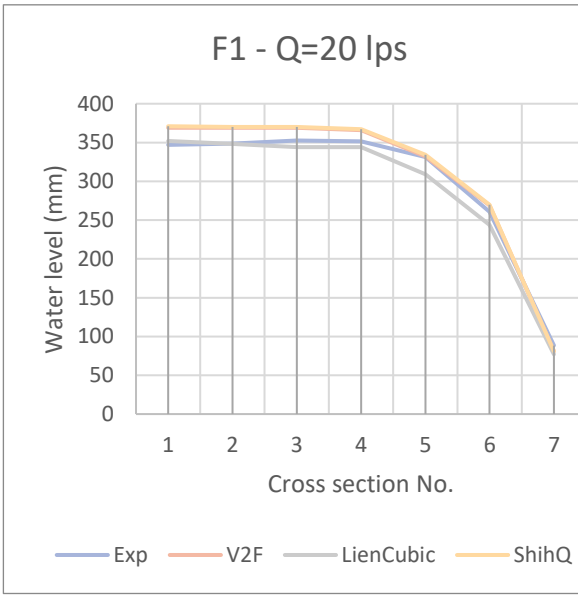

Figure 74: Experimental vs. simulation data in Parshall flume F1 - 20 l/s

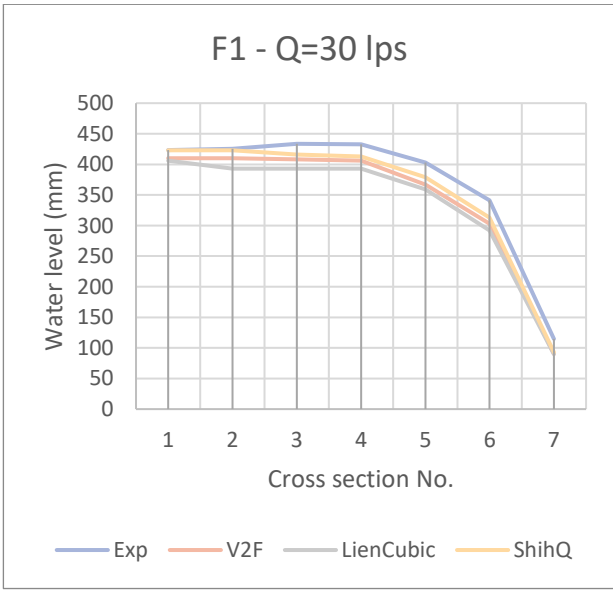

Figure 75: Experimental vs. simulation data in Parshall flume F1 - 30 l/s

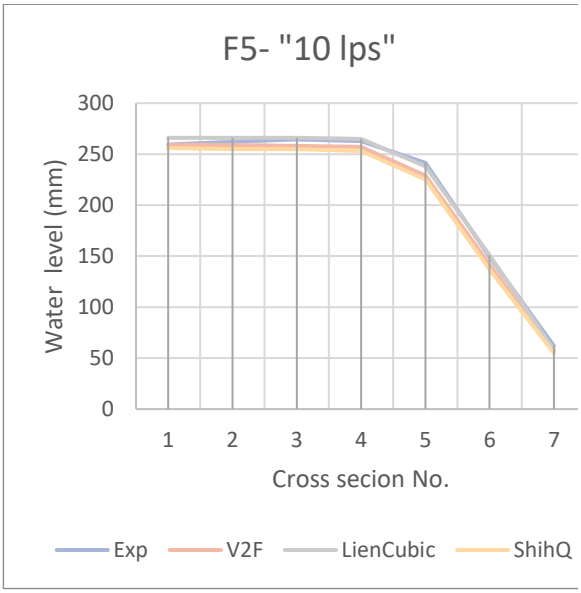

Figure 76: Experimental vs. simulation data in Parshall flume F5 - 10 l/s

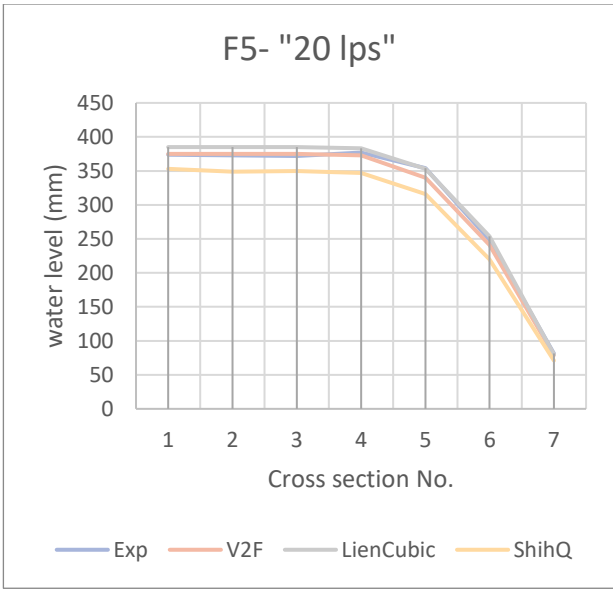

Figure 77: Experimental vs. simulation data in Parshall flume F5 - 20 l/s

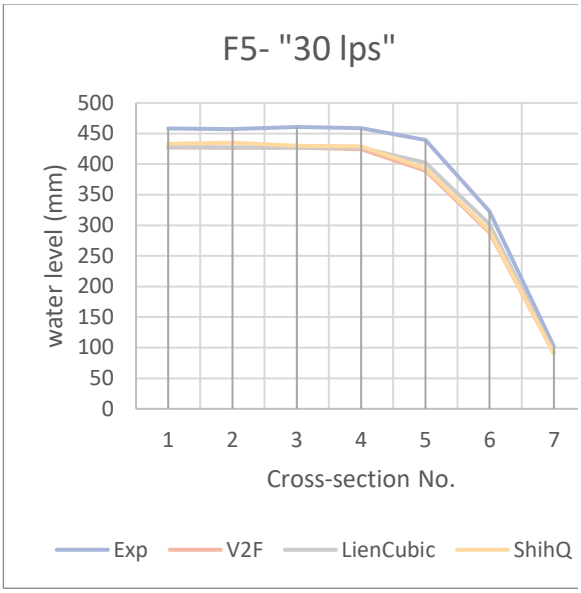

Figure 78: Experimental vs. simulation data in Parshall flume F5 - 30 l/s

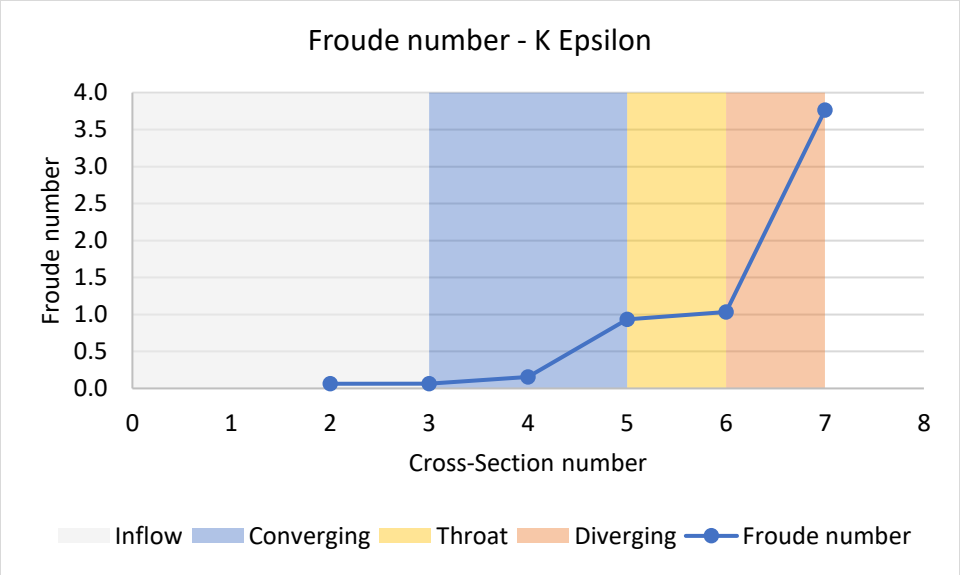

Figure 79: Froud number graph for K Epsilon turbulence model

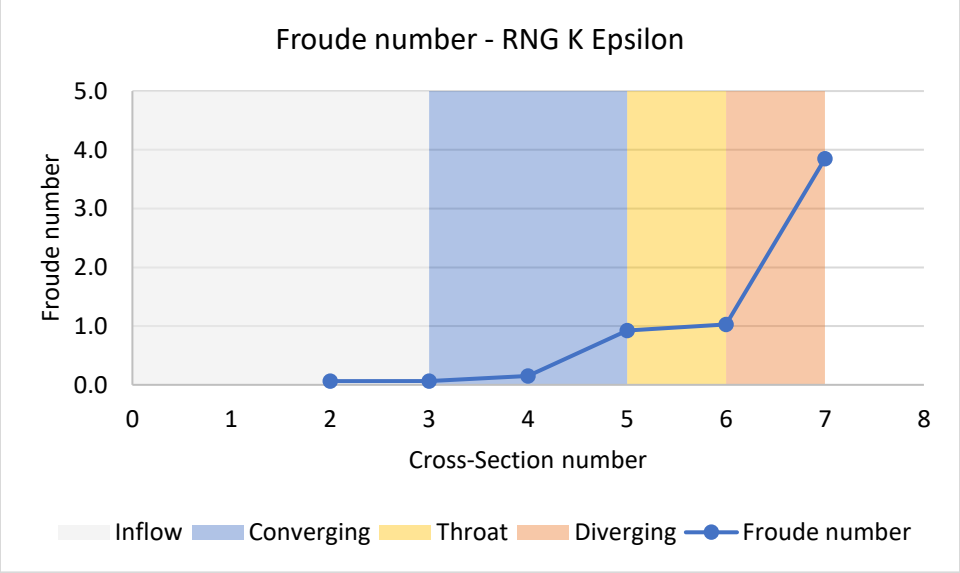

Figure 80: Froud number graph for RNG K Epsilon turbulence model

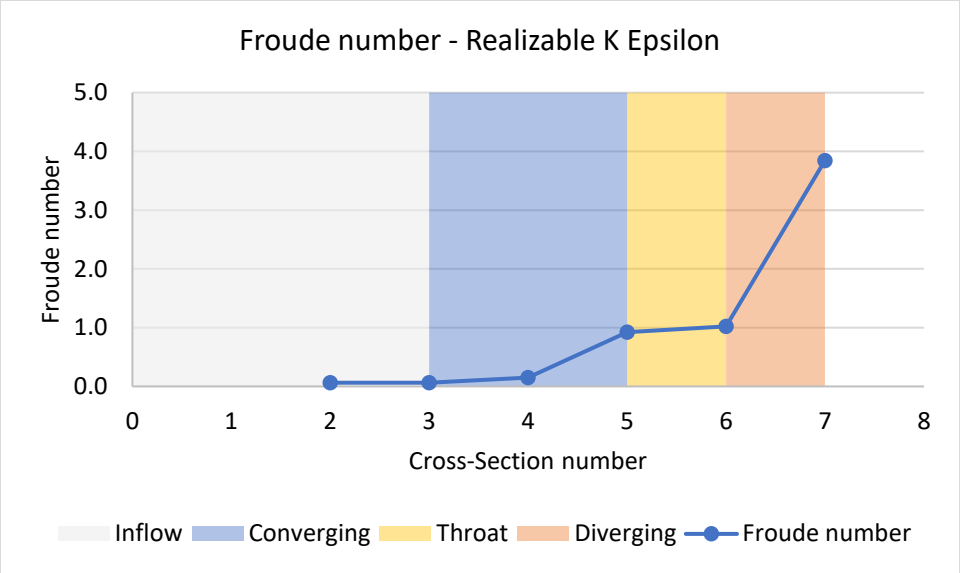

Figure 81: Froud number graph for Realizable K Epsilon turbulence model

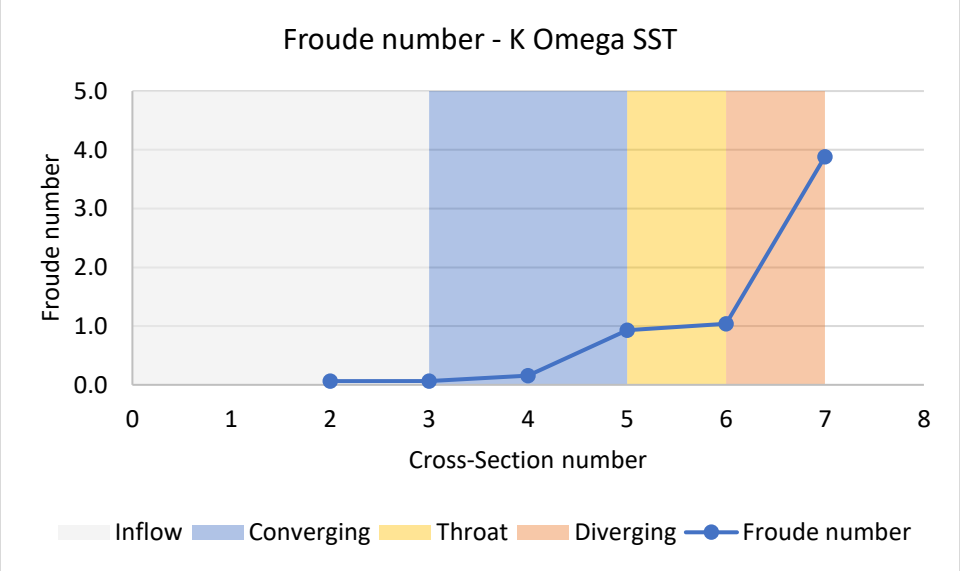

Figure 82: Froud number graph for K Omega SST turbulence model

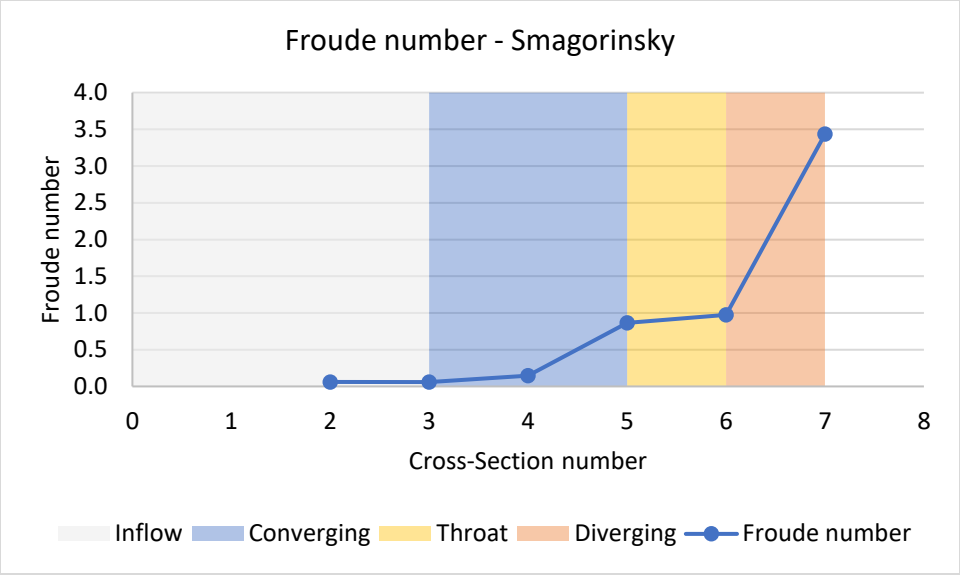

Figure 83: Froud number graph for Smagorinsky turbulence model (LES)

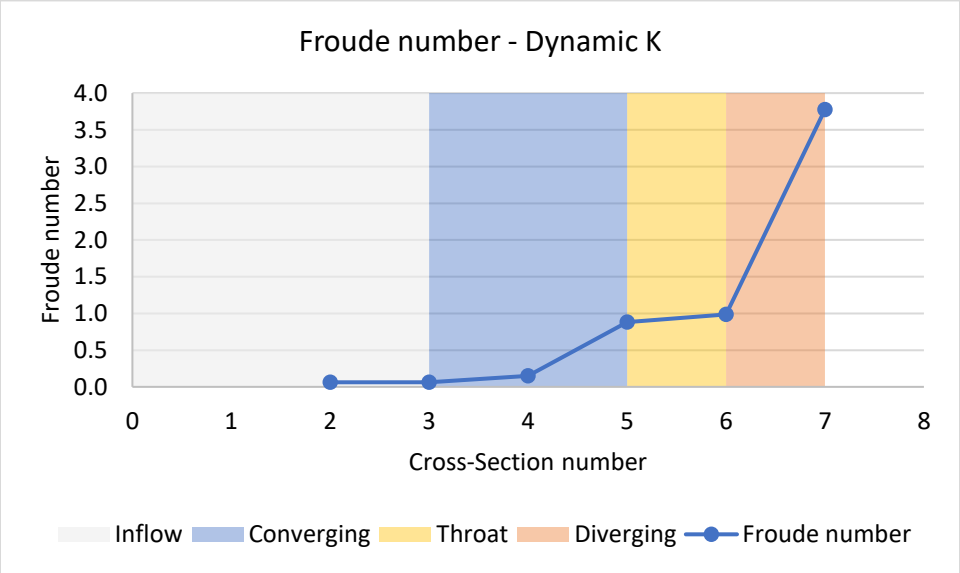

Figure 84: Froud number graph for Dynamic K eq turbulence model (LES)

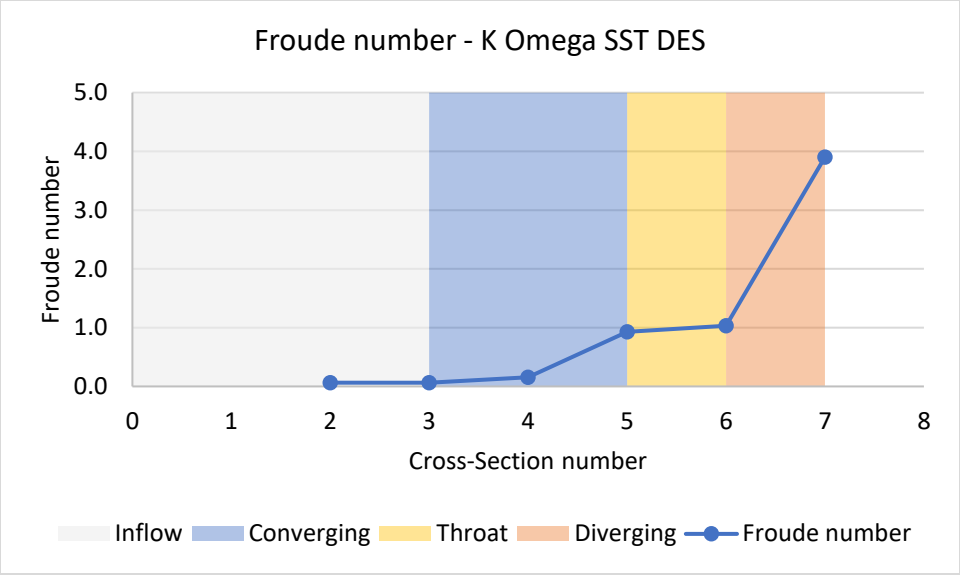

Figure 85: Froud number graph for K Omega SST DES turbulence model (DES)

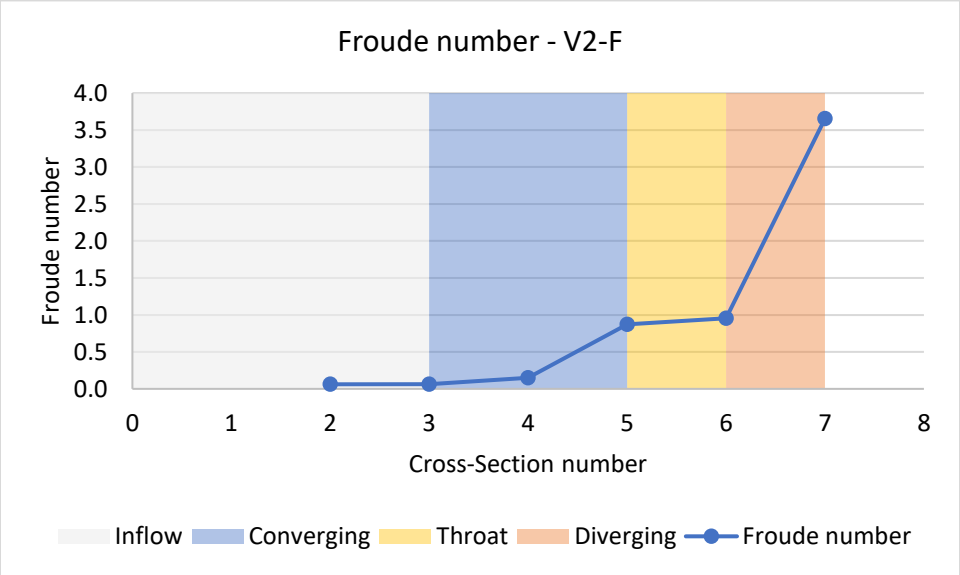

Figure 86: Froud number graph for non-linear $v^2 - f$ turbulence model

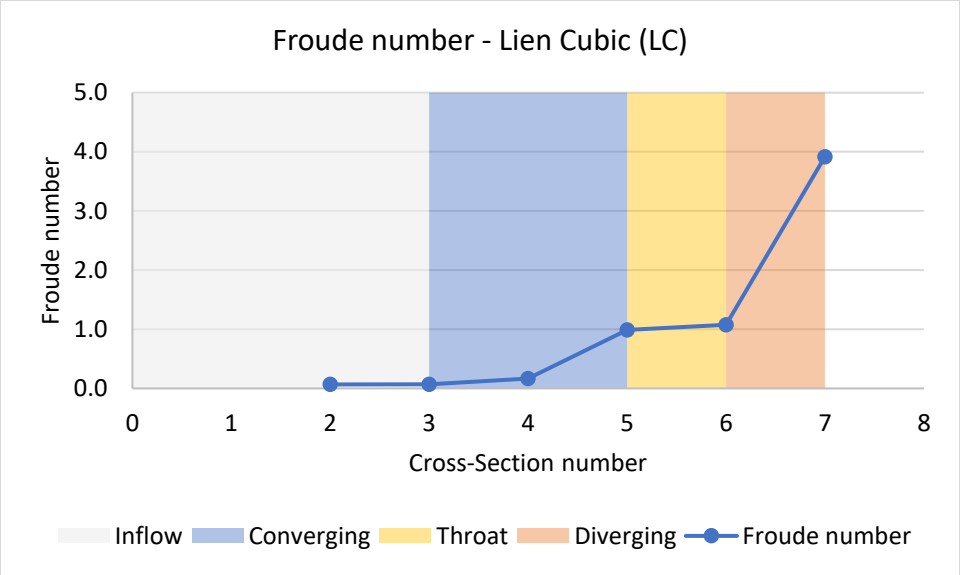

Figure 87: Froud number graph for non-linear Lien Cubic (LC) turbulence model

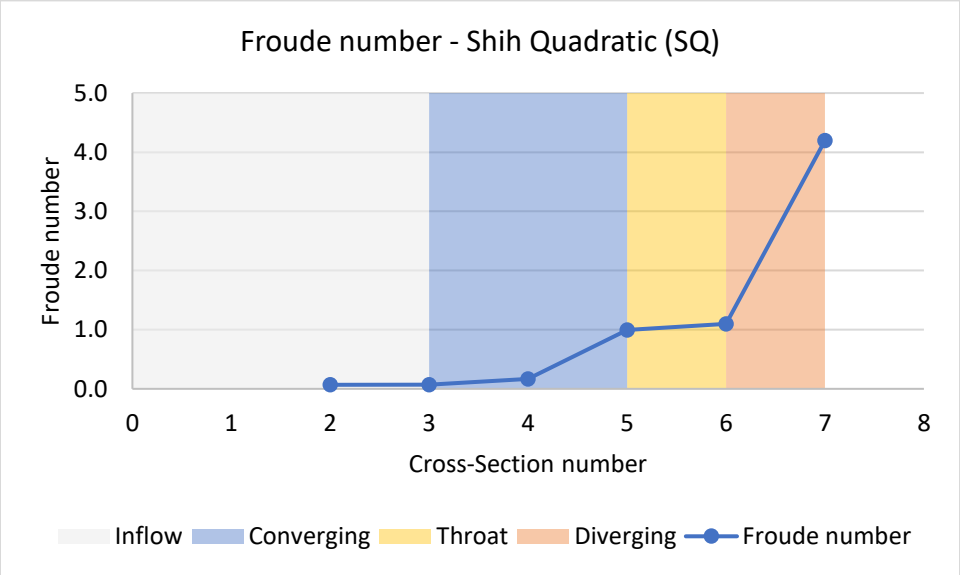

Figure 88: Froud number graph for non-linear Shih Quadratic (SQ) turbulence model

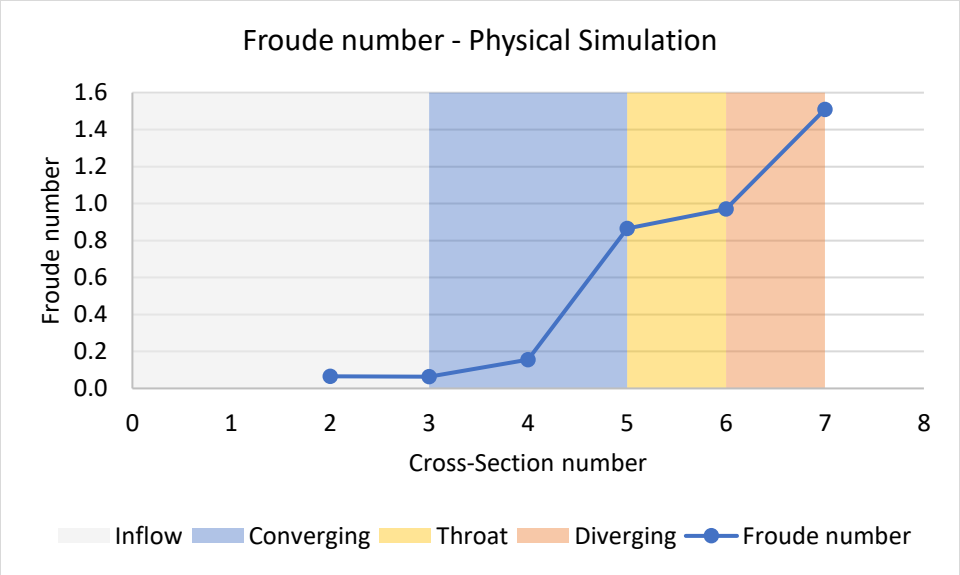

Figure 89: Froud number graph for Physical Simulation

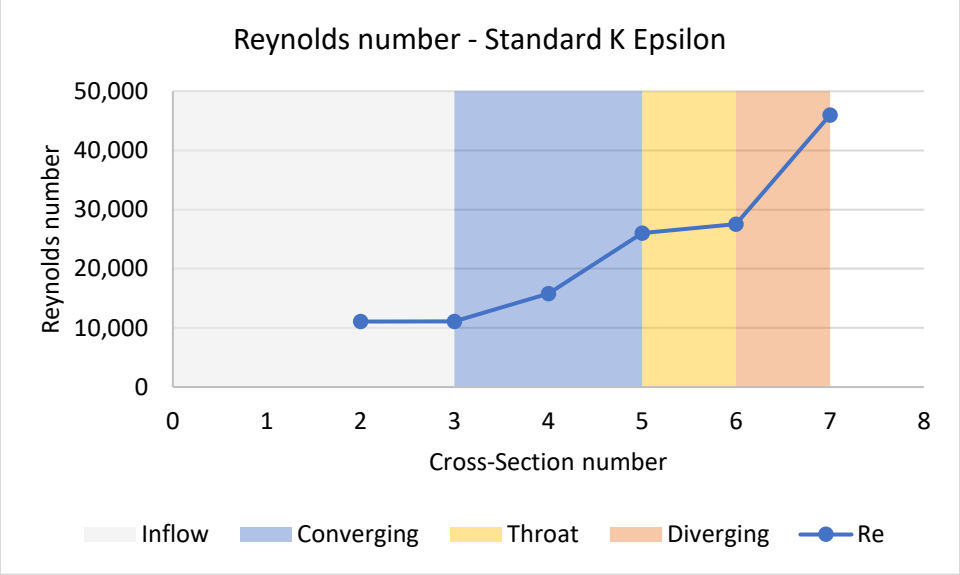

Figure 90: Reynolds number graph for Standard $k-\varepsilon$ turbulence model (RANS)

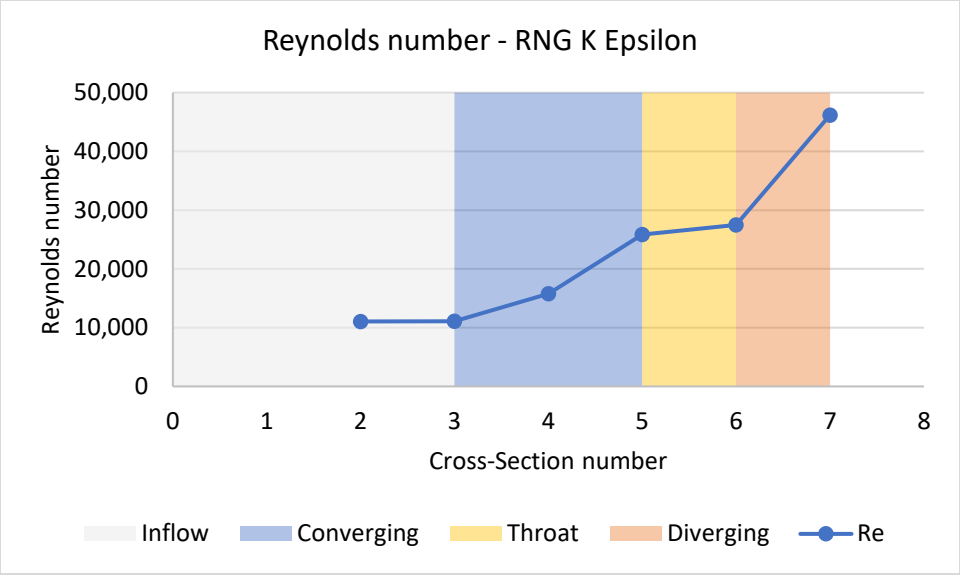

Figure 91: Reynolds number graph for RNG $k - \varepsilon$ turbulence model (RANS)

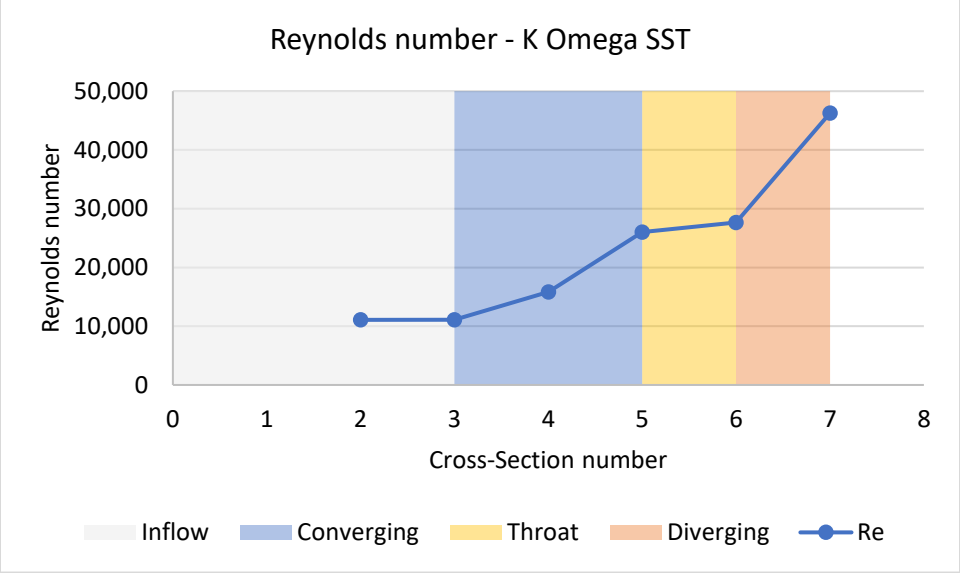

Figure 92: Reynolds number graph for RNG k epsilon turbulence model (RANS)

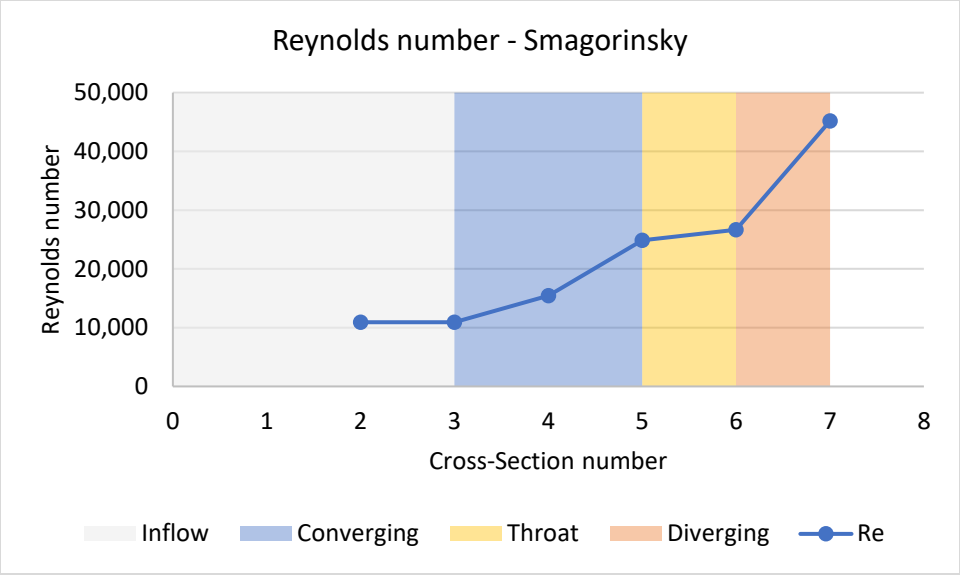

Figure 93: Reynolds number graph for Smagorinsky turbulence model (LES)

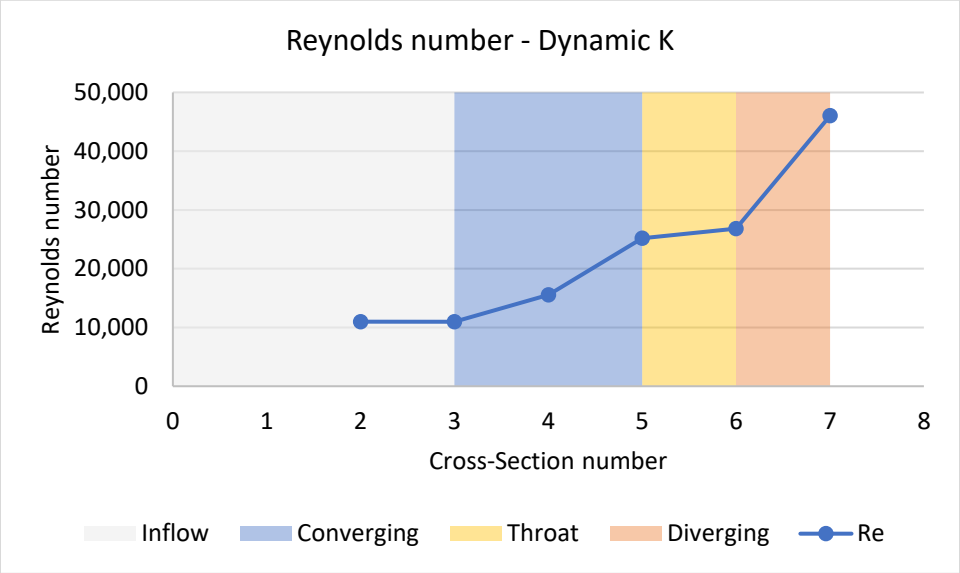

Figure 94: Reynolds number graph for Dynamic k eq turbulence model (LES)

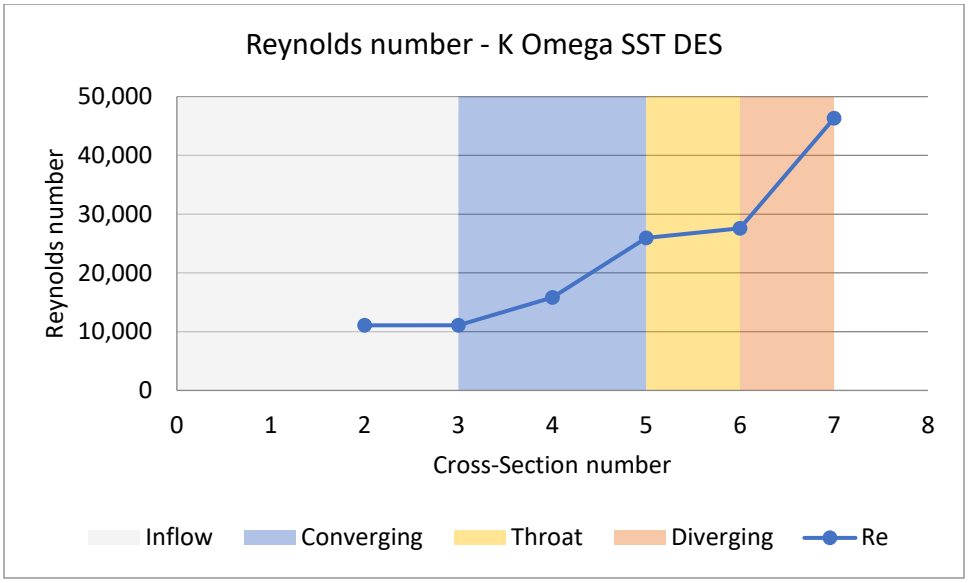

Figure 95: Reynolds number graph for $k-\omega\ SST\ DES$ turbulence model (DES)

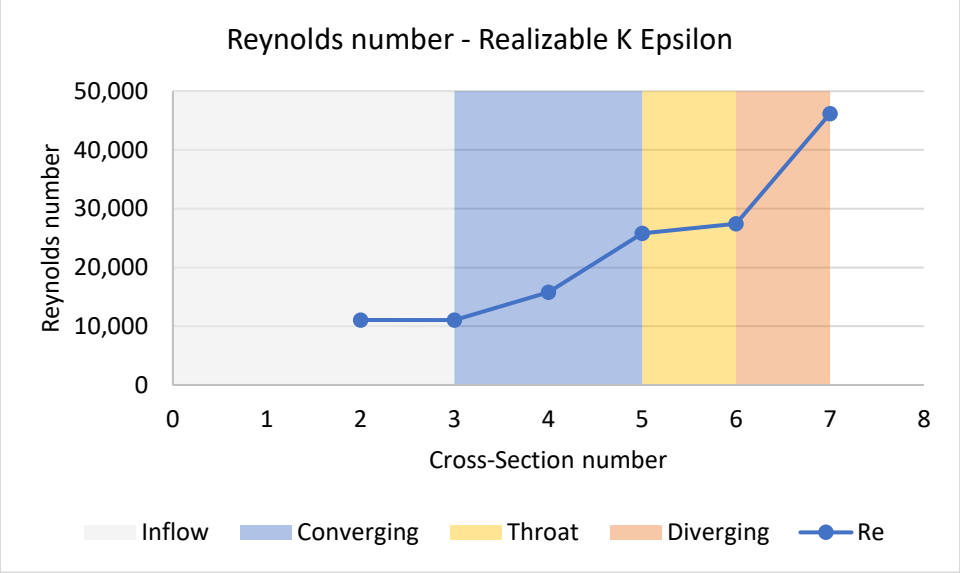

Figure 96: Reynolds number graph for Realizable $k-\varepsilon$ turbulence model (RANS)

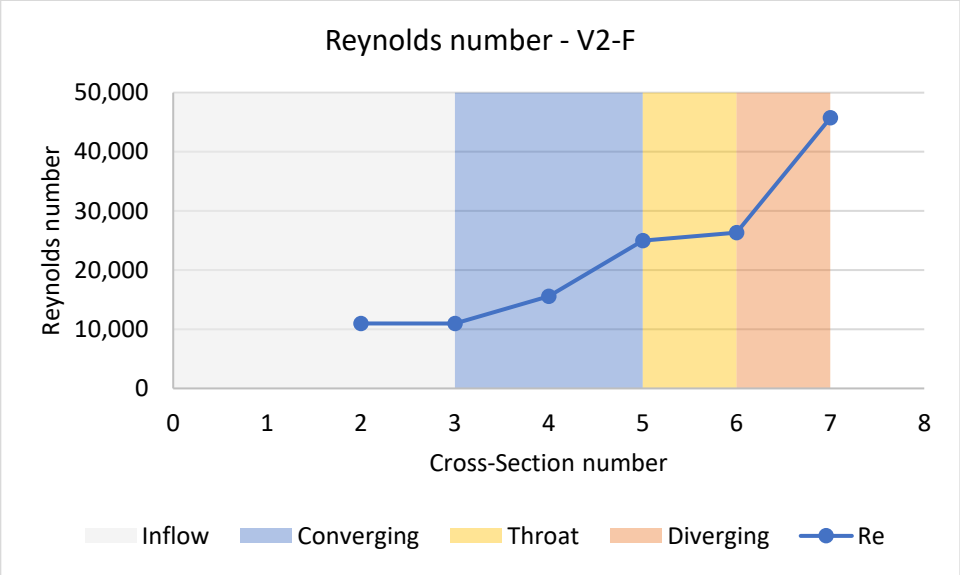

Figure 97: Reynolds number graph for $v^2 - f$ non-linear turbulence model

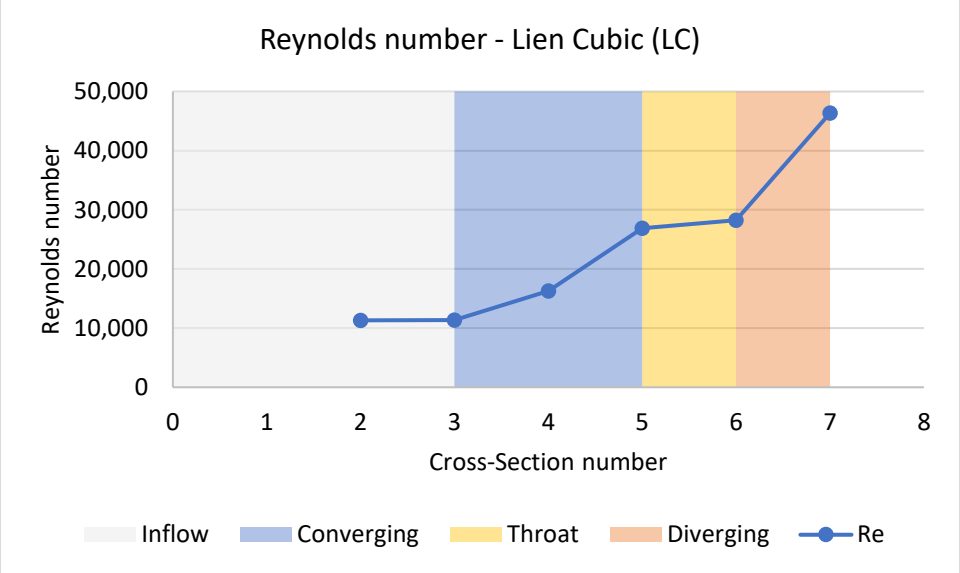

Figure 98: Reynolds number graph for Lien Cubic (LC) non-linear turbulence model

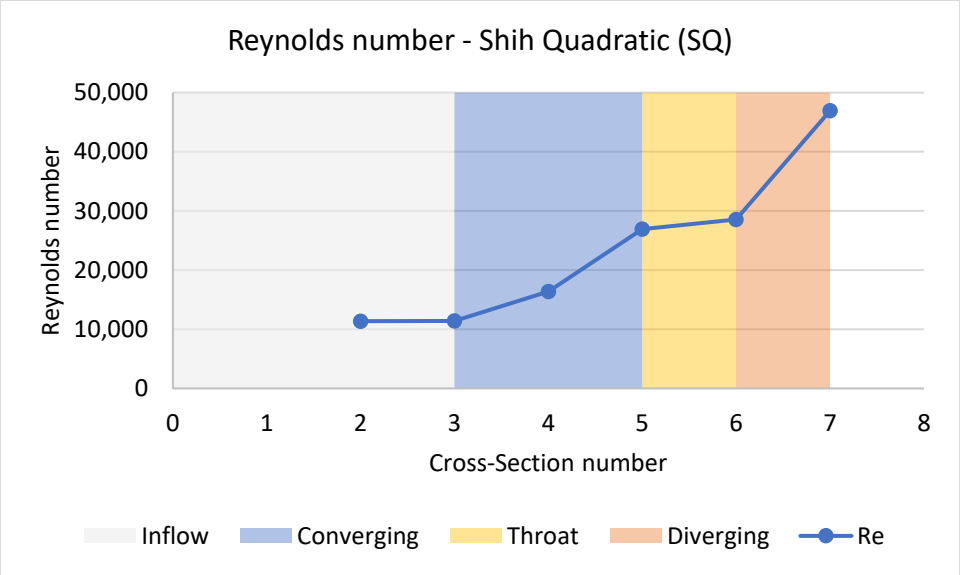

Figure 99: Reynolds number graph for SQ non-linear turbulence model

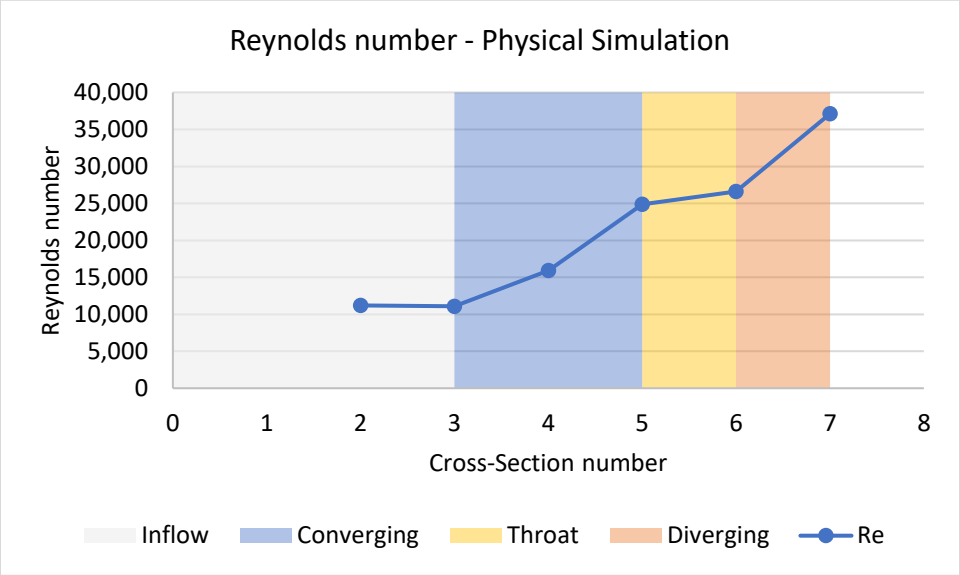

Figure 100: Reynolds number graph for Physical Simulation

References

1. Davis, R.W.; Deutsch, S. A Numerical-Experimental Study of Parhall Flumes. Journal of Hydraulic Research 1980, 18, 135–152, doi:10.1080/00221688009499557.
2. Sun, B.; Zhu, S.; Yang, L.; Liu, Q.; Zhang, C.; Zhang, J. ping Experimental and Numerical Investigation of Flow Measurement Mechanism and Hydraulic Performance on Curved Flume in Rectangular Channel. Arab J Sci Eng 2020, doi:10.1007/s13369-020-04949-x.
3. Xiao, Y.; Wang, W.; Hu, X.; Zhou, Y. Experimental and Numerical Research on Portable Short-Throat Flume in the Field. Flow Measurement and Instrumentation 2016, 47, 54–61, doi:10.1016/j.flowmeasinst.2015.11.003.
4. Savage, B.M.; Heiner, B.; Barfuss, S.L. Parshall Flume Discharge Correction Coefficients through Modelling. Proceedings of the Institution of Civil Engineers - Water Management 2014, 167, 279–287, doi:10.1680/wama.12.00112.
5. Sun, B.; Yang, L.; Zhu, S.; Liu, Q.; Wang, C.; Zhang, C. Study on the Applicability of Four Flumes in Small Rectangular Channels. Flow Measurement and Instrumentation 2021, 80, 101967.
6. Ran, D.; Wang, W.; Hu, X. Three-Dimensional Numerical Simulation of Flow in Trapezoidal Cutthroat Flumes Based on FLOW-3D. Frontiers of Agricultural Science and Engineering 2018, 5, 168–176.
7. Willeitner, R.P.; Barfuss, S.L.; Johnson, M.C. Using Numerical Modeling to Correct Flow Rates for Submerged Montana Flumes. J. Irrig. Drain Eng. 2013, 139, 586–592, doi:10.1061/(ASCE)IR.1943-4774.0000576.
8. Kim, S.-D.; Lee, H.-J.; Oh, B.-D. Investigation on Application of Parshall Flume for Flow Measurement of Low-Flow Season in Korea. Measurement Science Review 2010, 10, 111.
9. Hu, H.; Huang, J.; Qian, Z.; Huai, W.; Yu, G. Hydraulic Analysis of Parabolic Flume for Flow Measurement. Flow Measurement and Instrumentation 2014, 37, 54–64.
10. Heiner, B.; Barfuss, S.L. Parshall Flume Discharge Corrections: Wall Staff Gauge and Centerline Measurements. J. Irrig. Drain Eng. 2011, 137, 779–792, doi:10.1061/(ASCE)IR.1943-4774.0000355.
11. Wahl, T.L.; Replogle, J.A.; Wahlin, B.T.; Higgs, J.A. New Developments in Design and Application of Long-Throated Flumes. In Building Partnerships; 2000; pp. 1–10.

12. Howes, D.J.; Burt, C.M.; Sanders, B.F. Subcritical Contraction for Improved Open-Channel Flow Measurement Accuracy with an Upward-Looking ADVM. Journal of Irrigation and Drainage Engineering 2010, 136, 617–626.
13. Upp, E.L.; LaNasa, P.J. Fluid Flow Measurement: A Practical Guide to Accurate Flow Measurement; Elsevier, 2002; ISBN 978-0-08-050660-9.
14. Egyptian Clepsydra from the Temple of Karnak. Source: L. von Mackensen, Neue Ergebnisse Zur Ägyptischen Zeitmessung. Die Inbetriebnahme Und Berechnung Der Ältesten Erhaltenen Wasseruhr, Alte Uhren 1, 1978, Ohne Seitenangabe. Available online: https://www.topoi.org/project/a-3-8/, 03/01/2022.
15. Medlock, R.S. The Historical Development of Flow Metering. Measurement and Control 1986, 19, 11–22, doi:10.1177/002029408601900502.
16. Cascetta, F. Short History of the Flowmetering. Isa Transactions 1995, 34, 229–243.
17. Invention of the Venturi Meter. Nature 1935, 136, 254–254, doi:10.1038/136254a0.
18. Hayward, A.T.; Flowmeters, A. A Basic Guide and Source-Book for Users 1979.
19. Watral, Z.; Jakubowski, J.; Michalski, A. Electromagnetic Flow Meters for Open Channels: Current State and Development Prospects. Flow Measurement and Instrumentation 2015, 42, 16–25, doi:10.1016/j.flowmeasinst.2015.01.003.
20. Parshall Flume Figure Available online: https://en.wikipedia.org/wiki/File:Parshall_Flume.svg (accessed on 5 March 2022).
21. Engineering ToolBox, 2004 Available online: https://www.engineeringtoolbox.com/froude-number-d_578.html (accessed on 4 August 2022).
22. Heiner, B.J. Parshall Flume Staff Gauge Location and Entrance Wingwall Discharge Calibration Corrections. undefined 2009.
23. ASTM D1941 (2013). Standart Test Method for Open Channel Flow Measurement of Water with the Parshall Flume.
24. ISO-9826(1992). Measurement of Liquid Flow in Open Channelsparshall and SANIIRO Flumes.
25. Japanese Industrial Standard - JIS B 7553 : Parshall Flume Type Flowmeters. Japanese Industrial Standard 2017.
26. USBR Water Measurement Manual; United States Department of the Interior Bureau of Reclamation, 1953;

27. Sadrehaghighi, I. Turbulence Modeling with Case Studies; 2022;
28. Mendez, S.; Nicoud, F. Adiabatic Homogeneous Model for Flow around a Multiperforated Plate. AIAA journal 2008, 46, 2623–2633.
29. Schmitt, P.; Poinsot, T.; Schuermans, B.; Geigle, K.-P. Large-Eddy Simulation and Experimental Study of Heat Transfer, Nitric Oxide Emissions and Combustion Instability in a Swirled Turbulent High-Pressure Burner. Journal of Fluid Mechanics 2007, 570, 17–46.
30. Katopodes, N.D. Free-Surface Flow: Environmental Fluid Mechanics; Butterworth-Heinemann, 2018;
31. Tu, J.; Yeoh, G.H.; Liu, C. Computational Fluid Dynamics: A Practical Approach; Butterworth-Heinemann, 2018; ISBN 978-0-08-101244-4.
32. Cone, V.M. The Venturi Flume; U.S. Government Printing Office, 1917;
33. 20-Foot Concrete Parshall Flume with Radius Wing Walls. Available online: https://www.openchannelflow.com/assets/uploads/media/_large/20-foot-parshall-flume-curved-wing-walls.jpg, 12/01/2021.
34. Fiberglass 6-Inch Parshall Flume with Gauge. Available online: https://www.openchannelflow.com/assets/uploads/media/_large/flume-parshall-6-inch-fiberglass.png, 12/01/2021.
35. Parshall, R.L. The Parshall Measuring Flume. Agricultural Experiment Station—Colorado State University 1936.
36. Selecting Between a Weir and a Flume. 2022, Available online: https://www.openchannelflow.com/blog/selecting-a-primary-device-part-1-choosing-between-a-weir-and-a-flume.
37. Parshall, R.L. The Improved Venturi Flume. CER. 1928.
38. Heyrani, M.; Mohammadian, A.; Nistor, I. Numerical Simulation of Flow in Parshall Flume Using Selected Nonlinear Turbulence Models. Hydrology 2021, 8, 151, doi:10.3390/hydrology8040151.
39. Heyrani, M.; Mohammadian, A.; Nistor, I.; Dursun, O.F. Numerical Modeling of Venturi Flume. Hydrology 2021, 8, 27, doi:10.3390/hydrology8010027.
40. Alfonsi, G. Reynolds-Averaged Navier–Stokes Equations for Turbulence Modeling. Applied Mechanics Reviews 2009, 62, 040802, doi:10.1115/1.3124648.

41. Imanian, H.; Mohammadian, A. Numerical Simulation of Flow over Ogee Crested Spillways under High Hydraulic Head Ratio. Engineering Applications of Computational Fluid Mechanics 2019, 13, 983–1000, doi:10.1080/19942060.2019.1661014.
42. Khosronejad, A.; Herb, W.; Sotiropoulos, F.; Kang, S.; Yang, X. Assessment of Parshall Flumes for Discharge Measurement of Open-Channel Flows: A Comparative Numerical and Field Case Study. Measurement 2020, 167, 108292, doi:10.1016/j.measurement.2020.108292.
43. Dursun, O.F. An Experimental Investigation of the Aeration Performance of Parshall Flume and Venturi Flumes. KSCE J Civ Eng 2016, 20, 943–950, doi:10.1007/s12205-015-0645-0.
44. Shih, T.-H.; Liu, N.-S.; Chen, K.-H. A Non-Linear k-Epsilon Model for Turbulent Shear Flows. In Proceedings of the 34th AIAA/ASME/SAE/ASEE Joint Propulsion Conference and Exhibit; Cleveland, OH, USA, July 13 1998; p. 3983.
45. Lien, F.S. Low-Reynolds-Number Eddy-Viscosity Modelling Based on Non-Linear Stress-Strain/Vorticity Relations. In Proceedings of the Proceedings of 3rd Symposium on Engineering Turbulence Modelling and Measurement, 1996; Heraklion-Crete, Greece, May 27 1996.
46. Wright, S.J.; Tullis, B.P.; Long, T.M. Recalibration of Parshall Flumes at Low Discharges. Journal of Irrigation and Drainage Engineering 1994, 120, 348–362, doi:10.1061/(ASCE)0733-9437(1994)120:2(348).
47. Zerihun, Y.T. A Numerical Study on Curvilinear Free Surface Flows in Venturi Flumes. Fluids 2016, 1, 21, doi:10.3390/fluids1030021.
48. Kim, S.-Y.; Lee, J.-H.; Hong, N.-K.; Lee, S.-O. Numerical Simulation for Determining Scale of Parshall Flume. Proceedings of the Korea Water Resources Association Conference 2010, 719–723.
49. Tekade, S.A.; D VASUDEO, A.; D GHARE, A.; Ingle, R.N. Measurement of Flow in Supercritical Flow Regime Using Cutthroat Flumes. Sadhana 2016, 41, 265–272.
50. Tiwari, N.K.; Sihag, P. Prediction of Oxygen Transfer at Modified Parshall Flumes Using Regression Models. ISH Journal of Hydraulic Engineering 2020, 26, 209–220.
51. Thornton, C.I.; Smith, B.A.; Abt, S.R.; Robeson, M.D. Supercritical Flow Measurement Using a Small Parshall Flume. Journal of irrigation and drainage engineering 2009, 135, 683–692.

52. Cox, A.L.; Thornton, C.I.; Abt, S.R. Supercritical Flow Measurement Using a Large Parshall Flume. Journal of irrigation and drainage engineering 2013, 139, 655–662.
53. Ribeiro, Á.S.; e Sousa, J.A.; Simões, C.; Martins, L.L.; Dias, L.; Mendes, R.; Martins, C. Parshall Flumes Flow Rate Uncertainty Including Contributions of the Model Parameters and Correlation Effects. Measurement: Sensors 2021, 18, 100108.
54. Singh, J.; Mittal, S.K.; Tiwari, H.L. Discharge Relation for Small Parshall Flume in Free Flow Condition. International journal of research in engineering and technology 2014, 3, 317–321.
55. Willeitner, R.P.; Barfuss, S.L.; Johnson, M.C. Montana Flume Flow Corrections under Submerged Flow. Journal of irrigation and drainage engineering 2012, 138, 685–689.
56. Dufresne, M.; Vazquez, J. Head–Discharge Relationship of Venturi Flumes: From Long to Short Throats. null 2013, 51, 465–468, doi:10.1080/00221686.2013.781550.
57. Savage, B.M.; Heiner, B.; Barfuss, S. Parshall Flume Discharge Correction Coefficients through Modelling. Proceedings of the ICE - Water Management 2013, 167, 279–287, doi:10.1680/wama.12.00112.
58. Parshall, R.L. (Ralph L. Parshall Measuring Flume. 1936.
59. Robertson, E.D.; Chitta, V.; Walters, D.K.; Bhushan, S. On the Vortex Breakdown Phenomenon in High Angle of Attack Flows Over Delta Wing Geometries.; American Society of Mechanical Engineers Digital Collection, March 13 2015.
60. Tadayon, R. Modeling Curvilinear Flows in Hydraulic Structures. phd, Concordia University, 2009.
61. Adedoyin, A.A.; Walters, D.K.; Bhushan, S. Investigation of Turbulence Model and Numerical Scheme Combinations for Practical Finite-Volume Large Eddy Simulations. Engineering Applications of Computational Fluid Mechanics 2015, 9, 324–342, doi:10.1080/19942060.2015.1028151.
62. Hanjalic, K. Will RANS Survive LES? A View of Perspectives. Journal of Fluids Engineering 2005, 127, 831–839, doi:10.1115/1.2037084.
63. Jasak, H. OpenFOAM: Open Source CFD in Research and Industry. International Journal of Naval Architecture and Ocean Engineering 2009, 1, 89–94, doi:10.3744/JNAOE.2009.1.2.089.

64. Weller, H.G.; Tabor, G.; Jasak, H.; Fureby, C. A Tensorial Approach to Computational Continuum Mechanics Using Object-Oriented Techniques. Computers in Physics 1998, 12, 620, doi:10.1063/1.168744.
65. Wilcox, D.C. Turbulence Modeling for CFD; DCW industries La Canada, CA, 1998; Vol. 2; ISBN 0-9636051-5-1.
66. Cable, M. An Evaluation of Turbulence Models for the Numerical Study of Forced and Natural Convective Flow in Atria. 2009, 148.
67. Shih, T.-H.; Liou, W.W.; Shabbir, A.; Yang, Z.; Zhu, J. A New K-ϵ Eddy Viscosity Model for High Reynolds Number Turbulent Flows. Computers & fluids 1995, 24, 227–238.
68. Wang, W.; Wang, M. Application of KE Model on the Numerical Simulation of a Semi-Confined Slot Turbulent Impinging Jet. In Proceedings of the 2011 Fourth International Joint Conference on Computational Sciences and Optimization; IEEE, 2011; pp. 86–89.
69. Greenshields, C.J. The OpenFOAM Foundation." User Guide Version 6"; OpenFOAM Foundation Ltd, 2018;
70. Smagorinsky, J. General Circulation Experiments with the Primitive Equations: I. The Basic Experiment. Monthly weather review 1963, 91, 99–164.
71. Montazerin, N.; Akbari, G.; Mahmoodi, M. Developments in Turbomachinery Flow: Forward Curved Centrifugal Fans; Woodhead Publishing, 2015;
72. Moin, P.; Kim, J. Numerical Investigation of Turbulent Channel Flow. Journal of Fluid Mechanics 1982, 118, 341–377, doi:10.1017/S0022112082001116.
73. Piomelli, U.; Zang, T.A. Large-Eddy Simulation of Transitional Channel Flow. Computer Physics Communications 1990, 65, 224–230, doi:10.1016/0010-4655(91)90175-K.
74. Sohankar, A.; Davidson, L.; Norberg, C. A Dynamic One-Equation Subgrid Model for Simulation of Flow around a Square Cylinder. In Engineering Turbulence Modelling and Experiments 4; Elsevier, 1999; pp. 227–236 ISBN 978-0-08-043328-8.
75. Davidson, L. Large Eddy Simulations: A Note on Derivation of the Equations for the Subgrid Turbulent Kinetic Energies; Technical Report 97/11, Dept. of Thermo and Fluid Dynamics, Chalmers …, 1997;
76. Kim, W.-W.; Menon, S. A New Dynamic One-Equation Subgrid-Scale Model for Large Eddy Simulations. In Proceedings of the 33rd Aerospace Sciences Meeting and Exhibit; 1995; p. 356.

77. Brown, G.J.; Fletcher, D.F.; Leggoe, J.W.; Whyte, D.S. Application of Hybrid RANS-LES Models to the Prediction of Flow Behaviour in an Industrial Crystalliser. Applied Mathematical Modelling 2020, 77, 1797–1819, doi:https://doi.org/10.1016/j.apm.2019.09.032.
78. Baker, C.; Johnson, T.; Flynn, D.; Hemida, H.; Quinn, A.; Soper, D.; Sterling, M. Chapter 4 - Computational Techniques. In Train Aerodynamics; Baker, C., Johnson, T., Flynn, D., Hemida, H., Quinn, A., Soper, D., Sterling, M., Eds.; Butterworth-Heinemann, 2019; pp. 53–71 ISBN 978-0-12-813310-1.
79. Lindblad, D.; Jareteg, A.; Petit, O. Implementation and Run-Time Mesh Refinement for the K− ω SST DES Turbulence Model When Applied to Airfoils. Project work. Chalmers University of Technology 2014.
80. Menter, F.R.; Kuntz, M.; Langtry, R. Ten Years of Industrial Experience with the SST Turbulence Model. Turbulence, heat and mass transfer 2003, 4, 625–632.
81. Li, X.; Zhao, J. Dam-Break of Mixtures Consisting of Non-Newtonian Liquids and Granular Particles. Powder Technology 2018, 338, 493–505.
82. Morden, J.A.; Hemida, H.; Baker, C.J. Comparison of RANS and Detached Eddy Simulation Results to Wind-Tunnel Data for the Surface Pressures Upon a Class 43 High-Speed Train. J. Fluids Eng 2015, 137, doi:10.1115/1.4029261.
83. Spalart, P.; Jou, W.-H.; Strelets, M.; Allmaras, S. Comments on the Feasibility of LES for Wings, and on a Hybrid RANS/LES Approach; 1997;
84. Akan, A.O.; Houghtalen, R.J. Urban Hydrology, Hydraulics, and Stormwater Quality: Engineering Applications and Computer Modeling; John Wiley & Sons: Hoboken. New Jersey, 2003;
85. Figuérez, J.A.; González, J.; Galán, Á. Accurate Open Channel Flowrate Estimation Using 2D RANS Modelization and ADCP Measurements. Water 2021, 13, 1772, doi:10.3390/w13131772.
86. Vermeyen, T. Laboratory Calibration of a Nonstandard Parshall Flume; Hydraulics Branch Research and Laboratory Services Division: Denver, Colorado, 1991;
87. Weller, H.G.; Tabor, G.; Jasak, H.; Fureby, C. A Tensorial Approach to Computational Continuum Mechanics Using Object-Oriented Techniques. Computers in Physics 1998, 12, 620, doi:10.1063/1.168744.

88. Durbin, P.A. Separated Flow Computations with the K-Epsilon-v-Squared Model. AIAA journal 1995, 33, 659–664.
89. Shih, T.-H.; Lumley, J.L. Kolmogorov Behavior of Near-Wall Turbulence and Its Application in Turbulence Modeling. International Journal of Computational Fluid Dynamics 1993, 1, 43–56.
90. Reynolds, W.C. Fundamentals of Turbulence for Turbulence Modeling and Simulation; Stanford Univ CA Dept of Mechanical Engineering, 1987;
91. Shih, T.-H.; Zhu, J.; Lumley, J.L. A New Reynolds Stress Algebraic Equation Model. Computer methods in applied mechanics and engineering 1995, 125, 287–302.
92. Shih, T.-H. A Realizable Reynolds Stress Algebraic Equation Model; National Aeronautics and Space Administration, 1993; Vol. 105993;.
93. Suga, K. Eddy-Viscosity Modelling with Deformation Invariants and Non-Linear Elements. Ph.D. Thesis, UMIST, Manchester, United Kingdom: Dept. of Mech. Eng., 1993.
94. Nicoud, F. Unsteady Flows Modeling and Computation. LECTURE SERIES-VON KARMAN INSTITUTE FOR FLUID DYNAMICS 2007, 9, 3.
95. Deardorff, J.W. On the Magnitude of the Subgrid Scale Eddy Coefficient. Journal of Computational Physics 1971, 7, 120–133.
96. Schumann, U. Subgrid Scale Model for Finite Difference Simulations of Turbulent Flows in Plane Channels and Annuli. Journal of computational physics 1975, 18, 376–404.
97. Sagaut, P. Large Eddy Simulation for Incompressible Flows: An Introduction; Springer Science & Business Media, 2006;
98. Berselli, L.C.; Iliescu, T.; Layton, W.J. Mathematics of large eddy simulation of turbulent flows; Springer-Verlag: Heidelberg, 2006;
99. Galperin, B.; Orszag, S. Large Eddy Simulation of Complex Engineering and Geophysical Flows; Cambridge University Press: Cambridge, 1993;
100. Garnier, E.; Adams, N.; Sagaut, P. Large eddy simulation for compressible flows; Springer-Verlag: Heidelberg, 2009;
101. Grinstein, F.F.; Margolin, L.G.; Rider, W.J. Implicit Large Eddy Simulation: Computing Turbulent Fluid Dynamics; Cambridge University Press: Cambridge, 2007;
102. Ihme, M. Pollutant Formation and Noise Emission in Turbulent Diffusion Flames: Model Development and Application to Large-Eddy Simulation; VDM Verlag: Saarbru¨cken, 2008;

103. Lesieur, M. Large-Eddy Simulations of Turbulence; Cambridge University Press: Cambridge, 2005;
104. Meyers, J.; Geurts, B.J.; Sagaut, P. Quality and reliability of large eddy simulations; Springer-Verlag: Heidelberg, 2008;
105. Rodi, W.; Constantinescu, G.; Stoesser, T. Large-Eddy Simulation in Hydraulics; CRC Press: Hoboken, 2013;
106. Sagaut, P. Large Eddy Simulation for Incompressible Flows, an Introduction; Springer-Verlag: Heidelberg, 2001;
107. Sagaut, P. Large Eddy Simulation for Incompressible Flows, an Introduction; 2nd ed.; Springer-Verlag: Heidelberg, 2003;
108. Wagner CA, S.P., Hu¨. ttl T. Large-Eddy Simulation for Acoustics; Cambridge University Press: Cambridge, 2007;
109. Labourasse, E.; Sagaut, P. Advance in RANS-LES Coupling, a Review and an Insight on the NLDE Approach. Archives of Computational methods in Engineering 2004, 11, 199–256.
110. Travin, A.; Shur, M.; Strelets, M.; Spalart, P. Detached-Eddy Simulations Past a Circular Cylinder. Flow, turbulence and combustion 2000, 63, 293–313.
111. Tucker, P.G.; Davidson, L. Zonal k–l Based Large Eddy Simulations. Computers & Fluids 2004, 33, 267–287.
112. Piomelli, U.; Balaras, E.; Pasinato, H.; Squires, K.D.; Spalart, P.R. The Inner–Outer Layer Interface in Large-Eddy Simulations with Wall-Layer Models. International Journal of heat and fluid flow 2003, 24, 538–550.
113. Caruelle, B.; Ducros, F. Detached-Eddy Simulations of Attached and Detached Boundary Layers. International Journal of Computational Fluid Dynamics 2003, 17, 433–451.
114. Breuer, M.; Jovičić, N.; Mazaev, K. Comparison of DES, RANS and LES for the separated flow around a flat plate at high incidence. International Journal for Numerical Methods in Fluids 2003, 41, 357–388, doi:https://doi.org/10.1002/fld.445.
115. Rapp, B.E. Chapter 9 - Fluids. In Microfluidics: Modelling, Mechanics and Mathematics; Rapp, B.E., Ed.; Micro and Nano Technologies; Elsevier: Oxford, 2017; pp. 243–263 ISBN 978-1-4557-3141-1.